Investigating physical controls of vegetation-atmosphere interaction using ecosystem-scale measurements

Zur Erlangung des akademischen Grades einer
DOKTORIN DER INGENIEURWISSENSCHAFTEN (Dr.-Ing.)
von der KIT Fakultät für
Bauingenieur-, Geo- und Umweltwissenschaften des

Karlsruher Instituts für Technologie (KIT)

genehmigte
DISSERTATION
von
Gitanjali Thakur
aus Muzaffarpur (India)

Tag der mündlichen Prüfung: 18/07/2023
Referent: Prof. Dr.-Ing. Erwin Zehe
Korreferent: Dr. Stanislaus J. Schymanski
Karlsruhe (2024)

Acknowledgement

First and foremost, I would like to extend my heartfelt gratitude to my supervisor, Dr. Stanislaus Schymanski. Working under his guidance on this fascinating topic has been a privilege. His meticulous supervision, inspiring questions, and in-depth discussions have significantly enhanced my grasp of the literature, enabling clearer thinking and formulating a novel perspective. I have gained invaluable insights from him, ranging from the principles of open science ethics to honing a critical eye for detail.

I sincerely thank Prof. Erwin Zehe for accepting my PhD candidacy at KIT. Your encouragement, feedback, and practical guidance during our progress meetings have contributed significantly to a seamless journey and the successful completion of this thesis. Additionally, I sincerely appreciate the financial support that enabled me to attend EGU2022.

I want to thank Prof. Olivier Eiff for his insightful feedback during meetings from an experimentalist's perspective. His input has been crucial in shaping realistic model assumptions.

I sincerely thank Dr. Kaniska Mallick, Dr. Ivonne Trebs, and Dr. Mauro Sulis for their invaluable contributions as co-authors. I appreciate the time and expertise you have generously shared in ecosystem modelling. Our enlightening discussions on the various limitations of modelling and measurements have been instrumental in enhancing my understanding. I have gained immense knowledge from each of you, for which I am sincerely grateful.

I also sincerely thank Prof. Dan Yakir for reviewing my thesis and providing detailed, constructive feedback that has significantly improved the clarity of the explanation of the results. Additionally, I extend my gratitude to his lab members for their valuable discussions and insights into the measurements conducted at the Yatir Forest site, which were instrumental in formulating the model and interpreting the results.

I want to take this opportunity to express my gratitude to all the members of the Catchment and Ecohydrology group at the Luxembourg Institute Of Science and Technology for their friendliness and approachability. A special thanks go to my fantastic office mates (A001) for all the enjoyable fun, food, and laughter moments.

I want to thank my Grandma, Mom, Dad, Sneha, Devshil, and my in-laws for their love and encouragement.

Finally, I thank Atal for his unwavering support throughout this journey; I could not have done it without you.

Last but not least, thank you, Universe!

Abstract

Vegetation-atmosphere (V-A) interaction occurs through the exchange of energy, water, and carbon dioxide between the leaf surface and the atmosphere. The solar radiation absorbed by the leaves is partitioned into sensible heat, latent heat (water vapor), and outgoing longwave radiation. In analogy to Ohm's law, sensible heat is commonly expressed using a flux gradient relationship driven by the temperature difference between the surface and the atmosphere with a resistance determined by the physics of convective transfer. This aerodynamic canopy resistance is generally parameterized using wind conditions, air temperature gradients (buoyancy), and bulk canopy roughness. For modelling transpiration and CO2 uptake, an additional resistance is added to represent stomatal control on canopy gas exchange, such that the aerodynamic canopy resistance connects the physical control to the biological control (stomatal control) of canopy water and carbon exchange. However, limited process-based understanding of these resistances results in a widespread use of semi-empirical, site-specific parameterizations of aerodynamic canopy resistance based on a conceptual "aerodynamic temperature" instead of the actual leaf surface temperature. This simplification disconnects the leaf surface processes from ecosystem-scale observations, resulting in inconsistent and potentially inaccurate prediction of energy, water, and CO2 fluxes, thereby limiting our ability to predict ecosystem response to environmental change, such as increasing CO2 concentrations, rising temperatures, and changing precipitation and wind patterns.

Flux towers measure the incoming and outgoing radiative energy exchange using a radiometer and turbulent exchange of latent and sensible heat between the ecosystem and the atmosphere using the eddy covariance technique. Commonly, observed longwave radiation and remotely sensed regional values of surface emissivity are used to estimate surface temperature. Due to spatial heterogeneity of the land surface, the regional emissivity values result in potential bias of the surface temperature with respect to the observed turbulent fluxes. This further leads to wrong interpretation of ecosystem processes. For direct estimation of the total resistance to sensible heat transfer from observed sensible heat flux and air temperature, accurate estimates of surface temperature, adequately representing the sensible heat contributing surface, are required.

To investigate V-A exchange consistently at ecosystem scale, I developed self-consistent, physics-based mathematical models for the use of flux tower observations to evaluate the

drivers and resistances related to sensible heat transfer.

The research presented here addresses the following overarching research questions:

1. How can we use flux tower measurements to estimate ecosystem-scale emissivity and surface temperature?

2. How does surface heterogeneity affect the compatibility of eddy covariance measurements with the radiometric measurements at the flux tower sites?

3. How can we quantify ecosystem-scale resistance to sensible heat exchange using flux tower observations and how can we predict it from first principles?

A novel method is proposed to estimate the ecosystem-scale emissivity and temperature simultaneously using observed sensible heat flux and longwave radiation. I found that surface heterogeneity can result in a footprint mismatch between radiative and sensible heat flux measurements, which leads to inconsistency in the representation of the energy flux vs. temperature relationships. Despite this inconsistency, the observed slope of the sensible heat and estimated surface to air temperature difference resulted in robust estimates of ecosystem-scale total resistance to sensible heat transfer. Based on first principles, an ecosystem-scale total resistance model was developed that considers the surface characteristics and micro-meteorological conditions. The proposed resistance model is robust and estimates the surface-atmosphere resistance to sensible heat transfer substantially better than existing parameterizations. The methodology presented in this study can be used to improve the links between energy, water, and carbon exchange in land surface models, and greatly reduce the need for empirical parameterization and site-specific parameter tuning.

Zusammenfassung

Die Wechselwirkung zwischen Vegetation und Atmosphäre (V-A) erfolgt durch den Austausch von Energie, Wasser und Kohlenstoff zwischen der Blattoberfläche und der Atmosphäre. Die von den Blättern absorbierte Sonnenstrahlung wird in fühlbare Wärme, latente Wärme (Wasserdampf) und ausgehende langwellige Strahlung aufgeteilt. Analog zum Ohm;schen Gesetz wird die fühlbare Wärme üblicherweise durch eine Flussgradientenbeziehung ausgedrückt, die durch den Temperaturunterschied zwischen der Oberfläche und der Atmosphäre mit einem Widerstand bestimmt wird, der durch die Physik der konvektiven Übertragung bestimmt wird. Dieser aerodynamische Kronenwiderstand wird im Allgemeinen durch Windbedingungen, Lufttemperaturgradienten (Auftrieb) und die Kronenrauhigkeit parametrisiert. Für die Modellierung von Transpiration und CO 2 Aufnahme wird ein zusätzlicher Widerstand hinzugefügt, um die stomatäre Kontrolle des Gasaustauschs in der Baumkrone darzustellen, so dass der aerodynamische Widerstand der Baumkrone die physikalische Kontrolle mit der biologischen Kontrolle (stomatäre Kontrolle) des Wasser- und Kohlenstoffaustauschs in der Baumkrone verbindet. Das begrenzte prozessbasierte Verständnis dieser Widerstände führt jedoch zu einer weit verbreiteten Verwendung halbempirischer, standortspezifischer Parametrisierungen des aerodynamischen Kronenwiderstands, die auf einer konzeptionellen quot;aerodynamischen Temperatur quot; anstelle der tatsächlichen Temperatur der Blattoberfläche basieren. Durch diese Vereinfachung werden die Prozesse auf der Blattoberfläche von den Beobachtungen auf der Ebene des Ökosystems abgekoppelt, was zu inkonsistenten und potenziell ungenauen Vorhersagen von Energie-, Wasser- und CO 2 Flüssen führt und damit unsere Fähigkeit einschränkt, die Reaktion des Ökosystems auf Umweltveränderungen wie zunehmende CO 2 Konzentrationen, steigende Temperaturen und veränderte Niederschlags- und Windmuster vorherzusagen.

Flusstürme messen den ein- und ausgehenden Strahlungsenergieaustausch mit einem Radiometer und den turbulenten Austausch von latenter und fühlbarer Wärme zwischen dem Ökosystem und der Atmosphäre mit Hilfe der Wirbelkovarianztechnik. Zur Schätzung der Oberflächentemperatur werden in der Regel die beobachtete langwellige Strahlung und die aus der Ferne erfassten regionalen Werte des Oberflächenemissionsgrads verwendet. Aufgrund der räumlichen Heterogenität der Landoberfläche führen die regionalen Emissionswerte zu einer potenziellen Verzerrung der Oberflächentemperatur in

Bezug auf die beobachteten turbulenten Ströme. Dies führt außerdem zu einer falschen Interpretation der Ökosystemprozesse. Für eine direkte Schätzung des Gesamtwiderstands der fühlbaren Wärmeübertragung anhand der beobachteten fühlbaren Wärmeströme und der Lufttemperatur sind genaue Schätzungen der Oberflächentemperatur erforderlich, die die Oberfläche, die die fühlbare Wärme liefert, angemessen repräsentieren.

Um den V-A-Austausch auf Ökosystem-Ebene konsistent zu untersuchen, habe ich selbstkonsistente, physikalisch begründete mathematische Modelle entwickelt, um mit Hilfe von Flussturm-Beobachtungen die Triebkräfte und Widerstände im Zusammenhang mit der fühlbaren Wärmeübertragung zu bewerten.

Die hier vorgestellten Forschungsarbeiten befassen sich mit den folgenden übergreifenden Forschungsfragen:

1. Wie können wir die Messungen des Flussturms nutzen, um den Emissionsgrad und die Oberflächentemperatur auf Ökosystemebene zu schätzen?

2. Wie wirkt sich die Heterogenität der Oberfläche auf die Kompatibilität der Eddy-Kovarianz-Messungen mit den radiometrischen Messungen an den Flussturmstandorten aus?

3. Wie können wir den Widerstand gegen den Wärmeaustausch im Ökosystem anhand von Flussturmbeobachtungen quantifizieren und wie können wir ihn anhand erster Prinzipien vorhersagen?

Es wird eine neuartige Methode zur gleichzeitigen Schätzung des Emissionsgrads und der Temperatur auf Ökosystemebene unter Verwendung des beobachteten fühlbaren Wärmeflusses und der langwelligen Strahlung vorgeschlagen. Ich habe festgestellt, dass die Heterogenität der Oberfläche zu einer Fehlanpassung des Fußabdrucks zwischen den Messungen des Strahlungsflusses und des fühlbaren Wärmestroms führen kann, was zu Inkonsistenzen bei der Darstellung der Beziehungen zwischen Energiefluss und Temperatur führt. Trotz dieser Inkonsistenz führten die beobachtete Steigung der fühlbaren Wärme und die geschätzte Temperaturdifferenz zwischen Oberfläche und Luft zu robusten Schätzungen des Widerstands gegen die fühlbare Wärmeübertragung auf Ökosystemebene. Auf der Grundlage erster Prinzipien wurde ein Widerstandsmodell auf Ökosystemebene entwickelt, das die Oberflächeneigenschaften und mikrometeorologischen Bedingungen berücksichtigt. Das vorgeschlagene Widerstandsmodell ist robust und schätzt den Oberflächen-Atmosphären-Widerstand gegen die fühlbare Wärmeübertragung wesentlich besser ab als bestehende Parametrisierungen. Die in dieser Studie vorgestellte Methodik kann verwendet werden, um die Verbindungen zwischen Energie-, Wasser- und Kohlenstoffaustausch in Landoberflächenmodellen zu verbessern und den Bedarf an empirischer Parametrisierung und standortspezifischer Parameterabstimmung erheblich zu verringern.

Preface

Energy from the sun, plants need for all the fun,
and the control start to run.

Water and energy exchange begins at the leaf,
giving us all life in brief.
Forming clouds by taking water from the soil,
cooling the leaves down, not to boil.

Fun control alternate in range,
depending on the climate change.
Atmospheric control plays a significant role
quantifying it is the goal.

We need to comprehend
Flux tower measurement is the trend.
For us to recommend
we need to understand; not at all pretend.

Summarizing literature: Focusing on physical control and
surface temperature.
Found inconsistency in formulations and scale,
which required data intervention in detail.

Estimation of atmospheric control is no more a troll.
Let's start to roll!

Contents

List of Variables

Variable	Description	Unit
α	Surface albedo	–
ϵ	Surface emissivity	–
σ	Stefan-Boltzmann constant	$W\ m^{-2}\ K^{-4}$
ρ	Air density	$kg\ m^{-3}$
ϵ	Plot-scale effective emissivity	–
σ	Stefan–Boltzmann constant	$W\ m^{-2}\ K^{-4}$
ξ	Ratio of measurement height to Obhukov Length	–
β	Empirical constant used by Choudhury to account for r_r	–
ϵ_{MODIS}	Landscape-scale emissivity	–
ρ_a	Air density at room temperature	$Kg\ m^{-3}$
ψ_h	Correction term used to correct r_{a0} under non neutral condition	–
ϵ_{plot}	Plot-scale broadband monthly emissivity	–
ϵ_{rad}	Emissivity of soil and vegetation composite seen by the radiometer's FOV	–
C_p	Specific heat capacity of the air	$J\ kg^{-1}\ K^{-1}$
G	Ground heat flux	W m^{-2}
H	Sensible heat flux	W m^{-2}
H_{mod}	Modeled sensible heat flux using r_{lca} and $T_s - T_a$	$W\ m^{-2}$
K_h	Eddy diffusivity for heat exchange	$m\ s^{-2}$
K_m	Eddy diffusivity for momentum exchange	$m\ s^{-2}$
LAI	Leaf area index	–
LE	Latent heat flux	W m^{-2}
L_l	Leaf width	m

Variable	Description	Unit
M	Momentum flux	W m^{-2}
N_{NuL}	Nusselt number	–
R_{ldwn}	Downwelling longwave radiation	W m^{-2}
R_{lem}	Emitted longwave radiation	W m^{-2}
R_{lref}	Reflected longwave radiation	W m^{-2}
R_{lup}	Upwelling longwave radiation	W m^{-2}
R_{net}	Net Radiation	W m^{-2}
R_{sdwn}	Downwelling shortwave radiation	W m^{-2}
R_{sref}	Reflected shortwave radiation	W m^{-2}
Re_c	Reynolds number	–
RiB	Richardson number	–
T_0	Aerodynamic temperature	K
T_a	Air temperature measured at a reference height above the surface	K
T_{leq}	LST obtained using long equation	K
T_s	Surface temperature	K
T_s	Radiometric surface temperature of the vegetation canopy obtained using MODIS	K
$T_{s,avg}$	Average temperature using $Rlup,tot$ obtained from TSEB model	K
$T_{s,v}$	Weighted average of soil and vegetation temperature	K
T_{seq}	LST obtained using short equation	K
U_*	Observed shear velocity	$m\ s^{-1}$
U_{Z_h}	Horizontal wind speed at canopy top	$m\ s^{-1}$
U_z	Horizontal wind speed at height Z above the ground	ms^{-1}
W_s	Wind speed	$m\ s^{-1}$
Z_h	Canopy height	m
Z_m	Measurement height	m
Z_{oh}	Heat exchange roughness length	m
Z_{ohr}	Heat exchange radiometric roughness length	m
Z_{om}	Momentum roughness length	m

Variable	Description	Unit
c	Intercept of the linear regression between H and ΔT	$W\ m^{-2}$
d	Zero-plane displacement height	m
g	Acceleration due to gravity	$m\ s^{-2}$
k	Von Kármán constant	$-$
m	Monthly slope between H and ΔT	$m\ s^{-1}$
r_a	Total resistance to heat transport from surface to the atmosphere	$s\ m^{-1}$
r_{a0}	Canopy-air resistance considering T_0	$s\ m^{-1}$
$r_{a0,Allen}$	Aerodynamic resistance to heat exchange given by Allen et al.	$s\ m^{-1}$
$r_{a0,Thom}$	Aerodynamic resistance to heat exchange for non-neural condition by Thom et al.	$s\ m^{-1}$
$r_{a0,Verma}$	Aerodynamic resistance to heat exchange given by Verma et al.	$s\ m^{-1}$
r_{ah}	Canopy-scale aerodynamic resistance to the heat exchange	$s\ m^{-1}$
$r_{ah,Chou}$	Aerodynamic resistance to heat exchange given by Choudhury et al.	$s\ m^{-1}$
$r_{ah,slope}$	Effective canopy-scale resistance estimated using eddy covariance measurements	$s\ m^{-1}$
r_{am}	Resistance for momentum exchange	$s\ m^{-1}$
$r_{am,est}$	Estimated resistance to momentum exchange by inverting measured momentum flux	$s\ m^{-1}$
r_{az}	Momentum Resistivity	$s\ m^{-2}$
r_b	Quasi laminar boundary resistance (between Z_{0m} and Z_{oh})	$s\ m^{-1}$
r_{ca}	Canopy-air resistance derived between two level of the canopy	$s\ m^{-1}$
r_{lc}	Total effective leaf- boundary layer contributing to within canopy surface resistance	$s\ m^{-1}$
r_{lca}	Proposed leaf-canopy-air resistance	$s\ m^{-1}$

Variable	Description	Unit
r_{lh}	Leaf boundary layer resistance to heat exchange	$s\ m^{-1}$
r_r	Extra surface resistance when T_s is used instead of T_0	$s\ m^{-1}$

List of Abbreviations

R^2	Coefficient of determination
ABL	Atmospheric boundary layer
CCE	Canopy convector effect
EC	Eddy covariance
ECS	Eddy covariance sites
FAO	Food and Agriculture Organization
FOV	Field of view
HDF	Hierarchical data format
ICOS	Integrated carbon observation system
IRT	Infrared thermal
LST	Land surface temperature
MODIS	Moderate Resolution Imaging Spectroradiometer
NASA	National Aeronautics and Space Administration
NATT	North Australian Tropical Transect
PAI	Plant area index
PM	Penman-Monteith equation
QBL	Quasi-laminar boundary layer
RLP	Roughness length parameterization
RMSE	Root mean square error
SALib	Sensitivity Analysis Library
SEB	Surface energy balance
TERN	Terrestrial ecosystem research network
TIFF	Tagged image file format

List of Figures

List of Tables

Chapter 1

Introduction

Contents

1.1 Motivation

The relentless growth of the global population and its increasingly intense interactions with the natural environment exert significant pressure on groundwater and land resources, with the potential to cause irreversible environmental changes and catastrophic tipping points. The International Association of Hydrological Sciences (IAHS) designated the past decade (2013-2022) as a Scientific Decade focused on understanding the dynamic interplay between hydrology and society to address these pressing challenges. This initiative aimed to develop innovative theoretical frameworks for representing hydrological processes and environmental changes, emphasizing advanced monitoring and data analysis techniques (Montanari et al. 2013). Recent advancements in sensing technologies have markedly improved our ability to observe regional and ecosystem-scale data. These technologies enhance the estimation of ecosystem-scale parameters, such as specific vegetation cover, plant height, and leaf area index. In addition, Eddy covariance measurements (ECM) in varying land cover types have been instrumental in measuring energy partitioning by vegetation surfaces. ECMs are the most realistic measurement of water and energy fluxes close to the surface at a ecosystem-scale, and widely used for cal-

ibrating and evaluating land surface models (LSM). Accurate representations of energy, water, and carbon exchanges between the Earth's surface and the atmosphere are crucial for LSM, underscoring a promising future for climate models, which predict how Earth's climate will respond to environmental variations. Integrating new sensors at flux tower (ECM and radiometers) sites has enhanced data quality control. Data fusion techniques integrating data from multiple sources, such as remote sensing and high-resolution meteorological data, with flux tower observations have enhanced our understanding of ecosystem processes. Directly using these measurements can significantly benefit understanding the interactions and feedback mechanisms within hydrological systems, particularly those involving vegetation, soil, and the atmosphere.

The consequences of climate change on terrestrial ecosystems and human societies are primarily experienced through changes to the global water cycle (Jiménez Cisneros et al. 2014). Accurate simulation and prediction of various water cycle components require a comprehensive understanding of how vegetation and water resources respond to environmental forcings. Vegetation significantly influences land surface properties, including roughness and albedo. These properties determine the absorption and reflection of solar radiation by the land surface, affecting the partitioning of net available solar energy into fluxes of energy (sensible heat) and water (latent heat) that are returned to the atmosphere. This influence of vegetation on land surface properties directly impacts weather and climate on micro, macro and regional scales.

This doctoral research leverages ecosystem-scale and remote sensing measurements to investigate the interactions between vegetation and the atmosphere (V-A). The primary motivation is to use fundamental principles alongside state-of-the-art measured data (ECM, land surface parameter) to improve our ability to parameterize energy partitioning by natural vegetation surfaces under changing environmental conditions. This approach aims to deepen our understanding of the parameters controlling surface energy balance (SEB) partitioning, which is crucial for accurately quantifying and predicting the energy, water, and carbon fluxes exchanged between the Earth's surface and the atmosphere using models.

1.2 Background

Land-atmosphere (L-A) interactions link the land surface with the atmospheric boundary layer (ABL) through energy (solar and heat) and mass (carbon dioxide, water vapor and other gases) exchange. These interactions, occurring across a continuum of spatial and temporal scales, are an essential part of the hydrological cycle and climate. V-A interaction is vital in the L-A exchange process as it contributes to all atmospheric oxygen through carbon assimilation and 50% of the water vapor on land through transpiration (E). The energy exchange in V-A interaction originates predominantly at the leaf surface,

where the net available solar energy (R_{net}) is partitioned into sensible (H) and latent heat (LE) flux. This energy partitioning is referred to as SEB. In analogy to Ohm's law (Boulet et al. 1999), SEB components can be expressed mathematically using a flux gradient relationship. Leaf-scale H is driven by the leaf-to-air temperature difference and is controlled by the leaf boundary layer resistance (physical control), which can be parameterized using a flat-plate analogy (for heat exchange) by combining leaf geometry (leaf width, L_l) with atmospheric properties (wind speed (U_z)) , air density (ρ). Similarly, E, which drives LE flux, is driven by the leaf-to-air water vapor gradient and is controlled by stomatal resistance (biological control) in addition to the physical control. Stomata are tiny pores on the surface of leaves that open and close to regulate the exchange of water and carbon (CO_2) between the plant and the atmosphere by responding to environmental factors (wind speed, air temperature). This results in a two-way interaction between the leaf-scale processes and the ecosystem-scale micro-climate.

The evaluation of leaf-scale exchanges is crucial at the ecosystem-scale (canopy-scale) for both meteorological forecasting of ABL (Raupach and Finnigan 1988; Mauder, Foken, and Cuxart 2020) and water resource management (computation of evaporation and transpiration). The environmental variables (e.g., air temperature, wind speed) and the fluxes of energy, water, and carbon exchanged between the canopy-surface and the atmosphere, measured at hourly timescale using a flux tower (eddy-covariance tower), provide an excellent opportunity to investigate the controls of ecosystem-atmosphere interactions. Flux tower observations give us integrated measurements of fluxes from both vegetation and the soil surface. The turbulent fluxes of energy (H), water (LE), and carbon are measured using the eddy-covariance (EC) technique, the solar radiation (upwelling and downwelling) using radiometers, and the ground heat flux (G) using a heat plate placed beneath the soil surface. The incoming (solar radiation) and outgoing (H, LE) measurements are combined using the law of energy conservation (referred to as SEB), i.e., net available solar energy R_{net} equal to the sum of H, LE, and G. SEB is the core concept used in the models to estimate ecosystem-scale fluxes by parameterizing the exchange of energy, water, and net radiation. These components are then used to estimate the ecosystem-scale fluxes of carbon dioxide and water vapor through the photosynthesis-respiration and Penman-Monteith equations, respectively (Tanner and Fuchs 1968; Monteith 1965).

The ecosystem is generally approximated as a "big-leaf" surface treated as a homogeneous unit with a single set of surface properties (such as albedo, emissivity, roughness, and temperature). The exchange of momentum, energy, water, and carbon from the big-leaf surface to the atmosphere is parameterized using the physics of turbulent transfer, which is based on the eddy diffusivity theory. Eddy diffusivity measures how effectively turbulent eddies can transport heat or momentum in the air column and plays a key role in parameterizing ecosystem-scale H and LE. Since eddy diffusivity theory is valid only

in the air column, H is parameterized using aerodynamic temperature instead of surface temperature and is controlled by canopy-scale aerodynamic resistance. Aerodynamic temperature is defined as the average air temperature near the vegetation elements within the canopy (where the big-leaf surface is positioned)(Allen et al. 1998). Aerodynamic canopy resistance is generally parameterized using wind conditions, air temperature gradients (buoyancy), and bulk roughness (Choudhury and Monteith 1988). For modeling transpiration and CO_2 uptake, additional resistance is added to represent stomatal control on canopy gas exchange. The aerodynamic canopy resistance connects the physical control to the biological control (stomatal control) of canopy water and carbon exchange. This approach was designed to provide a mechanistic understanding of ecosystem processes and for the prediction of how ecosystems will respond to environmental changes, such as changes in temperature or precipitation.

1.3 Research gaps

The instantaneous value of ecosystem-surface temperature, commonly referred to as land surface temperature (LST), is a function of the net radiation (R_{net}), sensible heat flux (H), latent heat flux (LE), and ground heat flux (G). LST is defined as the "ensemble directional radiometric surface temperature" (Norman and Becker 1995) and is estimated from the infrared radiance emitted by a surface with known emissivity (ϵ). Emissivity is an intrinsic property of a surface, quantifying its efficiency in radiating thermal energy relative to a blackbody, with values ranging from 0 to 1. LST controls the magnitude and variability of surface energy balance (SEB) components (H and LE) and is also influenced by SEB partitioning, making it a critical variable for understanding L-A interactions. Despite its importance, the lack of direct LST measurements at the canopy-scale (ecosystem-scale) hampers a comprehensive understanding of the interactions and feedback mechanisms between LST and H and LE fluxes. Deriving LST from observed upwelling longwave radiation (R_{lup}) at flux towers requires knowledge of surface emissivity, which is not typically measured routinely. Flux tower observations capture a composite signal from soil and vegetation, which generally exhibit different surface temperatures and emissivity ranges. The emissivity of soil and vegetation varies depending on soil moisture content, vegetation structural attributes, and leaf area index. This variability makes ecosystem-scale emissivity a dynamic parameter that fluctuates seasonally; thus, the ϵ estimation representing the canopy surface is not straightforward. Consequently, ecosystem-scale emissivity is crucial for accurate ecosystem-scale energy balance models. However, constant ϵ values obtained through remote sensing technologies (satellites) at landscape scale or estimated from look-up tables often lead to inaccurate LST estimations for a canopy surface (**rolim20comparison**).

The ecosystem surface, comprising soil and vegetation, exhibits diverse surface prop-

erties that influence its interactions with incoming solar radiation, such as absorption, reflection, and emission of the received solar radiation. Flux tower uses an eddy-covariance measurement system to measure solar radiation using radiometers, turbulent heat fluxes (H), and water (LE). The radiometer and the EC tower have different footprints. A footprint is the surface area influencing the observation (Schmid 2002). Turbulent fluxes (H, LE) measured using the EC system (ECS) are averaged over a relatively large area, with footprints spanning several hundreds of meters. In contrast, radiometers, which measure incoming and outgoing solar radiation (R_{net}, R_{lup}), typically have much smaller hemispherical footprints, about a tenth of a meter (Wohlfahrt and Tasser 2015). Spatial heterogeneity due to variations in land cover types, canopy structure, and soil types within the footprint results in a footprint mismatch between the radiometer and the ECS. Such mismatches can lead to incorrect representations of the surface energy balance (SEB) components and biases in the estimated LST (estimated using R_{lup}) compared to observed turbulent fluxes (H, LE) due to the unrepresentativeness of the surface representing measurements. Furthermore, satellite-derived emissivity (ϵ), meant for landscape-scale applications at canopy-scale, can introduce additional bias in canopy-scale LST. Therefore, quantifying surface heterogeneity is crucial for accurate LST estimation and calculating the canopy surface's SEB, ensuring that all flux components represent similar heterogeneity within their footprints.

Another significant challenge with flux tower measurements is the non-closure of the SEB, where the sum of observed H, LE, and G does not equal R_{net}, often the sum of H and LE is smaller than R_{net}, leading to energy imbalance (Twine et al. 2000). This imbalance in incoming and outgoing fluxes is typically due to underestimating the H and LE, mainly due to secondary eddies. Since in the models, the energy balance is closed therefore, before using the H and LE fluxes to compare with the model result, a correction is applied to the observed H and LE fluxes using the energy balance closure (EBC) scheme (Twine et al. 2000). The EBC schemes applied to the observation can mask underlying model biases, leading to incorrect conclusions about model performance (Ehret et al. 2012). Previous studies have suggested that surface heterogeneity could be a potential reason for the non-closure of energy balance. However, there are no definitive studies that directly link canopy-scale surface heterogeneity to energy imbalance. Therefore, to use the flux tower measurements to improve ecosystem-scale SEB models, further research is needed to quantify the contribution of surface heterogeneity to the non-closure of energy balance.

V-A interactions begin at the leaf surface; following Ohm's law, the heat flux is represented using surface-air temperature difference and constrained by the resistance to heat exchange. Current canopy models that study vegetation-atmosphere (V-A) interactions typically parameterize sensible heat flux (H) using aerodynamic theory (aerodynamic temperature, aerodynamic resistance). Aerodynamic temperature, representing

the air temperature within the canopy (at heights closer to the canopy top), decouples the canopy surface where energy partitioning occurs. The canopy surface includes all surfaces within the canopy, primarily leaves, that partition solar energy into H and LE. Canopy-scale heat exchange is the sum of the heat exchanges occurring with all surfaces within the canopy depending on leaf surface temperature and leaf resistance to sensible heat (Schymanski and Or 2017). Therefore, it is crucial to consider surface temperature (LST) to parameterize sensible heat flux instead of using aerodynamic temperature. However, using surface temperature in V-A heat exchange models is problematic due to the aerodynamic theory's inapplicability near the surface (in the viscous sublayer). Consequently, the semi-empirical parameterization of resistance to heat exchange typically accounts only for aerodynamic resistance, neglecting leaf-scale resistance. These assumptions create a disconnect between leaf-scale processes and fluxes measured at the canopy-scale by the flux tower. This disconnect hinders the association of observed fluxes with vegetation surface processes, leading to inadequate representation of the heat exchange resistance and inaccurate predictions of energy, water, and CO_2 fluxes. We need to connect leaf-scale exchanges with canopy-scale measurements to predict ecosystem responses to environmental changes. To predict ecosystem behaviour under varying environmental conditions, including increasing CO_2 concentrations, rising temperatures, and shifting precipitation and wind patterns connecting the leaf-scale process with canopy-scale measurement, is required.

To address these research gaps and to investigate the V-A exchange consistently using flux tower observations, the research presented here addresses the following overarching research questions:

Research questions:

1. How can we use eddy-covariance measurements to estimate canopy-scale emissivity and surface temperature?
2. How does surface heterogeneity affect the compatibility of eddy-covariance measurements with the radiometric measurements at the flux tower sites?
3. How can ecosystem-scale resistance to heat exchange be quantified using flux tower observations, and how can a resistance model be formulated to connect leaf-scale processes with canopy-scale aerodynamic theory?

1.4 Overall methodology

To address the research questions we used three years of flux tower measurements from fourteen sites having good data quality and different land cover types. The measurements were obtained from standard platforms sharing flux tower measurements (ICOS (https://www.icos-cp.eu/), TERN (https://www.tern.org.au/) ; Fluxnet (https:

//fluxnet.org/), Ameriflux (https://ameriflux.lbl.gov/). The satellite derived land surface measurements (LST and emissivity) were taken from MODIS TERRA satellite (MODA011).

Figure 1.1: Study sites used in this work

Table 1.1: Description of study sites

Study site	Abbreviation	Landcover type
Adelaide River	AR	Savanna dominated by Eucalyptus tectifica and Planchonia careya
Alice Springs	AS	Mulga woodland, hummock grassland, river red gum forest
Brookings	BR	Cropland
Daly Uncleared	DU	Woodland savanna
Gebesee	GB	Cropland
Howard Springs	HS	Open woodland savanna
Litchfield	LF	Tropical savanna
Neustift	NS	Grassland
Oensingen	OS	Cropland
Rollesbroich	ROL	Grassland
Sturt Plains	SP	Mitchell Grass
Tharandt	TH	72% spruce and 13% deciduous forest (10% larch)
Ti Tree East	TT	Grassy mulga woodland, Corymbia/ Triodia savanna
Tumbarumba	TUM	Wet sclerophyll
Yatir Forest	YF	Evergreen need-leaf forest

An example of flux tower instrumentation at Yatir Forest (picture obtained from the group of Prof. Dan Yakir through personal communication) is shown in Fig. 1.2.

1.5 Thesis outline

The three research questions have been answered in three chapters.

Chapter 2

Due to the involvement of two unknowns (temperature and emissivity (ϵ)) inside one measurement variable (upwelling longwave radiation), estimating in-situ surface temper-

Figure 1.2: Flux tower instrumentation at Yatir Forest. The site consists of an eddy-covariance system (ECS), net radiometer, thermocouples, soil heat plate and rain gauge. ECS consist of a three dimensional sonic anemometer that measures wind speed and direction in three dimensions (u, v, w) and provides data on turbulence, and an infrared gas analyzer (IRGA) measures concentrations of CO_2 and H_2O vapor to calculate their fluxes. Net radiometer measures net radiation (R_{net}) as the difference between incoming and outgoing shortwave and longwave radiation. Thermocouples measure air and soil temperature. Soil heat flux plates measure ground heat flux (G), and rain gauges measure precipitation.

ature (LST) is not straightforward. Most of the time, the models use satellite-derived LST and ϵ values to estimate SEB and the SEB components are validated using flux tower measurements. Therefore, it is important to quantify the correspondence between satellite-derived LST and the co-dependent variable, ϵ, with the flux tower observations. To address these complexities associated with ecosystem-scale LST and emissivity estimation, this chapter formulates an alternative method to simultaneously estimate LST and emissivity by combining the measured longwave radiation with sensible heat (H) and air temperature (T_a). One of the early studies by Holmes et.al. (Holmes et al. 2009) used a similar approach to estimate emissivity and LST; however, only one component of the upwelling longwave, i.e., emitted longwave, was used, and the reflected component was ignored. Ignoring reflected longwave component is a common approach in the literature to estimate surface temperature by considering $\epsilon = 1$.

For the adequate estimate of LST and ϵ and to quantify the consequence of omitting the reflected longwave radiation component for ecosystem-scale LST and emissivity. Research question for chapter 2 are:

1. How much is the bias in LST and ϵ when we ignore the reflected downwelling component?
2. Does the estimation of ecosystem-scale ϵ have an advantage over satellite-observed ϵ?
3. How much uncertainty is introduced in plot-scale LST and ϵ due to uncertainty of the observed fluxes?

Chapter 3

In this chapter, we investigate the impact of surface heterogeneity on ecosystem-

scale estimates of surface temperature and ϵ at flux tower sites. A two-source (ground-vegetation) SEB model is formulated to quantify the impact of surface heterogeneity by combining radiometric and EC measurements. The heterogeneity scenario was simulated by hypothesizing that the fraction of vegetation seen by the radiometer is different from the fraction of vegetation measured by the ECS which will lead to footprint mismatch between the radiometer and the eddy covariance tower.

Research questions for chapter 3 are:

1. How can we use flux tower measurement to quantify the surface heterogeneity present at the site?
2. To what extent does surface heterogeneity contribute to energy imbalance?
3. What is the most effective procedure for treating flux tower measurements in the presence of footprint mismatch due to spatial heterogeneity?

Chapter 4

A decent amount of literature exists on the empirical estimation of aerodynamic resistances for various ecosystems based on roughness length parameterizations and atmospheric stability correction. Most of these parameterizations do not explicitly include the leaf boundary layer and, therefore, rely on a conceptual 'aerodynamic temperature' at some distance from the actual leaf surfaces. This gap hampers reliable modeling of canopy gas exchange (transpiration and CO_2 assimilation) as these processes happen directly at the leaf surface and rely on accurately capturing the leaf surface temperature. An additional resistance based on a 'KB^{-1}' parameterization is commonly added to the classical aerodynamic resistance to bridge this gap. In this chapter, we estimate the benchmark resistance values for canopy-scale heat and momentum exchange by inverting the flux-profile equations (eddy-diffusivity theory). A self-consistent mathematical model was developed by using aerodynamic conditions and canopy properties to represent the benchmark resistance value at the study sites.

Research questions for chapter 4 are:

1. How can we infer benchmark canopy-scale heat and momentum resistance from eddy covariance measurements?
2. How can we compare existing canopy-scale aerodynamic resistance parameterizations with the estimated benchmark resistance?
3. How can we formulate a consistent heat exchange resistance model by coupling leaf-surfaces to the canopy-air space?

Chapter 2

Surface emissivity and temperature estimation using plot-scale measurement

An edited version of this paper was published in Scientific Reports as:
Thakur, G., Schymanski, S.J., Mallick, K. et al. "Downwelling longwave radiation and sensible heat flux observations are critical for surface temperature and emissivity estimation from flux tower data." *Sci Rep* 12, 8592 (2022).
https://doi.org/10.1038/s41598-022-12304-3

Contents

2.1 Introduction

The effects of global change are reflected in land surface temperature (LST) anomalies and their interannual variability (Rowell 2005). It controls the magnitude and variability of

the surface energy balance (SEB) components and simultaneously gets modulated by the SEB partitioning (Mallick et al. 2015; Timmermans et al. 2007). LST contains imprints of surface moisture and is extremely sensitive to evaporative cooling, which makes it a preeminent variable for studying evaporation and surface-atmosphere exchange (Mallick et al. 2018a; Trebs et al. 2021a; Kustas and Anderson 2009). It directly affects the amount of emitted longwave radiation and influences the saturation vapor pressure at the surface that drives latent heat flux. Thus, the ecohydrological functioning and carbon-water coupling are largely controlled by the surface temperature of the soil-vegetation system (Still et al. 2021). The availability of an extensive network of eddy covariance measurements (flux tower) allows us to understand the interactions and feedbacks between the surface-atmosphere exchange processes such as evaporation, transpiration, and its control by the atmosphere and vegetation at the diurnal time scale. However, the unavailability of direct LST measurements at the same scale hinders a detailed understanding of the interactions and feedbacks between LST and surface-atmosphere exchange processes, which is of utmost importance to the climate modeling community (Migliavacca et al. 2021).

Inversion of the longwave radiation in flux tower data to obtain LST has gained popularity in recent years. LST estimation depends on the emissivity of the underlying surface (Mallick et al. 2018b), which is not available as routine measurement. Therefore, estimating in-situ LST is not straightforward due to the involvement of two unknowns (LST and emissivity) inside one measurement variable (upwelling longwave radiation). To circumvent this challenge, we conducted simultaneous retrievals of LST and emissivity by exploiting the longwave radiation components in conjunction with associated SEB flux measurements (Holmes et al. 2009; Maes et al. 2019).

The SEB components can be sub-divided into radiative components (often lumped in net radiation, R_{net}) and thermodynamic components, including sensible heat flux (H), latent heat flux (LE), and ground heat flux (G) respectively as shown:

$$R_{net} = H + LE + G \tag{2.1}$$

The instantaneous value of LST is the result of interplay between the R_{net} at the surface, H, LE and, G (Wang and Dickinson 2013). Thus, LST can also be used for the estimation of H (Sun and Mahrt 1995) and LE (Jacob et al. 2001) between the surface and the atmosphere. LST provides the lower-boundary condition in SEB models for diagnostic estimates of LE and is highly relevant for drought monitoring (Trebs et al. 2021a; Mallick et al. 2016; Mallick et al. 2015). As the surface-to-air temperature difference drives the exchange of sensible heat between surface and atmosphere, all components of Eq. (2.1) depend on the LST.

Net radiation (R_{net}) can be sub-divided into downwelling and upwelling components

(Verma et al. 2016) as shown below:

$$R_{net} = R_{sdwn} + R_{ldwn} - R_{sref} - R_{lref} - R_{lem} \tag{2.2}$$

Here, R_{sdwn} and R_{ldwn} are the shortwave and longwave downwelling components, R_{sref} and R_{lref} are the shortwave and longwave reflected components, and R_{lem} is the longwave emitted component. Only a fraction of solar top-of-the-atmosphere radiation reaches the Earth's surface, as some is reflected back to space by clouds, some is absorbed by the atmosphere and emitted later as longwave radiation. Reflected shortwave (R_{sref} in Eq. (2.2) is expressed as $R_{sref} = \alpha\ R_{sdwn}$, while reflected longwave (R_{lref}) is represented as $R_{lref} = \alpha R_{ldown}$, where α is the surface albedo. The emitted longwave radiation as a function of surface temperature (T_s) and surface emissivity (ϵ) is given by Stefan-Boltzmann (SB) equation (Lhomme et al. 1988)

$$R_{lem} = \epsilon\sigma T_s^4 \tag{2.3}$$

where, σ ($W\ m^{-2}\ K^{-4}$) is the SB constant, ϵ is the surface emissivity ranging between 0 and 1, and T_s (K) is the LST. For a land surface, ϵ depends on soil type, vegetation cover, soil moisture, soil chemistry, roughness, spectral wavelength, temperature and view angle (Norman and Becker 1995).

The emitted and downwelling longwave radiance are measured at given angle within its instantaneous field of view (FOV) by a downward facing sensor relatively close to the surface (a few meters for an eddy covariance (EC) tower). The radiation received by a pyrgeometer or infrared sensor is a combination of the radiation emitted (R_{lem}) and reflected (R_{lref}) by the surfaces in its FOV as shown in Eq. (2.4):

$$R_{lup} = R_{lem} + R_{lref} \tag{2.4}$$

Substitution of Eq. (2.3) into Eq. (2.4) and replacing α as $1-\epsilon$, R_{lup} becomes a function of emissivity, surface temperature and downwelling longwave radiation:

$$R_{lup} = \epsilon\sigma T_s^4 + (1-\epsilon)R_{ldwn} \tag{2.5}$$

Eq. (2.5) is then solved for LST as a function of measured longwave and known surface emissivity:

$$T_s = \sqrt[4]{\frac{R_{ldwn}}{\sigma} - \frac{R_{ldwn}}{\epsilon\sigma} + \frac{R_{lup}}{\epsilon\sigma}} \tag{2.6}$$

In order to invert LST as shown in Eq. (2.6), ϵ values are required. However, radiometers at eddy covariance sites (ECS) do not measure spectral bands separately to deduce emissivity directly. Therefore, we will deduce site-specific ϵ from observations of

air temperature (T_a), measured longwave (R_{ldwn}, R_{lup}) and sensible heat flux (H) (Holmes et al. 2016). In analogy to Ohm's law, the linear relationship between H and ΔT can be expressed mathematically as:

$$H = m(T_s - T_a) \tag{2.7}$$

where, m ($m\ s^{-1}$) is a proportionality constant (defined as $m = \rho C_p / r_a$ and broadly referred to as heat transfer coefficient) and depends on surface characteristics and micro-meteorology (Lhomme et al. 1988), T_a (K) is the temperature of the air measured at a reference height above the surface, C_p ($J\ kg^{-1}\ K^{-1}$) is the specific heat capacity of air, ρ ($kg\ m^{-3}$) is the air-density, and r_a ($s\ m^{-1}$) is the total resistance to heat transport from surface to the atmosphere. It is evident from Eq. (2.7) that for $T_s - T_a = 0$, H will be zero. This boundary condition and the linear relationship between H and ΔT is used to estimate ϵ (Holmes et al. 2009; Holmes et al. 2016). Another approach for plot-scale ϵ estimation filters the data where H is close to zero, substitutes T_s in Eq. (2.5) by T_a and solves for ϵ (Maes et al. 2019).

However, due to surface heterogeneity, sparse canopies are prone to footprint mismatch between the aerodynamic (flux tower) footprint and radiometric (hemispherical) footprint (Chu et al. 2021; Marcolla and Cescatti 2018; Morillas et al. 2013), where the aerodynamic footprint represents the area contributing to measured sensible heat flux, while the radiometric footprint is dominated by the surface below the sensor at a Nadir viewing angle, contributing to the measured longwave radiation (used for T_s estimation). This can result in a different boundary condition i.e. at $\Delta T = 0$, $H \neq 0$ as expressed in Eq. (2.8):

$$H = m(T_s - T_a) + c \tag{2.8}$$

where, H is representative of the sensible heat flux from the EC tower footprint, T_s is representative of all the radiating surfaces in the radiometric sensor's view, and c is interpreted as the H from surfaces in the aerodynamic footprint that are not seen by the radiometer.

Plot-scale estimation of ϵ and LST using observed H, T_a, R_{lup} and R_{ldwn} as described above and in the Methods section (2.2), may be prone to substantial uncertainty. It is unclear how uncertainties in observed fluxes propagate into the uncertainty of estimated LST and ϵ. By design, infrared thermal (IRT) sensors only measure upwelling infrared radiance and therefore cannot explicitly account for the amount of reflected downwelling infrared radiation in the signal. For a long time, downwelling longwave (R_{ldwn}) was not routinely observed at ECS (Wang and Liang 2009) and was also considered to be the most poorly quantified component of the radiation budget (Trenberth and Fasullo 2012). Therefore, the second term in Eq. (2.5) is commonly omitted, arguing that $\epsilon \approx 1$, and

hence, Eq. (2.5) is simplified to Eq. (2.9) (Crago and Qualls 2014):

$$R_{lup} \approx \epsilon \sigma T_s^4 \tag{2.9}$$

Eq. (2.9) can be solved for T_s to yield what we will term the "short equation" (seq) for T_s:

$$T_s \approx \sqrt[4]{\frac{R_{lup}}{\epsilon \sigma}} \tag{2.10}$$

Note that the above derivation is actually flawed, as the second term of Eq. (2.5) was omitted arguing that $\epsilon \approx 1$, and yet ϵ was retained in the first part of the equation. Nevertheless, even with the availability of downwelling longwave measurements (Stephens 1995), the use of Eq. (2.9) is still a common practice (Crago and Qualls 2014; Mallick et al. 2018b). This gives rise to the question if the short equation (Eq. (2.10)) is adequate to estimate LST from ground-based measurements. In the remainder of this chapter, we will refer to LST obtained using the long equation (Eq. (2.6)) as T_{leq} and to LST obtained using the short equation (Eq. (2.10)) as T_{seq}.

To better understand and improve approaches of plot-scale LST estimation, the present study addresses the following research questions:

1. Can we obtain an adequate estimate of plot-scale LST while neglecting the reflected downwelling longwave radiation?

2. Does the estimation of plot-scale ϵ based on observed sensible heat flux (H) have an advantage over satellite-derived ϵ for plot-scale LST estimation?

3. How much uncertainty is introduced in plot-scale LST and ϵ due to uncertainty in measured EC fluxes?

To answer these questions, we analysed data for ten eddy covariance sites in different biomes and climates (see Table 2.1). Plot-scale broadband monthly emissivity (ϵ_{plot}) was derived using observed H and estimated ΔT as proposed by Holmes et al. (Holmes et al. 2009). Plot-scale LST was estimated using either Eq. (2.6) or Eq. (2.10), and either ϵ_{plot} or landscape-scale emissivity (ϵ_{MODIS}). Estimated LST was compared with Moderate Resolution Imaging Spectroradiometer (MODIS) LST (TERRA satellite-sensed) for the times of satellite overpass. Uncertainty in ϵ_{plot} and LST due to uncertainty in observed fluxes was calculated using Sobol-based uncertainty analysis (implemented with Sensitivity Analysis Library (SALib)) (Rosolem et al. 2012).

2.2 Methods

In the last two decades, plot-scale radiometric data collected at ECS have gained popularity for in-situ LST retrieval due to its high temporal resolution (Stoy et al. 2013;

Cullen et al. 2007). In addition to this, the LST estimates at plot-scale originate from a relatively homogeneous footprint in comparison to the satellite-derived LST (MODIS pixels). This section describes: (i) how to retrieve plot-scale LST and ϵ using EC measurements, (ii) how to quantify the correspondence between plot-scale LST with MODIS LST and, (iii) how to quantify the uncertainty in plot-scale LST and ϵ.

Tower data: ECS collect micro-meteorological measurements above the surface (vegetation canopy) using flux towers following common measurement protocols (Baldocchi et al. 2001). The towers are generally equipped with an instrument made up of pyrgeometers or radiometers to measure upwelling and downwelling shortwave and longwave radiation, which is further used to calculate net radiation (Eq. (2.2)). Besides radiative fluxes, measurement at ECS also include sensible and latent heat fluxes, net carbon-dioxide exchange and a range of meteorological variables, such as air temperature (T_a), humidity and wind speed. T_a is the air temperature measured at a reference height above the canopy. Each flux measurement is accompanied by a flagging system based on the second CarboEurope-IP QA/QC workshop (Gilberto et al. 2020). In our current work, we use high quality available data (flag 0) as it is without atmospheric corrections. For the analysis, ten sites were selected to represent a variety of land cover types and climates (Table 2.1). Eight sites belong to the North Australian Tropical Transect (NATT) and two sites (Yatir Forest (YF), Brookings (BR)) are chosen to replicate results from Holmes et.al (Holmes et al. 2009) as shown in Table 2.1. Eddy covariance level 3 data is obtained from http://data.ozflux.org.au/portal/pub/listPubCollections.jspx for Australian sites. The data for Brookings was obtained from Ameriflux whereas the data for Yatir Forest was obtained through personal communication with Professor Yakir's lab in order to obtain the older version of the data, which was used by Holmes et al. (Holmes et al. 2009).

MODIS data: Landscape-scale emissivity and LST data (MODIS product MOD11A1) was downloaded from National Aeronautics and Space Administration (NASA) Earth data . It is a level 3 daily LST product gridded in the sinusoidal projection at a spatial resolution of 0.928 km by 0.928 km. The daily LST pixel values in each granule (tile contains 1200 x 1200 grids in 1200 rows and 1200 columns) is retrieved by the generalized split-window algorithm under clear-sky conditions and MODIS LST values are averaged by overlapping pixels in each grid with overlapping areas as weight (Wan 2007). The downloaded data in hierarchical data format (HDF), were converted into tagged image file format (TIFF) using the python package pyModis (Delucchi 2014). Alternatively MODIS data can also be obtained from https://appeears.earthdatacloud.nasa.gov/. MODIS measures spectral emissivity through four channels (28, 29, 30, 31) at wavelengths ranging between 8-12 μm (Jin and Liang 2006) and the system of equations is iteratively solved for a given range of wavelengths (8 - 12 μm) to obtain ϵ and LST using radiative transfer models (Hulley, Hughes, and Hook 2012; Jin and Liang 2006;

Table 2.1: Description of study sites

Study site	Latitude, Longitude	Landcover	Time-period	Longwave sensors	Sensor installation height (m)	Altitude (m)
Adelaide River **(AR)**	13.0769, 131.1178	Savanna dominated by Eucalyptus tectifica and Planchonia careya	2006-09	Pyrgeometers (CNR1)	15	90
Alice Springs **(AS)**	22.2828, 133.2493	Mulga woodland, hummock grassland, river red gum forest	2016-18	Radiometer (CNR1)	12.2	606
Brookings **(BR)**	44.352, 96.840	Cropland	2005	Pyrgeometers	NA	510
Daly Uncleared **(DU)**	14.1592, 131.3881	Woodland savanna	2016-18	Radiometer (NRlite)	21	110
Howard Springs **(HS)**	12.4943, 131.1523	Open woodland savanna	2016-18	Pyrgeometers (CM3 and CG3)	23	63
Litchfield **(LF)**	13.1790, 130.7945	Tropical savanna	2016-18	Radiometer (CNR4)	31	222
Sturt Plains **(SP)**	17.1507, 133.3502	Mitchell Grass	2016-19	Pyrgeometers (CG-2)	4.8	230
Ti Tree East **(TT)**	22.2870, 133.6400	Grassy mulga woodland, Corymbia/ Triodia savanna	2016-18	Radiometer (CNR1)	9.9	553
Tumbarumba **(TUM)**	35.6566, 148.1517	Wet sclerophyll	2015-18	Pyrgeometers (CM3 and CG3)	70	1200
Yatir Forest **(YF)**	31.3448, 35.0519	Evergreen need-leaf forest	2005	Pyrgeometers	NA	641

Wang and Liang 2009). In the current study, dataset columns used to compare plot-scale LST are day-time daily LST and local view time. In order to obtain landscape-scale ϵ, the emissivity from bands 31 and 32 are used. These bands have stable emissivities than other channels ranging from 0.92-1, and can be used to derive broadband emissivity (Wan 2007).

Plot-scale ϵ and LST estimation: LST is defined as the "ensemble directional radiometric surface temperature" (Norman and Becker 1995), and can be estimated from the infrared radiance emanating from a given surface with known emissivity (Kustas et al. 2007). The emissivity at ecosystem-scale can also be estimated using observed H, R_{lup}, R_{ldwn}, and T_a. A plot-scale ϵ (ϵ_{plot}) estimation approach was initially proposed by Holmes (Holmes et al. 2009) using the short equation (Eq. (2.10)). In the present

work, we have used both the long equation (Eq. (2.6)) and the short equation (Eq. (2.10)) to estimate ϵ_{plot}. The prime variables used in the study are H, R_{lup}, R_{ldwn}, and T_a, whereas the ancillary variables R_{net} and wind speed (W_s) are used to filter the data for analysis. The data filtering criteria are sufficient net radiation ($R_{net} > 25\ W\ m^{-2}$) and wind speed ($W_s > 2\ m\ s^{-1}$) (Holmes et al. 2009). For each month, a linear regression (with and without intercept) between sensible heat (H) and ($T_s - T_a$) is performed (Fig. 2.1b) using Scipy (https://docs.scipy.org/doc/scipy/reference/generated/scipy.stats.linregress.html). T_s is estimated by solving Eq. (2.6) and Eq. (2.10) using measured longwave radiation and prescribed ϵ, starting with the maximum possible value for a grey body, 0.99, and then progressively reducing ϵ with step size of 0.002 until we reach a minimum root mean square error (RMSE) for a linear relationship between H and ΔT. Only months with coefficient of determination (R^2) > 0.5 between H and ΔT are considered for ϵ_{plot} estimation. An illustration plot for RMSE as a function of ϵ is shown in Fig. A.5. The monthly ϵ_{plot} is obtained using the long (Eq. (2.6)) and short equation (Eq.(2.10)) and termed as ϵ_{leq} and ϵ_{seq} respectively, as shown in Fig. 2.1b. For two sites with a high value of intercept (HS and LF in Table 2.2) we tested if adding 6-8% to the observed R_{lup} and closing the energy balance using Bowen ratio closure before ϵ_{plot} estimation would remove the intercept (Fig. 2.6).

Recently, another approach for plot-scale ϵ estimation using Eq. (2.4) was used by Maes et.al (2019) (Maes et al. 2019). In this approach, data sets are filtered for non rainy days without snow cover ($\alpha < 0.4$) and near-zero H ($-2 < H < 2$). The ϵ values are then estimated by substituting $T_s = T_a$ in Eq. (2.4) as shown in Eq. (2.11). The monthly ϵ was obtained as the median of ϵ obtained by substituting filtered data in Eq. (2.11) (red stars in Fig. 2.2).

$$\epsilon = \frac{R_{ldwn} - R_{lup}}{R_{ldwn} - T_a^4 \sigma} \tag{2.11}$$

LST comparison: MODIS LSTs are a global reference for LST and used world-wide, also in conjuction with plot-scale flux measurements. To calculate plot-scale LST for the exact time of TERRA day-time overpass for each site, the 30 minute tower data was interpolated linearly, and the interpolated R_{ldwn} and R_{lup} observations corresponding to the time of overpass were used in conjunction with the monthly ϵ_{plot} or ϵ_{MODIS} for the calculation. Plot-scale daily LST is compared to MODIS LST in terms of the mean, bias, RMSE and R^2 using a robust linear regression model (scipy stat model) as shown in Fig. 2.1a. The goodness of fit between plot-scale and landscape-scale LST was determined by looking at R^2 (Fig. 2.1b). The bias is estimated as the mean of the deviation between daily MODIS LST and plot-scale T_s.

General approach: We estimate landscape-scale broadband ϵ using MODIS spectral

ϵ as shown in Bahir et. al (Bahir et al. 2017).

$$\epsilon_{MODIS} = 0.4587\epsilon_{31} + 0.5414\epsilon_{32} \tag{2.12}$$

Tower-based longwave radiation measurement (R_{lup}, R_{ldwn}) passing the filtering criteria (as mentioned in plot-scale emissivity estimation) along with MODIS based ϵ was used to invert LST using Eq. (2.6) and Eq. (2.10). The obtained plot-scale LST was compared to landscape-scale MODIS LST using a robust linear regression as mentioned above and shown in Fig. 2.1a.

Uncertainty estimation: Uncertainty in plot-scale ϵ and LST was quantified based on an assumed systematic error (caused by a potential bias in measurement devices) at the study sites. In a first step, based on the literature (Trenberth and Fasullo 2012; Foken 2008), the error bounds of each input variable (H, R_{lup}, R_{ldwn}, T_a) used for plot-scale ϵ estimation were defined. The error bounds for R_{lup} and R_{ldwn} are -5 to 5 $W\ m^{-2}$ (Trenberth and Fasullo 2012), for H, we used -20 to 20 $W\ m^{-2}$ and for T_a we used -1 to 1 K (Foken 2008). The error samples (perturbation) within these bounds were generated using the Saltelli sampling scheme (using the python package SALib (Saltelli et al. 2017)). Each error sample is added to the monthly segregated measured fluxes as explained above. Observed fluxes combined with perturbed fluxes are used to estimate T_s using Eq. (2.10) and Eq. (2.6). The obtained range of diurnal T_s and observed T_a based on the perturbation is used to calculate the uncertainty in ΔT; an example for July 15 is shown in Fig. 2.7c. Perturbed sensible heat flux (H+sample error) and perturbed ΔT is used to obtain ϵ_{plot} as described above. The distribution of monthly ϵ_{plot} values is reported as uncertainty in monthly ϵ.

2.3 Results

2.3.1 Plot-scale ϵ using long and short equation

Following the method proposed by Holmes et al. (Holmes et al. 2009; Holmes et al. 2016), plot-scale monthly ϵ was estimated at the study sites by fitting ϵ to minimise the RMSE of the regression between H and $T_s - T_a$ (see Fig. A.3). In Fig. 2.2a, c, and d, we used the original data and reproduced Figs. 2a, 3C, and 3Q from Holmes et al. (2009) (Holmes et al. 2009) to validate our interpretation of their approach using the short equation (Eq. (2.10)). We noted only marginal differences between the two results based on the short equation, which are likely due to different fitting algorithms. The replication of the $H(\Delta T)$ plot using the long equation (Eq. (2.6)) with the same data is given in Fig. 2.2b and the monthly ϵ values are shown in Fig. 2.2c, d, indicated by blue stars. The retrieved LST values were slightly higher when using Eq. (2.6) (compare

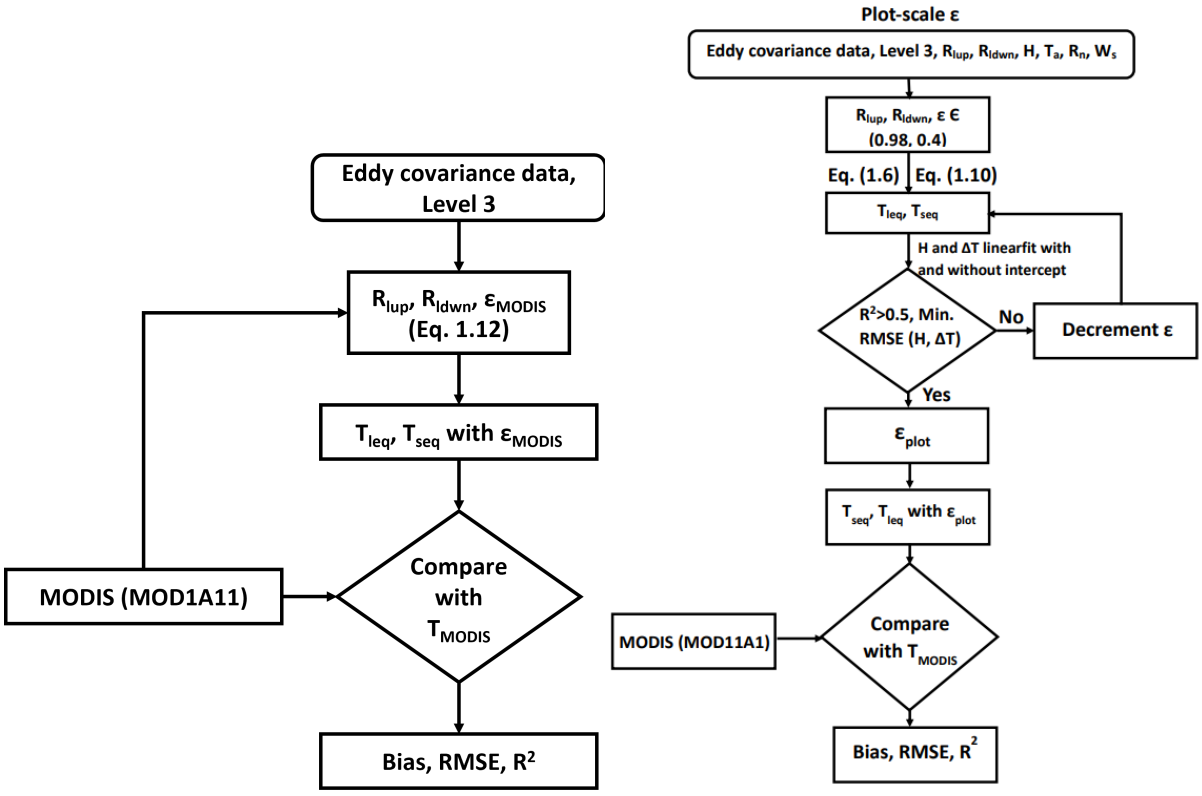

Figure 2.1: Schematic representation of steps followed for plot-scale LST retrieval using landscape-scale emissivity (a) or plot-scale emissivity (b). To estimate plot-scale ϵ_{plot}, surface-air temperature difference (ΔT) is computed from observed longwave radiation (R_{lup} and R_{ldwn}) and T_a for given ϵ_{plot}, and then ϵ_{plot} is varied in a way to minimise RMSE of a linear relationship between observed sensible heat flux (H) and ΔT. The resulting surface temperatures (T_{leq}, T_{seq}) are then compared to T_{MODIS}, with the R^2, RMSE, and bias reported in Fig. (2.4).

a and b in Fig. 2.2). The use of the long equation (Eq. (2.6)) resulted in substantially (10%) lower values of ϵ as compared to the values estimated by Holmes et al. (Holmes et al. 2009) for the common study sites (BR, Fig. 2.2c and YF, Fig. 2.2d). The reduction in ϵ can be attributed to the sensitivity of the two equations to the emissivity. As shown in Fig. A.4, the T_s estimation using the short equation is more sensitive to ϵ than for the long equation, thus even a small reduction in ϵ can lead to a large increase in the T_s (to minimise RMSE).

Another approach for plot-scale ϵ estimation (Maes et al. 2019) in combination with Eq. (2.6) resulted in even lower ϵ values for BR, as shown in Fig. 2.2c (red stars), whereas at YF, this approach gave an ϵ value higher than 1 (red star in Fig. 2.2d). Note that the long equation also yielded an acceptable H ΔTrelationship for more months at YF (blue stars) than the short equation (black dots), as shown in Fig. 2.2d. The pattern of lower ϵ and higher LST using the long equation compared to the short equation was confirmed for all the ten sites used in the present study (Table A.1).

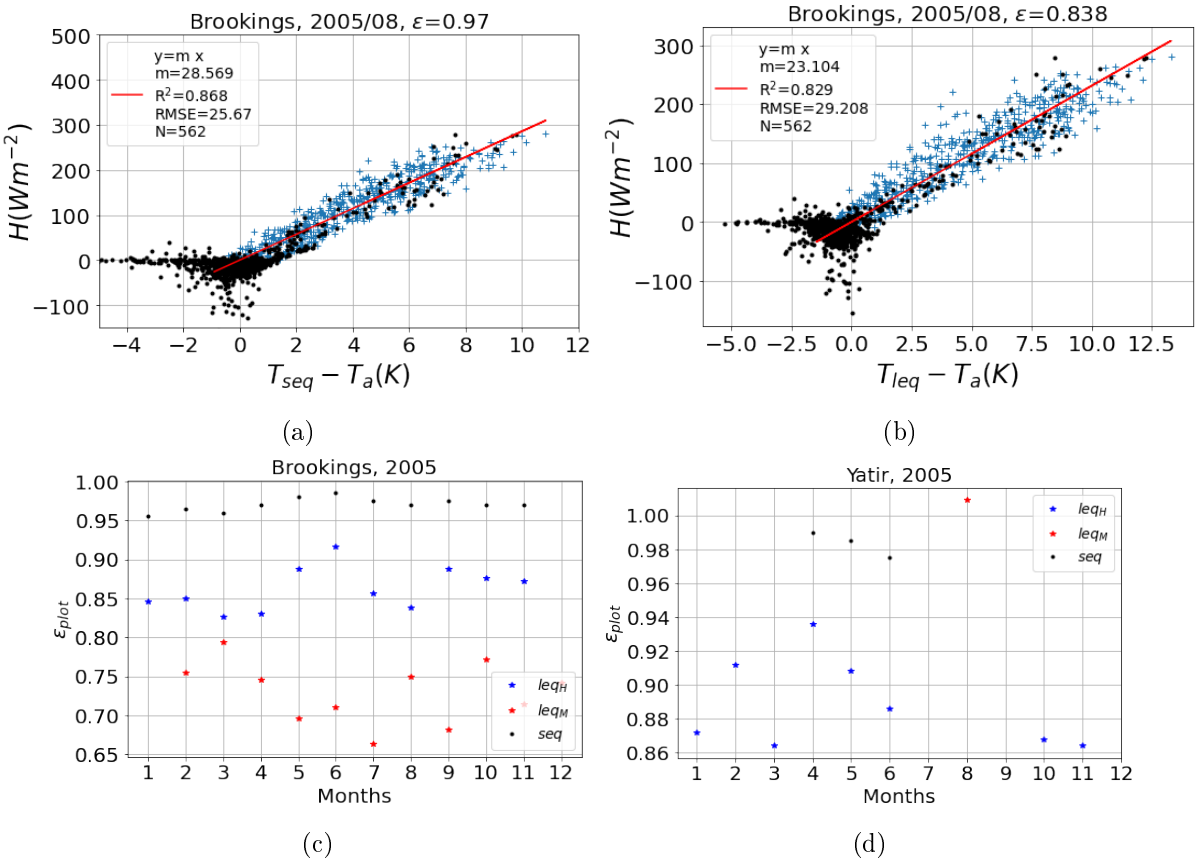

Figure 2.2: Reproduction of analysis presented in Figs. 2a, 3c, and Q in Holmes et al. (Holmes et al. 2009). **(a)** Sensible heat (H) vs $\Delta T = T_{seq} - T_a$ based on the short equation (T_{seq}, Eq. (2.10)); (b) H vs. ΔT based on the long equation (T_{leq}, Eq. (2.6)). Both show data for August 2005 at BR. Blue crosses represent data points satisfying the filtering criteria, while black dots represent points not considered in the analysis. N is the number of blue crosses used for regression (red line), m is the slope of regression, RMSE is the root mean square error and R^2 is the square of the coefficient of determination. The fitted ϵ value is reported in the title. **(c)** Optimised ϵ values at BR obtained for the months where $R^2 > 0.5$ using the short equation (Eq. (2.9), black dots) and long equation (Eq. (2.6), blue stars), and ϵ obtained using the approach of Maes et. al (Maes et al. 2019) (red stars). **(d)** Same as (c), but for YF.

2.3.2 Landscape-scale vs plot-scale estimates of ϵ and LST

At each site, LST was estimated using both the short equation (T_{seq}, Eq. (2.10)) and the long equation (T_{leq}, Eq. (2.6)). In the first step, tower-based longwave radiation and landscape-scale broadband ϵ from MODIS spectral ϵ (ϵ_{MODIS}, Eq. (2.12)) was used. The yearly daytime surface-to-air temperature difference for each study site is estimated and shown in Fig. 2.3. At all sites, Eq. (2.10) resulted in higher day-time plot-scale T_s estimates as compared to Eq. (2.6), when using ϵ_{MODIS}, with the medians of surface-to-air temperature differences (ΔT) differing by 0.8 to 1.5 K (Fig. 2.3). The difference in ΔT using the two equations is highest at the water limited sites, e.g. AS and YA. Note that for two sites (LF and HS), the median values of daytime ΔT are negative. Comparison of plot-scale LST estimated using ϵ_{MODIS} at satellite overpass time with landscape-scale LST (T_{MODIS}) revealed strong correlations at most of study sites but systematically lower

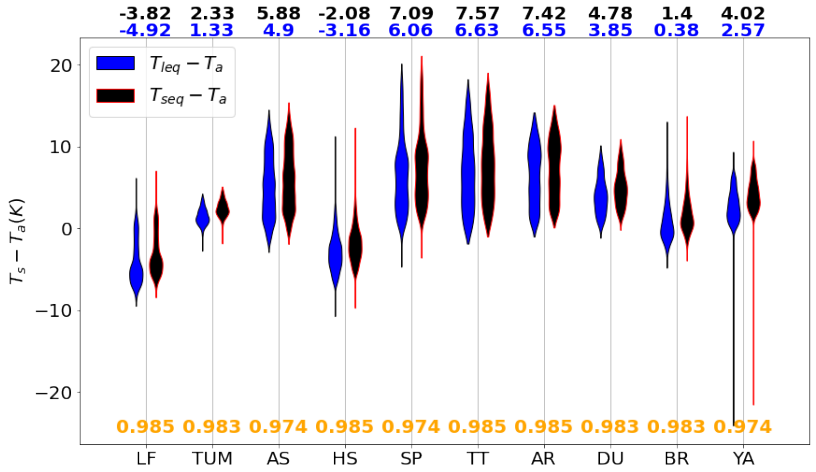

Figure 2.3: Yearly distributions of half-hourly surface-to-air temperature differences ($\Delta T = T_s - T_a$) for a representative year at each site. LST was calculated using the short equation (Eq. (2.10)) or long equation (Eq. (2.6)) with landscape-scale emissivity (ϵ_{MODIS}). The median values of ΔT are shown at the top of the plot and the ϵ_{MODIS} values used for the T_s retrieval are shown at the bottom in orange. See Table 2.1 for site abbreviations. The shapes of the violin represent the distributions of ΔT values.

plot-scale LST (Fig. 2.4a, b). Use of ϵ_{plot} for LST estimation (T_{seq} and T_{leq}) resulted in substantial reduction of the bias as shown in Fig. 2.4c, d. This trend in bias reduction was similar at other sites (Table A.1 for details). The minimum bias is found at TUM, a closed canopy (eucalyptus forest) and the highest bias was obtained at LF and HS, heterogeneous ecosystems with sparse canopies (woodland savanna). However, for some sites, weak correlation between satellite-derived and local LST estimates were also evident (at DU, R^2 was reduced from 0.8 to 0.4, see Table A.1). The low correlation between MODIS LST and plot-scale LST can be due to various reasons, such as differences in sensor types, viewing angles and distance between the sensors and sources, e.g. requiring atmospheric correction for satellite-based sensors. Also, using plot-scale ϵ for LST estimation resulted in positive $T_s - T_a$ at LF and HS as shown in Fig. A.1 in comparison to Fig. 2.3.

2.3.3 Plot-scale ϵ estimation using long equation with intercept

In order to account for the possibility of bias between radiometric and aerodynamic measurements (e.g. due to footprint mismatch of measuring devices or instrument bias), we also fitted Eq. (2.8), i.e. a relationship allowing for an intercept in the linear fit between H and ΔT (instead of forcing it through zero as in Fig. 2.2) for plot-scale ϵ estimation. As shown in Fig. 2.5, the plot-scale ϵ values resulting from this approach ($H = m\Delta T + c$) were substantially closer to the landscape-scale ϵ values compared with the approach without intercept ($H = m\Delta T$), as shown in Table 2.2. However, comparison of the resulting plot-scale LST with landscape-scale LST values revealed an increase in bias at most sites compared to the LST obtained using ϵ_{plot} without an intercept (Table 2.2). The median values of the resulting intercept ranged from -24 to

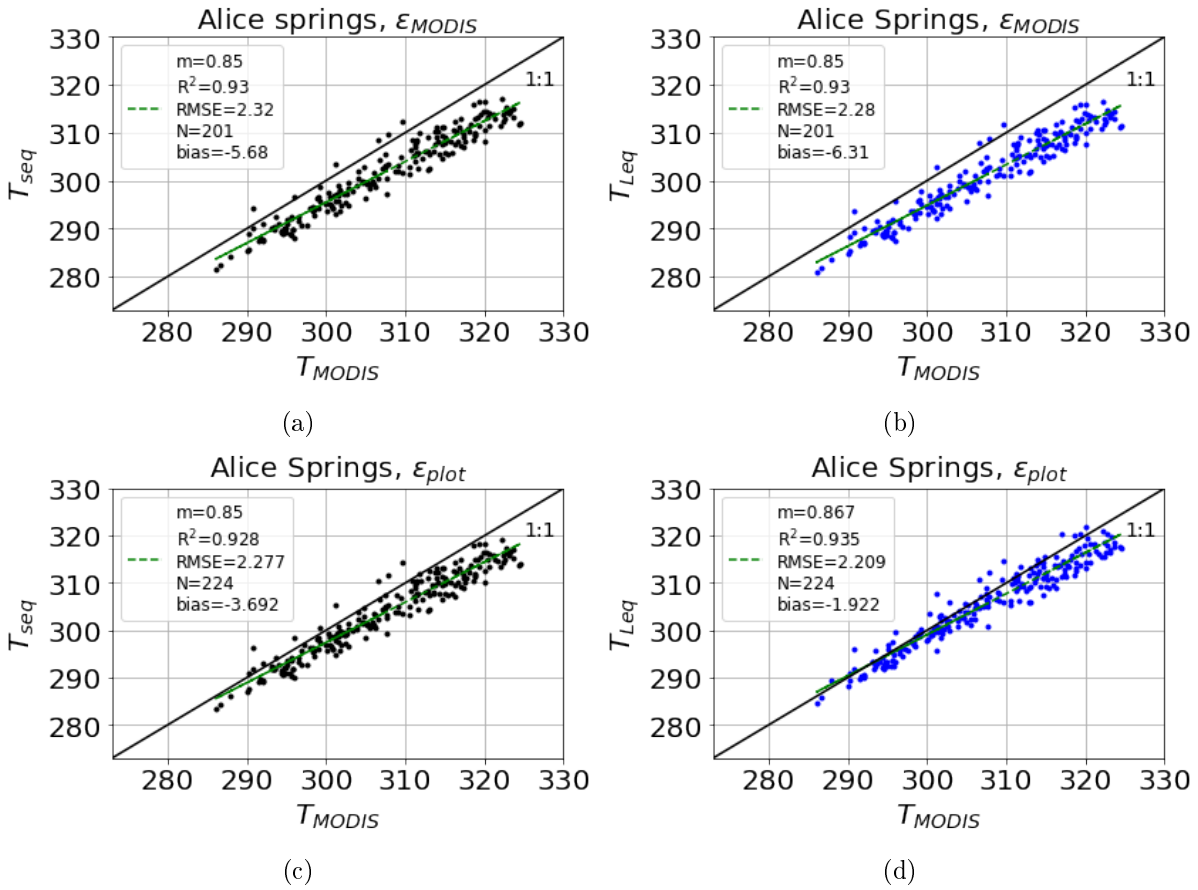

Figure 2.4: Landscape-scale LST (T_{MODIS} derived from MOD11A1) vs. plot-scale LST at AS for 2016-2018. **(a)** T_{seq} based on short equation (Eq. (2.10)) and satellite-derived (MODIS) broadband emissivity; **(b)** Same as (a), but T_{leq} based on long equation (Eq. 2.6); **(c)** T_{seq} based on short equation (Eq. (2.10)) and monthly plot-scale emissivity; **(d)** Same as (c), but T_{leq} based on long equation (Eq. (2.6)). Bias is mean $T_{seq} - T_{MODIS}$, N is the number of daily overpasses of MODIS between 2016 and 2018, c is the intercept, m the slope, RMSE is the root mean square error and R^2 is coefficient of determination. At each site, LST was estimated using both the short equation (T_{seq}, Eq. (2.10)) and the long equation (T_{leq}, Eq. (2.6)). In a first step, we used satellite-derived landscape-scale broadband emissivity from MODIS (ϵ_{MODIS}, Eq. (2.12)) for estimating plot-scale LST from tower-based longwave measurements, and compared these with landscape-scale LST extracted from MODIS LST dataset (T_{MODIS}).

+258 $W\ m^{-2}$, with the highest intercept values at HS (amounting to 70% of the maximum observed H at this site). The minimum value of intercept was obtained at TUM (5% of the maximum observed H). Note, that if we assumed just a slight under-estimation of upwelling longwave radiation by 40 $W\ m^{-2}$ at HS (ca. 8% of observed R_{lup}), the intercept was reduced from 294 (Fig. 2.5c) to 17 $W\ m^{-2}$ (Fig. 2.6a) without change in other regression parameters (m, RMSE, R^2). In this study, we did not apply any energy balance closure scheme, as a Bowen ratio closure, although resulting in higher R^2 values at HS, also led to even greater intercept (c) (Fig. 2.6b). Interestingly, adding 40 $W\ m^{-2}$ to the measured upwelling longwave radiation and subsequent energy balance closure largely removes the intercept and at the same time increases R^2, as shown in Fig. A.6. Also, the bias between MODIS and plot-scale LST is reduced from -10.66 K (Table 2.2)

to 4.01 K by adding 40 $W\ m^{-2}$ and closing the energy balance.

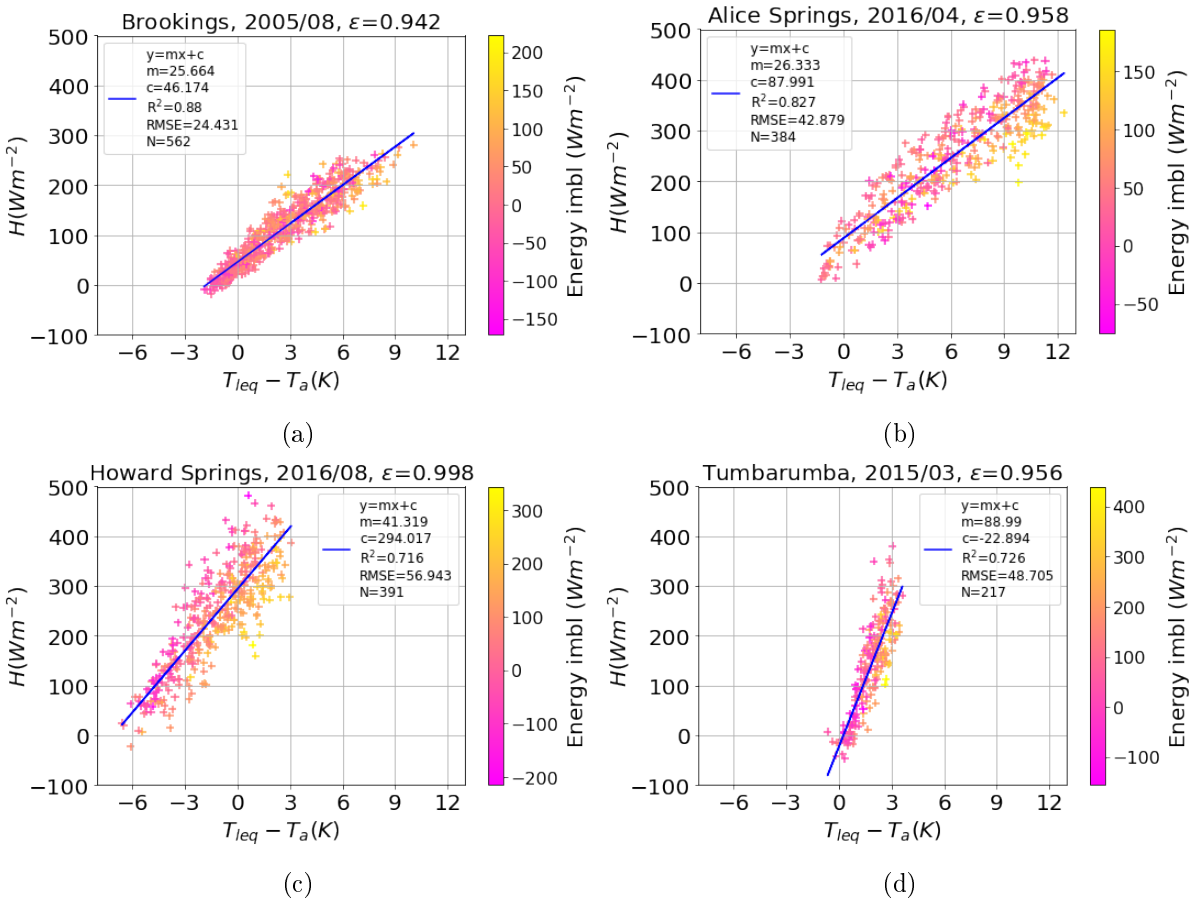

Figure 2.5: Sensible heat flux as a function of surface-to-air temperature difference based on Eq. (2.8) ($H = m(T_s - T_a) + c$). ϵ was fitted to minimise RMSE of a robust linear regression. The title of the plot contains site, year, month and the fitted ϵ-value. The legend correspond to Fig. 2.2. The colour code indicates the degree of energy imbalance of each data point (i.e. $R_{net} - H - LE - G$).

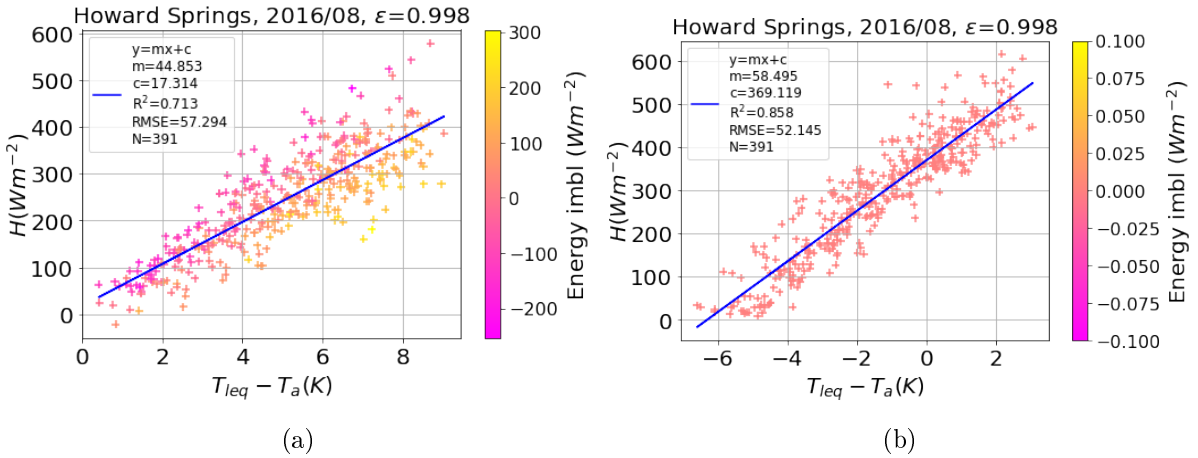

Figure 2.6: Sensible heat flux as a function of surface-to-air temperature difference based on Eq. (2.8) ($H = m(T_s - T_a) + c$). Same analysis and legends as in Fig. 2.5c), but (a) After adding 40 $W\ m^{-2}$ to measured R_{lup}, and (b) after closing the energy imbalance using a Bowen ratio closure scheme.

Table 2.2: Correspondence between daytime landscape-scale LST (T_{MODIS}) and plot-scale LST (T_s) (estimated at TERRA time of pass), using different emissivity estimates. The emissivity values used to retrieve plot-scale LST is either taken from MODIS (ϵ_{land}), or derived flux tower data (ϵ_{plot}), using Eq. 2.7 ($H = m\Delta T$) or Eq. 2.8 ($H = m\Delta T + c$). The reported ϵ_{plot} and intercept (c) are median values over all months for each site. Bias is defined as the mean of $T_s - T_{MODIS}$, R^2 is the coefficient of determination between plot-scale LST in comparison to landscape-scale LST. The site acronyms are explained in Table 2.1.

Sites	Landscape-scale ϵ			Plot-scale ϵ $H = m\Delta T$			Plot-scale ϵ $H = m\Delta T + c$			
	ϵ_{land}	R^2	bias (K)	ϵ_{plot}	R^2	bias (K)	ϵ_{plot}	R^2	bias (K)	c (Wm^{-2})
SP	0.974	0.81	-4.61	0.85	0.82	-1.91	0.92	0.774	-2.563	18.12
AS	0.974	0.93	-6.24	0.82	0.93	-1.92	0.993	0.915	-4.884	72.46
TT	0.974	0.57	-8.30	0.80	0.52	-4.02	0.939	0.521	-7.466	58.70
HS	0.985	0.16	-9.90	0.6	0.22	-2.47	0.949	0.18	-10.45	237.29
LF	0.985	0.41	-11.0	0.6	0.41	-2.57	0.968	0.378	-11.47	258
AR	0.985	0.27	-3.51	0.960	0.252	-2.98	0.996	0.27	-3.567	14.72
DU	0.985	0.81	4.61	0.985	0.425	-3.926	0.994	0.405	-4.603	-8.11
TUM	0.983	0.84	-2.10	0.97	0.89	-1.93	0.955	0.85	-1.696	-24.24
BR	0.983	0.937	-0.195	0.82	0.895	2.72	0.919	0.906	1.662	17.72
YA	0.974	0.855	-3.45	0.93	0.793	-0.582	0.873	0.826	0.073	-22.95

2.3.4 Uncertainty in plot-scale ϵ and LST

Each of the observed input variables used for the estimation of plot-scale ϵ and LST has an associated uncertainty. Here we present exemplary results for Alice Springs (AS), which showed the highest correlation between plot-scale and landscape-scale LST estimations (Table 2.2). The uncertainty in plot-scale ϵ estimated using Eq. (2.6) ('leq') and Eq. (2.7) (i.e. without intercept in H vs ΔT was mainly in the range of ± 0.02 to ± 0.05, with a maximum of ± 0.2 if outliers are included (blue color in Fig. 2.7a). The short equation (Eq. (2.10), 'seq') resulted in a vary narrow range of ϵ values between 0.94 and 0.99 throughout the year, with very small uncertainty (around ± 0.01, black boxes in Fig. 2.7a). Interestingly, the differences in ϵ uncertainty did not propagate into differences in LST uncertainty, which were around ± 0.2 K at the hourly scale for each equation if plot-scale emissivity was used (blue boxes in Fig. 2.7b and black boxes in Fig. 2.7c). In fact, if landscape-scale values of ϵ were used, the LST uncertainty was even bigger (± 0.5 K, orange boxes in Fig. 2.7b and c). However, if an intercept in the H vs ΔT relationship was allowed during estimation of ϵ_{plot}, the uncertainty in ϵ_{plot} largely vanished (Fig. A.6a), while the uncertainty in $T_s - T_a$ at the diurnal scale doubled (Fig. A.6b).

2.4 Discussion

Our analysis revealed a fundamental flaw in the commonly used short equation (Eq. (2.10)) for estimating plot-scale LST and ϵ_{plot}, as it does not produce the same results as the long equation (Eq. (2.6)) even with high values of ϵ_{MODIS}. In fact, the short

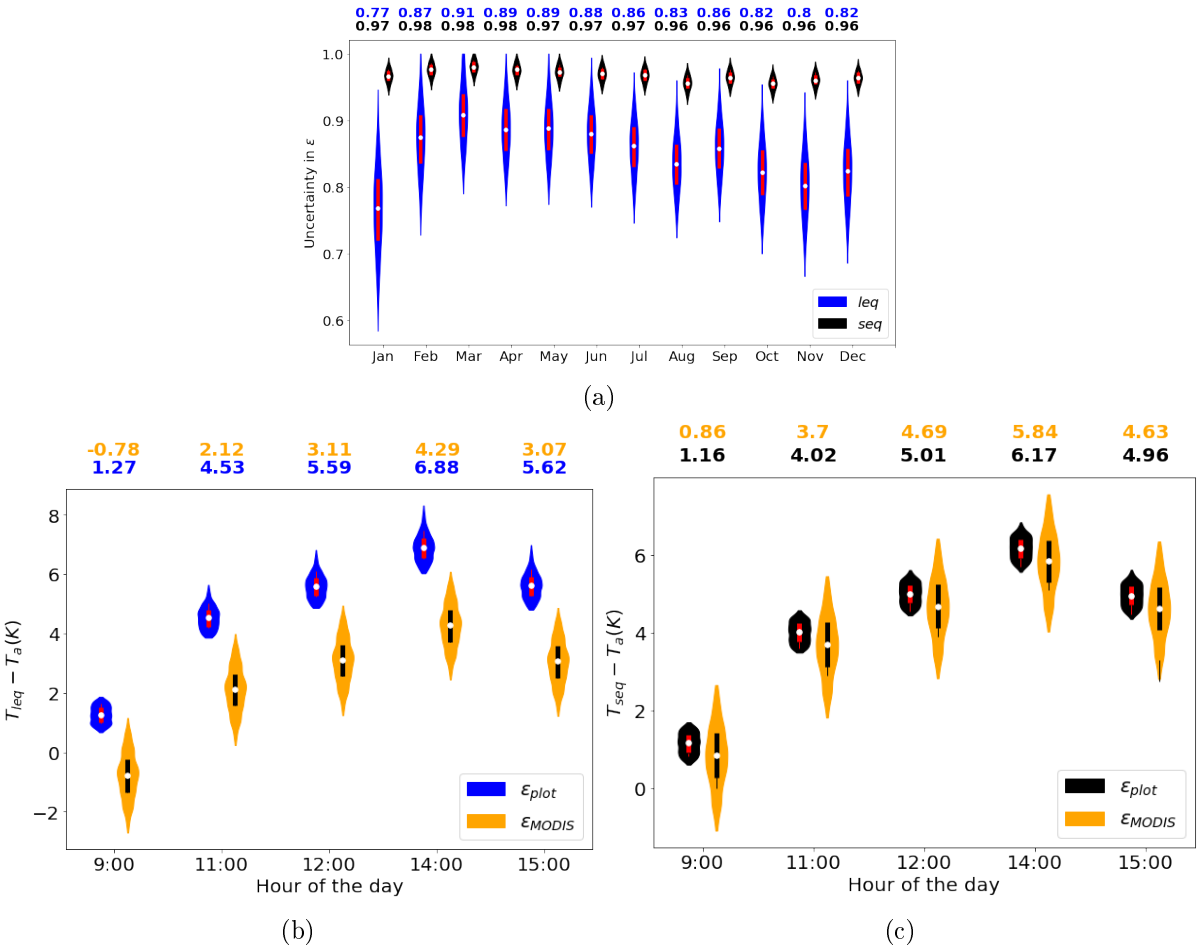

Figure 2.7: Uncertainty in plot-scale estimations of ϵ and surface-air temperature differences ($T_s - T_a$) at AS, based on Eq. (2.7) (no intercept in H vs ΔT). Monthly values of ϵ shown for 2017 and hourly $T_s - T_a$ for 15 August 2017. **(a)** Uncertainty in monthly ϵ_{plot} due to uncertainty in H, R_{lup}, R_{ldwn} and T_a, using Eq. (2.5) (leq, blue) and Eq. (2.9) ('seq', black). **(b)** Hourly uncertainty in $T_s - T_a$ on 15 July based on Eq. (2.5), due to uncertainty in R_{lup}, R_{ldwn} and T_a when landscape-scale emissivity is used (ϵ_{MODIS}, orange) or due to uncertainty in H, R_{lup}, R_{ldw} and T_a when ϵ_{plot} is used (blue). **(c)** Same as (b), but based on Eq. (2.9). The white dots represent the median values of each distribution, the bars extend between the 25 and 75% quantiles and the outermost violin represent the full distributions of the data.

equation strongly over-estimates the sensitivity of LST to ϵ (Fig. A.4), as it neglects the fact that low emissivity results in a greater fraction of reflected longwave in the sensor signal (compare Eq. (2.10) and (2.6)). The sensitivity of the long equation (Eq. (2.6)) to ϵ is driven by the contrast between R_{lup} and R_{ldwn}, whereas for the short equation (Eq. (2.10)), it is only driven by observed R_{lup} (Fig. A.2). For instance, an error of 0.01 in ϵ at a water-limited site (e.g. AS) can cause an error of 0.17 K using Eq. (2.6) and 0.79 K using Eq. (2.10) respectively (Fig. A.4). This means that small errors in ϵ can result in large differences in LST when using the short equation, or conversely, unrealistic LST values can conveniently be rectified by slightly changing the ϵ value. This is illustrated e.g. in Fig. 2.7, where estimation of ϵ_{plot} resulted in similar LST values between the short and long equations, but with vastly different ϵ values and much greater uncertainty

in estimated ϵ using the long equation compared to the short equation. Considering that the short equation ignores an important component of longwave radiation, it must be concluded that in this case, it achieves seemingly the right results for the wrong reasons. The reduced sensitivity of the long equation (Eq. (2.6)) to ϵ is of advantage for plot-scale LST estimation, since ϵ_{plot} is usually unknown and therefore used as an approximate value (Mallick et al. 2018b). However, when using the long equation in conjunction with plot-scale H measurements to estimate ϵ_{plot}, we obtained unrealistically low ϵ values at some sites (e.g. HS and LF, Table 2.2) in comparison to previously reported ϵ values for a soil-vegetation system (Sugita and Brutsaert 1996; Snyder et al. 1998). This strong bias in plot-scale ϵ estimates was largely removed if H vs ΔT linearfit was allowed to have an intercept (Table 2.2, plot-scale ϵ). The intercept (i.e. $\Delta T \neq 0$ at $H = 0$) could be caused by combining measurements coming from instruments (radiometer, eddy covariance system) with different footprints (Marcolla and Cescatti 2018). The mismatch of source areas becomes important if the surface underlying the instruments has heterogeneous land cover. Although "footprint awareness" is often omitted at ECS under the assumption of homogeneity (Chu et al. 2021), in patchy vegetation, the radiometer can be "seeing" a different vegetation fraction than that contributing to EC measurements, meaning that $H \neq 0$ at $\Delta T = 0$. This problem was not detected by Holmes et al. (Holmes et al. 2009), as the short equation (Eq. (2.10)) was used, and due to its high sensitivity to ϵ (Fig. A.4a) even a small reduction in ϵ corrected the offset in H vs ΔT (Fig. 2.2a). In contrast, when repeating the same analysis using the long equation (Eq. (2.6)), a larger reduction in ϵ is required to remove the intercept, resulting in lower ϵ (Fig. 2.2b). By allowing an intercept in the H vs ΔT linear fit, we implicitly account for the possibility of a footprint mismatch or instrument bias in the data. This small change in methodology enables us to detect such problems by inspecting the value of the intercept (c). Considering the aerodynamic footprint to be larger than the radiometric footprint (Marcolla and Cescatti 2018; Chu et al. 2021), a positive intercept can be interpreted as the H from the aerodynamic footprint which is not seen by the radiometer.

The intercept was very high for the sites HS and LF (Table. 2.2). A close inspection of the H vs ΔT plots at these sites (Fig. A.1) revealed negative day-time $T_s - T_a$ (Fig. 2.3), which may suggest an underestimation of R_{lup}. While testing this hypothesis at HS (having the highest intercept, Fig. 2.5c) we found that adding roughly 40 $W\ m^{-2}$ (approx. 8% of observed R_{lup}, Fig. 2.6 in observed R_{lup} led to significant reduction in the intercept from 294 $W\ m^{-2}$ (Fig. 2.5c) to 17 $W\ m^{-2}$ and positive day-time $T_s - T_a$ (Fig. 2.6a). The other linear regression parameters (m, R^2, RMSE) were not affected (compare Fig. 2.6a and Fig. 2.5c). The hemispherical view of the radiometers looking down at a heterogeneous canopy makes it possible that they "see" more tree crowns and less soil than the area contributing to the EC footprint. This could lead to an underestimation of R_{lup}, and an underestimation by $30 - 40\ W\ m^{-2}$ would be equivalent to approximately

5-10% of the observed flux, which is within the range of a typical energy imbalance found at this site. Previous studies have found a dependence of footprint mismatch on wind direction (Chu et al. 2021; Marcolla and Cescatti 2018; Morillas et al. 2013), but we did not find a significant relation between monthly intercept and dominant wind direction at HS.

Surface heterogeneity has also been recognized as one of the potential causes for the lack of energy balance closure observed at most ECS at diurnal scales (Wilson et al. 2002; Stoy et al. 2013). However, in our analysis the use of an energy balance closure scheme (based on the Bowen ratio) led to much lower values of ϵ_{plot} using Holmes approach with the long equation and without intercept. In contrast, if an intercept was allowed, energy balance closure led to an increase in positive intercept (Fig. 2.6b). Perhaps this is the reason why other studies on plot-scale ϵ estimation have also used the observed fluxes without correction (Holmes et al. 2009; Holmes et al. 2016; Maes et al. 2019). Other energy balance closure schemes add the missing energy to H in water limited ecosystems (Twine et al. 2000), or to LE in energy limited ecosystems (Chakraborty et al. 2019). However, our analysis suggests that the footprint mismatch may cause a small bias in the upwelling longwave radiation measurements that is not accounted in any conventional energy balance closure approaches. When we added 35 $W\ m^{-2}$ (instead of 40 $W\ m^{-2}$, see Fig. 2.6a) to the measured upwelling longwave radiation and subsequently closed the energy balance at the HS site (which had the largest H vs ΔT intercept), we largely removed the intercept and at the same time obtained realistic ϵ values and an increased R^2 (Fig. A.6). In addition, the bias between MODIS LST and plot-scale LST at HS was reduced by 6.4 K (Fig. A.6b), compared to using upwelling longwave without correction.

When estimating plot-scale LST using ϵ_{MODIS} values, we found at many sites with a sparse canopy strongly negative bias in comparison to MODIS LST, which is in agreement with previous studies where the bias for sparse canopies reached up to 12 K (Guillevic et al. 2018). The MODIS overpass can have a large off-Nadir viewing angle, which would lead to an elongated foot-print (Margulis, Liu, and Baldo 2019) and therefore, a different distribution of bare soil and vegetated areas compared to the mostly Nadir viewing angle of the tower-mounted sensor. The difference in footprint and viewing angles between the tower mounted pyrgeometers and MODIS radiometers could also be the reason for bias between the two LST estimates. Plot-scale LST estimates based on plot-scale ϵ using a linear H vs ΔT fit without an intercept largely reduced this bias between plot-scale and MODIS LST (Table 2.2) and also reduced the uncertainty in diurnal LST (Fig. 2.7b, c) in comparison to the use of ϵ_{MODIS}. However, the resulting plot-scale ϵ values were unrealistically low at some sites (Table 2.2, center). In contrast, allowing an intercept ($H = m * \Delta T + c$) in ϵ_{plot} estimation resulted in more realistic ϵ values at these sites, but very large intercept values (over 200 $W\ m^{-2}$ at some sites), indicating that the plot-scale LST values cannot be used in combination with the observed

aerodynamic fluxes at these sites, as strongly positive H at 0 surface-air temperature difference is physically inconsistent (Fig. 2.5c). In addition, this approach increased the bias between plot-scale and MODIS LST at most of the study sites (Table 2.2). Note that the correspondence between landscape-scale LST and plot-scale LST can vary strongly between sites, depending on canopy densities and viewing angles (tower vs. satellite) (Margulis, Liu, and Baldo 2019), sensor installation height and position, and sensor types (Marcolla and Cescatti 2018). At the sites with the largest intercept values, we found that an assumed bias in upwelling longwave radiation by only 6-9% would largely remove the intercept and also reduce the bias between MODIS and plot-scale LST (Fig. 2.6a, Fig. A.6b). A detailed analysis of such bias and potential correction approaches is beyond the scope of this study. Given that the fit of a linear model without intercept is statistically questionable in general (Eisenhauer 2003), and the fact that such a fit resulted in unrealistically low values of ϵ at some sites, we conclude that fitting a model with intercept is the more robust approach, and that a significant intercept should be used as a red flag for the utility of the data for estimation of plot-scale LST. Additionally, the uncertainty in ϵ_{plot} values obtained using a regression model with intercept nearly vanished in comparison to the uncertainty resulting from a regression model without intercept (see Fig. A.6a).

Note that the fluxes observed at ECS are representative of the composite signal from both, soil and vegetation, which typically have different ranges of surface temperatures and emissivities (Jin and Liang 2006). The ϵ of soil strongly depends on soil moisture content (Mira et al. 2007), whereas the ϵ of a canopy depends on its structural attributes and leaf area index, the latter of which can vary strongly at the seasonal scale (Chen 2015). For example, the laboratory-measured directional ϵ for various canopy elements (bark, leaf and its arrangement, stem wood) ranged between 0.9 to 1 at the YF (Vishnevetsky et al. 2019). Laboratory measurements of thermal infrared reflectance spectra suggest that the ϵ uncertainty due to structural unknowns, such as leaf orientation, is more significant than the differences in leaf component emissivity among plant species (Snyder et al. 1998). Consequently, it is clear that the ϵ of a surface is a function of many factors and a detailed analysis of all these factors is out of scope of the present study. Derivation of landscape-scale broadband emissivity (ϵ_{MODIS}) from narrowband spectral emissivity is a first-order approximation for capturing the integrated effects of land cover from MODIS spectral bands (Jin and Liang 2006), whereas the derivation of ϵ_{plot} from EC flux data provides an independent alternative for the estimation of effective plot-scale ϵ. Our finding that inclusion of an intercept in the H vs ΔT relationship when estimating ϵ_{plot} significantly reduces uncertainty in ϵ_{plot} while increasing uncertainty in ΔT suggests that this method could be used for reliable estimates of effective ϵ_{plot} within the radiometer footprint even in the presence of a footprint mismatch between the radiometric and H measurements. The approach could also be extended to urban settings if reliable EC

measurements are available and anthropogenic heat components are known. Although the effects of footprint mismatch between radiometric and EC measurements could be large in such a heterogeneous setting, ϵ_{plot} estimation based on H vs ΔT with intercept could provide a robust estimate of effective ϵ_{plot}, which is important for climate models simulating urban heat island effects (Chakraborty et al. 2021).

In summary, our results reveal that the short equation (Eq. (2.10), neglecting downwelling longwave radiation) leads to biased estimates of LST and substantially overestimated sensitivity of LST to surface emissivity. Therefore, the use of Eq. (2.10) is not recommended and should be replaced by Eq. (2.6) if downwelling longwave radiation measurements are available. At some sites, the use of Eq. (2.6) resulted in plot-scale LST estimates that were far below satellite-derived landscape-scale LST values, and also inconsistent with plot-scale flux data (negative surface-air temperature difference when sensible heat flux is strongly positive). In many previous studies, such bias would have been removed by slightly lowering surface emissivity (ϵ), but the reduced sensitivity of Eq. (2.6) to ϵ would require unrealistically low values of ϵ to remove the low-bias in LST. When estimating plot-scale ϵ values, realistic estimates based on Eq. (2.6) are only possible at these sites if we include an intercept in the H vs ΔT relationship, but this again results in very high intercept values (over 200 $W\ m^{-2}$). Note that high values of intercept do not necessarily make ϵ_{plot} unreliable, they rather suggest poor correspondence between H and T_s due to footprint mismatch. Hypothesizing that the intercept is a consequence of a foot print mismatch between the aerodynamic and radiometric measurements, a small correction in upwelling longwave (6-9%) and subsequent energy balance closure (based on the Bowen ratio) largely removed the intercept and produced realistic ϵ_{plot} values and self-consistent H vs ΔT plots. This approach also reduced the bias between plot-scale LST and MODIS LST, although it did not improve the weak correlation between these LST estimates (Fig. A.5b). In the past, ground-based radiometric measurements have been used for the validation of the MODIS LST product (Wang, Liang, and Meyers 2008), whereas here we compared the plot-scale LST with MODIS LST to check its dependency.

The combination of radiometric and aerodynamic measurements for the estimation of ϵ_{plot} and LST provides a quality check on the correspondence between observed fluxes and temperatures at ECS. The intercept value can be used as a consistency criterion for observed data (radiometric and aerodynamic measurements) before using them in combination, as a strong intercept indicates inconsistency between observed sensible heat flux and surface-to-air temperature difference. Therefore, the proposed method of fitting a linear relation with intercept to H and ΔT has the potential to provide more reliable benchmark data sets for model evaluation and validation at the ecosystem scale (plot-scale). The ϵ_{plot} estimates could also be used to parameterize climate and weather prediction models at ecosystem scale, but this was not tested in the present study. Overall, the implications of our study are of particular relevance for the research community

interested in process-based understanding of the diurnal and seasonal feedbacks in soil-vegetation systems based on observed fluxes.

2.5 Code and data availability

The data and code used for this study is freely available from zenodo.org (https://doi.org/10.5281/zenodo.6385016)

Chapter 3

Impact of surface heterogeneity on flux tower measurements

An edited version of this paper will be submitted to Biogeosciences as:
Thakur, G., Schymanski, S.J., Trebs, I., "Assessing the effects of surface heterogeneity and footprint mismatch on ecosystem-scale observations using a two source energy balance model"

Contents

3.1 Introduction

Flux tower installed over an ecosystem measures the energy, water, and carbon exchange between the surface and the atmosphere and the environmental variables (e.g., air temperature, wind speed) are recorded at an hourly timescale. The instrumentation at the flux tower sites consists of a radiometer measuring incoming and outgoing solar and infrared radiation from the ecosystem-surface, an Eddy Covariance System (ECS) measuring the turbulent exchange of energy (H) and water fluxes (LE), and heat plate placed beneath the ground (2-20 cm) to measure the ground heat flux (G). R_{net} represents the balance between incoming solar radiation (R_{sdwn}), and the radiation from the sky (R_{ldwn}) and outgoing solar radiation (R_{sref}, R_{lref}, R_{lup}). By idealizing the ecosystem as homogeneous surface and applying the law of energy conservation, the net solar radiation received by the surface (R_{net}) equals the sum of H, LE, and G which is termed as surface energy balance as shown in Eq. (3.1)

$$R_{net} = H + LE + G \tag{3.1}$$

H ($W\ m^{-2}$) is the sensible heat flux; it represents the energy transfer between the land surface and the atmosphere due to convection and conduction. LE ($W\ m^{-2}$) is the latent heat flux; it is the energy removed by the land surface when water evaporates from the surface into the atmosphere (evaporation/transpiration). G ($W\ m^{-2}$) is the ground heat flux; it refers to heat exchange from the Earth's surface into the soil calculated using soil heat conductivity and the vertical gradient of air-temperature (Buchan 2000; Sánchez et al. 2008). EC measurements (H, LE) are averaged over a typically larger area and have a footprint of several hundreds of meters. In contrast, a radiometer measures the incoming and outgoing solar radiation (used to estimate R_{net}) has a footprint of a tenth of a meter (hemispherical footprint). The footprint of the G measuring plate is in meters (Wohlfahrt and Tasser 2015). The footprint represents the spatial extent from which the measured fluxes originate and describes the region over which the fluxes are representative and can be attributed to the measurements taken at a particular site (Schmid 2002). The radiometric footprint is determined by the size of its hemispherical field of view (FOV). In contrast, the EC footprint is determined by the characteristics of the atmospheric turbulence, which typically covers a larger area than the radiometeric footprint (Hoffmann et al. 2016). Thus, any variations in land-cover, canopy structure, soil types, etc., within the radiometer FOV w.r.t the EC footprint can lead to spatial representativeness issues and a mismatch in footprints, which implies the spatial composition representing R_{net} is different from the H and LE (Wohlfahrt, Klumpp, and Soussana 2011). The footprint of an EC system depends on the installation height (Z_m), surface roughness, and atmospheric stability. In contrast, the radiometric footprint depends on

the installation height and the area the radiometr sees (Schmid 1994; Göckede, Rebmann, and Foken 2004). It has been reported that almost 100% of the hemispherical radiometric signal originates from within a diameter of two to five times of radiometer installation heights (installed on a tower, looking vertically up and down), while about 50–80% of the turbulent flux signal is generated within a distance of about twenty times the installation heights (Marcolla and Cescatti 2018). Flux tower observation represents the combined vegetation and ground (soil, dry leaves) surface fluxes, and the observed H is related to the average surface-to-air temperature difference using Eq. (3.2) (Lhomme 1991).

$$H = \frac{\rho C_p}{r_{ah}}(T_s - T_a) \tag{3.2}$$

r_{ah} $(m\ s^{-1})$ is the aerodynamic resistance that the ecosystem-surface provides to the heat exchange, T_a (K) is the average air temperature measured above the surface (at Z_m) and T_s (K) is the average surface temperature of the ecosystem-surface estimated using Eq. (3.3)(Thakur et al. 2022).

$$T_s = \sqrt[4]{\frac{R_{ldwn}}{\sigma} - \frac{R_{ldwn}}{\epsilon\sigma} + \frac{R_{lup}}{\epsilon\sigma}} \tag{3.3}$$

R_{ldwn}, R_{lup} is the observed downwelling and upwelling longwave radiation, and ϵ is the effective emissivity of the ecosystem-surface composed of ground and vegetation. The ecosystem- surface comprise of ground (ϵ_s) and vegetation (ϵ_v). ϵ_s depends mainly on the soil moisture, soil organic matter and ϵ_v depends on the vegetation type, vegetation density, leaf orientations, etc. (Guillevic et al. 2003) (Valayamkunnath et al. 2018). In Chapter 2, we combined observed H with the estimated $T_s - T_a$ using a linear regression model at lux tower sites to estimate the monthly value of ecosystem-scale ϵ (ϵ_{opt}) found that to represent H vs ΔT we need to consider intercept meaning Eq. (3.2) was replaced by Eq. (3.4) (Thakur et al. 2022).

$$H = m(T_s - T_a) + c \tag{3.4}$$

The slope (m) of Eq. (3.4) can be used to estimate canopy-scale total resistance to H as explained in Chapter 4. r_{ah} plays a crucial role in understanding the functional response of climate change to the exchange of H and LE between the Earth's surface and the atmosphere. It provides important insights into how changes in the Earth's surface properties, such as changes in vegetation cover, affect the exchange of energy and water vapor with the atmosphere (Shaver et al. 2000). There exist multitude of semi-empirical parameterisations to estimate r_{ah} using canopy height, shear wind speed (Verma, Kim, and Clement 1989), wind speed (Allen et al. 1998), and atmospheric stability (Thom et al. 1975). $c(W\ m^{-2})$ is the intercept of the regression (between H vs $T_s - T_a$), i.e.,

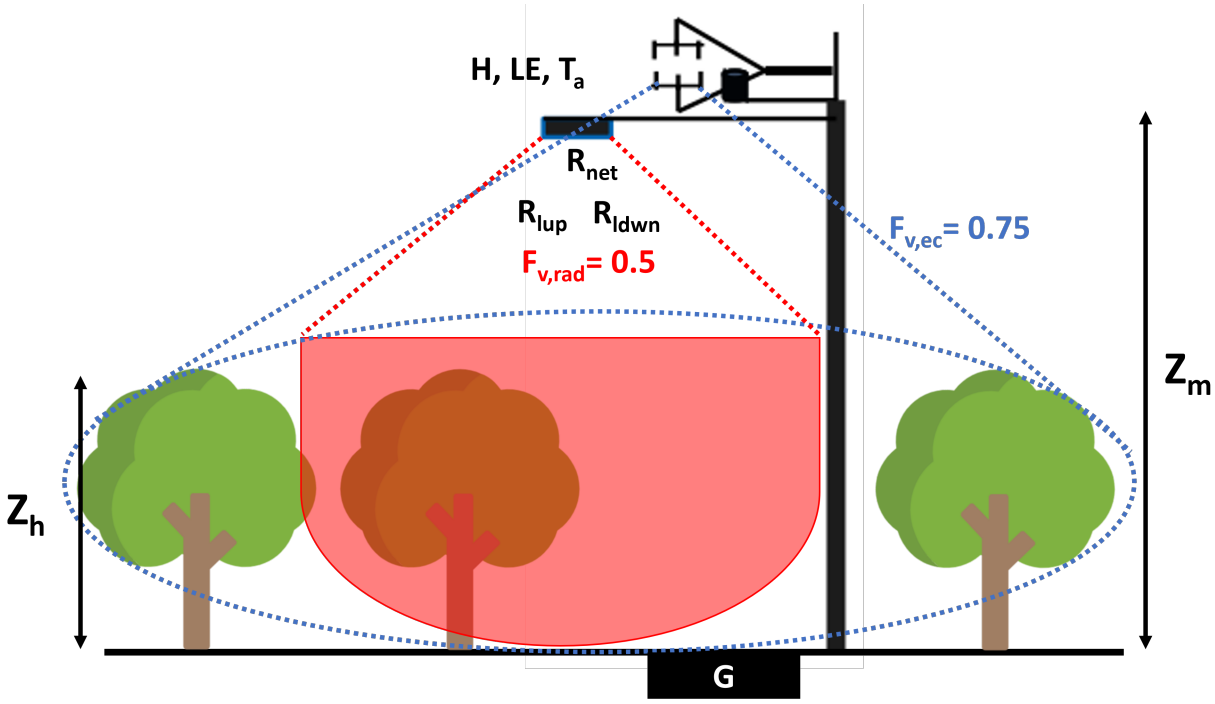

Figure 3.1: Conceptual representation of the footprint mismatch between the EC measurement system and the radiometers. $F_{v,ec}$ is the fractional vegetation cover and contributing to EC measurements and $F_{v,rad}$ is the fractional vegetation seen by the radiometer. The red dotted line shows the radiometeric footprint and the blue dotted line is showing the ECS footprint. Z_m is the height above the ground where radiometers are placed and Z_h is the average canopy height at the study site. It means for a heterogeneous ecosystem, the vegetation fraction seen by the radiometer ($F_{v,rad}$) contributing to R_{net}, R_{lup}, R_{ldwn} can be different than the vegetation fraction ($F_{v,ec}$) contributing to the measurement of turbulent fluxes (H,LE). The heat plate measuring G is shown by black box located within the radiometric footprint

H contribution from the ground or vegetation surface that contributes to the EC measurements but is not accounted by the radiometric measurement (radiometer's FOV). A conceptual representation of small-scale spatial heterogeneity at the flux tower site resulting in c as shown by Eq. (3.4) is shown in Fig. 3.1. Understanding the consequences of spatial surface heterogeneity is crucial to correctly interpret flux tower observations and derive meaningful insights from them. These measurements are also used to validate and calibrate land surface models (LSM)(Chu et al. 2021) and diagnose process representations in surface energy balance models (SEB) models (Butterworth et al. 2021). SEB models evaluate the functional response of land -cover types to energy or water exchange under changing environments by mathematically representing the physical processes such as radiation, convection, conduction, and evaporation. The model parameterizes R_{net} by using downwelling solar radiation, ϵ and surface albedo (α). H is represented using the flux-gradient relationship as shown in Eq. (3.2), r_{ah} is parameterized using semi-empirical formulations and T_s values are obtained by remote sensing measurement (Lhomme 1991) (Su 2002). G is parameterized using the soil heat conduction equation, which describes the transfer of heat through the soil using thermal conductivity, volumetric heat capacity

and, the temperature gradient within the soil layers (Corbari et al. 2010; Su 2002) iterated over time such that Eq. (3.1) is satisfied and most of the time LE is estimated as a residual (Choudhury, Reginato, and Idso 1986a). The model performance is evaluated by comparing steady state estimates of SEB components to the observations of H, LE and G.

A common challenge in comparing modelled SEB component to the measured fluxes is the non-closure of the energy balance (EB) at the flux tower sites, also known as the energy balance closure problem. Energy balance closure, a formulation of the first law of thermodynamics, requires that the sum of the energy fluxes (H, LE and G) should equal the net available energy (R_{net}) for a given surface. However, in practice, the measured turbulent fluxes (H, LE) and soil heat flux (G) often fall short of balancing the available energy (R_{net}), leading to the non-closure of the energy balance equation (Wohlfahrt et al. 2009). Primary method to quantify energy imbalance involves deriving linear regression coefficients, specifically the slope and intercept using ordinary least square (OLS) relationship between the half hourly estimates of the dependent flux variables (H+LE) against independent net available energy (R_{net}-G) (Wilson et al. 2002; Kidston et al. 2010). The slope of the energy balance shows the ratio of incoming (R_{net}) and outgoing energy (H+LE+G) at a flux tower site and in an ideal condition should be one with negligible intercept (Wilson et al. 2002). For most of the time the slope is smaller than one (between 0.7 to 1) meaning the outgoing fluxes are less than the incoming radiation. Numerous studies worldwide indicate that the turbulent fluxes (H, LE) are generally underestimated when the turbulence is low as smaller eddies are unable to reach the eddy-covariance measurement system (Mauder, Foken, and Cuxart 2020) resulting in under estimation of H and LE. Thus, the observed turbulent fluxes (H, LE) are corrected using bowen ratio energy balance closure scheme (Wilson et al. 2002; Kidston et al. 2010) such that Eq. (3.1) is satisfied and the slope of energy balance regression is one. Another reason for the non-closure of energy balance is overestimation of the net available energy (R_{net}) and primary reason for this is the mismatch between the instruments measuring incoming solar energy (R_{net}) and the ECS measuring turbulent fluxes (Wilson et al. 2002; Kidston et al. 2010). Quantifying the component of imbalance due to footprint mismatch using measurements is challenging because the impacts of various factors are combined and represented together in the measurements however, more attention must be given to the energy imbalance resulting from footprint mismatch. In chapter 2 (Thakur et al. 2022), we found that only by considering the footprint mismtach the intercept of H vs ΔT can be explained. Here we investigate in how far a footprint mismatch can indeed cause an intercept in the H vs. $T_s - T_a$ and $H + LE$ vs. $R_n - G$ using a two source energy balance model (TSEB).

1. Is there a relation between slope and intercept of H vs ΔT and the energy imbalance?

2. Can footprint mismatch between radiometer and eddy covariance tower can lead to a positive intercept in H vs ΔT and significant energy imbalance?

3. What is the best approach for achieving a consistent H vs ΔT plot in the presence of footprint mismatch?

3.2 Methods

The flux tower sites where the study was conducted are described in Table. 3.1.

3.2.1 H vs ΔT regression and energy imbalance regression

The half-hourly daytime observations of the flux tower measurement are used, which include sensible heat (H), Latent heat (LE), ground heat flux (G) upwelling longwave (R_{lup}), downwelling longwave (R_{ldwn}), air temperature (T_a), wind speed (U_z) and shear wind speed (U^*) is used. The data filtering criteria was $R_{net} > 25\ Wm^{-2}$, $U_z > 2\ ms^{-1}$, $U^* > 0.2$ (Holmes et al. 2009). For the regression between H and ΔT, we used measured H and T_a, whereas T_s was deduced from observed R_{lup} and R_{ldwn} and prescribed emissivity values, taken either from MODIS, or by fitting to achieve a maximum R^2 between H and ΔT. The ϵ value at which RMSE is minimum and $R^2 > 0.5$ is called as ϵ_{opt}. The robust linear regression between H and $T_s - T_a$ is performed as shown in Eq. (3.5) (Thakur et al. 2022) using a python package scipy. stats.linregress().

$$H = m(T_s - T_a) + c \tag{3.5}$$

The intercept (c) corresponds to the H measured by the EC system when the surface contributing to the radiometer readings has ΔT=0, i.e. H=0. c represents the H from the fraction of vegetation or ground which is not seen by the radiometer but contributes to the H measured by the EC measurement system. We hypothesise that the value of c is positive if the radiometer sees a higher vegetation fraction than that contributing to the EC fluxes. To quantify the strength and direction of the energy imbalance and to interpret how c from Eq. (3.5) relates to the imbalance (c_{imb}, m_{imb}) a linear regression model was applied, as shown in Eq. (3.6)

$$H + LE = m_{imb}(R_{net} - G) + c_{imb} \tag{3.6}$$

The EC measurement system measures H and LE within the same footprint, while the footprint of G is smaller but always contained within the radiometer footprint. The value of m_{imb} in Eq. (3.6) is consistently less than one due to non closure of energy balance at EC sites (Foken 2008). The intercept in Eq. (3.6) (c_{imb}) is the H+LE when

Table 3.1: Description of study sites

Study site	Landcover	Time-period	Measurement height (m)	Altitude (m)	Average leaf width (m)	LAI
Adelaide River **(AR)**	Savanna dominated by Eucalyptus tectifica and Planchonia careya	2007-09	21	90	0.025	1.7
Alice Springs **(AS)**	Mulga woodland, hummock grassland, river red gum forest	2016-18	9.25	606	0.008	0.5
Daly Uncleared **(DU)**	Woodland savanna	2016-18	21	110	0.031	1.5
Gebesee **(GB)**	Cropland	2017-20	3.5	153	0.032	1.4
Howard Springs **(HS)**	Open woodland savanna	2016-18	23	63	0.05	1.3
Litchfield **(LF)**	Tropical savanna	2016-18	23	222	0.05	1.5
Sturt Plains **(SP)**	Mitchell Grass	2016-18	5	230	0.004	0.49
Tharandt **(TH)**	72% spruce and 13% deciduous forest (10% larch)	2017-20	42	214	0.002	4.5
Ti Tree East **(TT)**	Grassy mulga woodland, Corymbia/ Triodia savanna	2016-18	6.25	553	0.008	0.3
Tumbarumba **(TUM)**	Wet sclerophyll	2015-17	40	1200	0.034	4.17
Yatir Forest **(YF)**	Evergreen need-leaf forest	2005	12	641	0.002	1.3

$R_{net} - G = 0$. Considering that $R_{net} - G$ is measured by the radiometric instruments and ground heat flux plates, representing the radiometer footprint, whereas H and LE stems from the EC footprint, an non-zero intercept can indicate a footprint mismatch between these measurements. Intecept c in Eq. (3.5) corresponds to the H measured by the ECS when ΔT=0, meaning no measurements by radiometer. To determine if there is a consistent pattern between the intercepts in Eq. (3.6) and Eq. (3.5), both of which could indicate a footprint mismatch between the radiometric and turbulent flux measurements, we calculated the regressions for individual months at different study sites.

$$R_{net} = R_{sdwn} + R_{ldwn} - R_{sref} - R_{lref} - R_{lem} \tag{3.7}$$

3.2.2 Numerical two-source model

A physically based two-source energy balance model (TSEB) was formulated to test the footprint mismatch hypothesis. This model was derived from the leaf model developed by Schymanski et al. (Schymanski, Or, and Zwieniecki 2013), with equations and coefficients adapted for a vegetation canopy and the ground surface (soil or dried leaves). Meteorological data from an EC station were used as input and the surface energy balance equation was solved. The model estimates steady-state sensible heat flux (H), latent heat flux (LE), and longwave radiation flux (R_{lup}) from both ground and vegetation surfaces. These simulated fluxes are then combined to simulate the footprint mismatch between the radiometer and the eddy covariance system within the two-source energy balance framework as explained below.

Vegetation surface energy balance model

The absorbed shortwave solar radiation is partitioned by the vegetation into sensible heat flux by the vegetation (H_{veg}), latent heat flux by the vegetation (LE_{veg}), and the upwelling longwave from the vegetation surface ($R_{lup,veg}$) as shown in Eq. (3.8).

$$R_{sdwn} + R_{ldwn} - R_{sref} - R_{lref} = H_{veg} + LE_{veg} + R_{lem} \tag{3.8}$$

R_{sdwn} is the observed downwelling shortwave radiation, R_{sref} is the reflected shortwave radiation, R_{lref} is the reflected longwave radiation, R_{lem} is the emitted longwave radiation. H_{veg} is parameterized using vegetation temperature (T_{veg}), observed air temperature (T_a) (K) and aerodynamic resistance ($r_{ah,veg}$) offered by the vegetation surface as shown in Eq. (3.9).

$$H_{veg} = \frac{\rho C_p}{r_{ah,veg}}(T_{veg} - T_a) \tag{3.9}$$

Here, C_p ($J\ kg^{-1}\ K^{-1}$) is the specific heat capacity of the air, ρ ($kg\ m^{-3}$) is the air density.$r_{ah,veg}$ is parameterized using formulation by Allen et al. (Allen et al. 1998) as

shown in Eq. (3.10)

$$r_{ah,veg} = \frac{\log\left(\frac{Z_h - d}{Z_{oh}}\right)\log\left(\frac{Z_m - d}{Z_{om}}\right)}{k^2 U_z} \tag{3.10}$$

Z_m is the measurement height, Z_h is the canopy height, d is the displacement height, Z_{om} is the roughness length for momentum exchange, Z_{oh} is the roughness length of heat exchange, estimated using the rule of thumb $d = 0.67Z_h$, $Z_{om} = 0.123Z_h$, $Z_{oh} = 0.1Z_{om}$ (Thom et al. 1975). The exchange of LE was parameterized as a function of the concentration of water vapor inside the leaf ($c_{w,veg}$, $mol\ m^{-3}$) and in the free air (c_{wa}, $mol\ m^{-3}$) as shown in Eq. (3.11).

$$LE_{veg} = \frac{\rho C_p}{r_{cw,veg}}(c_{w,veg} - c_{wa}) \tag{3.11}$$

$c_{w,veg}$ is a function of T_{veg} as shown in Eq. (3.12), $r_{cw,veg}$ is the effective resistance of the vegetation to the exchange of water.

$$c_{w,veg} = \frac{P_{wl}}{R_{mol} T_{veg}} \tag{3.12}$$

P_{wl} is the saturation vapour pressure at the leaf temperature (Schymanski, Or, and Zwieniecki 2013).The vegetation resistance to the exchange of water ($r_{cw,veg}$) is defined as the sum of $r_{ah,veg}$ and stomatal resistance (r_s). For simplicity, r_s was assumed to be constant, at 100 $m\ s^{-1}$, which is the standard resistance for a single leaf proposed for a grass reference crop by Allen et al. (1998) (Allen et al. 1998). The stomatal resistance for the canopy (r_{sc}) was calculated by dividing the stomatal resistance of a single leaf (r_s) by leaf area index (LAI).

$$r_{cw,veg} = r_{ah,veg} + r_{sc} \tag{3.13}$$

$$r_{cw,veg} = \frac{\log\left(\frac{Z_h - d}{Z_{oh}}\right)\log\left(\frac{Z_m - d}{Z_{om}}\right)}{k^2 U_z} + r_{sc} \tag{3.14}$$

$R_{lup,veg}$ is calculated using Eq. (3.15), the ϵ_v was prescribed as 0.97 and observed R_{ldwn} value was given as input

$$R_{lup,veg} = R_{ldwn} F_{v,rad}\,(+1 - \epsilon_v) + \epsilon_v F_{v,rad} \sigma T_{veg}^4 \tag{3.15}$$

As shown in Eq. Eq. (3.15), R_{ldwn} is the downwelling longwave observed by the radiometer. The observed meteorological variables used as input are U_z, T_a. Canopy structural properties (a_s, $a_s h$, L_l, Z_h, LAI), the stomatal resistance (r_s) are given as an input to calculate the steady state energy balance (Eq. 3.8) for each observed input in time we get T_{veg}, H_{veg},E_{veg},$R_{lup,veg}$

Ground surface energy balance model

The ground-surface energy balance model is represented in Eq. (3.16), the absorbed shortwave solar radiation ($R_{sdwn} - R_{sref}$) is partitioned into H_{gr}, LE_{gr}, R_{gr} and G.

$$R_{sdwn} + R_{ldwn} - R_{sref} - R_{lref} = H_{gr} + LE_{gr} + R_{lem,gr} + G \tag{3.16}$$

For the ease of modelling, we considered $G = 0$. Ground surface heat flux (H_{gr}), is simulated similar to that for vegetation (Eq. 3.10), but using the ground surface temperature (T_{gr}) and ground resistance to sensible heat flux (r_{gr}) as shown in Eq. (3.17):

$$H_{gr} = \frac{\rho C_p}{r_{gr}}(T_{gr} - T_a) \tag{3.17}$$

r_{gr} is parameterized using wind speed, air temperature at a height two meters above the ground surface, $T_{a,2m}$, and T_{soil} is the ground temperature measured by the soil sensor at eddy-covaiance sites (Kustas et al. 2016).

$$r_{gr} = \frac{1}{c\left(T_{gr} - T_{a,2m}\right)^{0.33} + bU_2} \tag{3.18}$$

$T_{a,2m}$, $U_{z,2m}$ is the air temperature and wind speed at two meters above the soil surface, and Eq. (3.18) was substituted in Eq. (3.17) to estimate H_{gr}. For simplicity, we assumed the evaporation from ground to be zero ($E_{gr} = 0$). The $R_{lup,gr}$ is defined as a function of T_{gr}, emissivity of the ground surface (ϵ_s) and observed R_{ldwn}. The prescribed value of ϵ_s was 0.93.

$$R_{lup,gr} = R_{ldwn}\left(1 - \epsilon_s\right) + \epsilon_s \sigma T_{gr}^4 \tag{3.19}$$

Eq. (3.17) are substituted in Eq. (3.16) and the energy balance equation is solved until steady state is reached and for each observed input in time we get T_{gr}, H_{gr},$R_{lup,gr}$as shown in Eq. (3.16).

Combining ground and vegetation: Two-source model accounting for footprint mismatch

The vegetation and ground energy balance model is combined to represent the footprint mismatch and their respective contribution to the eddy covariance and radiometric footprints. Given that the radiometer has a much smaller footprint than the eddy covariance tower, there is a possibility that the fraction of vegetation in the radiometer footprint ($F_{v,rad}$) is different to that in the footprint of the eddy-covariance tower ($F_{v,ec}$) Considering the one-dimensional description of energy partitioning for sparse canopy assuming horizontal uniformity (Shuttleworth and Wallace 1985), the total sensible heat flux is represented as the sum of sensible heat fluxes from the ground and vegetation, scaled by

the vegetated fraction in the EC footprint (Eq. 3.20):

$$H_{tot} = F_{v,ec}H_{veg} + (1 - F_{v,ec})H_{gr} \tag{3.20}$$

Similarly, the total upwellling longwave radiation is computed as the sum of contributions by the vegetation and the ground, scaled by the vegetated fraction seen by the radiometer (Eq. 3.21):

$$R_{lup,tot} = F_{v,rad}R_{lup,veg} + (1 - F_{v,rad})R_{lup,gr} \tag{3.21}$$

$R_{lup,tot}$, R_{lin} are used to estimate the average temperature of the ground-vegetation composite surface ($T_{s,avg}$), the ϵ range was defined between (0.998 to 0.7) such that the RMSE between H_{tot} and $T_{s,avg} - T_a$ regression was minimum. Average temperature of the ground and vegetation surface ($T_{s,avg}$) using the $R_{lup,tot}$ was estimated Eq. 3.22

$$T_{s,avg} = \sqrt[4]{\frac{R_{ldwn}}{\sigma} - \frac{R_{ldwn}}{\epsilon\sigma} + \frac{R_{lup,tot}}{\epsilon\sigma}} \tag{3.22}$$

3.3 Results

The details of the method can be found in (Thakur et al. 2022). The energy imbalance (ΔE) of each data point was estimated using Eq. (3.23).

$$\Delta E = R_{sdwn} - R_{sref} - (H_{tot} + LE_{tot} + R_{lup,tot}) \tag{3.23}$$

3.3.1 Intercept between H vs. ΔT and Energy balance closure (EBC) using observation

To investigate the correspondence between the intercept (c) of the H vs $T_s - T_a$ regression and energy imbalance,the intercept (c_{imb}) and slope (m_{imb}) of the H+LE vs. $R_n - G$ regression (Eq. (??)) is plotted. In Fig. 3.2a produces a high intercept value for H vs. DT, such that DT is negative throughout the dataset, using an optimized emissivity (ϵ_{opt}) of 0.948. The energy balance regression plot (3.2 at Litchfield (LF). In Fig. 3.2a, a high intercept value for H with a negative surface temperature difference and an optimized emissivity (ϵ_{opt}) of 0.948 is observed. In Fig. 3.2b shows the energy balance regression plot with $m_{imb} = 0.715$ and $c_{imb} = 29\ Wm^{-2}$, which is 3% of H+LE. These analyses were extended to all study sites, and the monthly values of the two intercepts (c_{imb} and c) were estimated over three years at each site, as illustrated in the box plot in Fig. 3.2c. At the TUM, AR, DU, YF, and SP, the box plots shows that the intercept of the energy balance regression (black boxes) is generally higher than that of the H vs. $T_s - T_a$ regression (blue boxes). The median value of c_{imb} across different sites ranged from -1.33 to 68.87 Wm^{-2}, while c varied from -22 to 285 Wm^{-2}. In Fig. 3.2c shows no clear correspondence

between the median values of c (blue dotted lines) and c_{imb} (black dotted lines). The slope of the energy balance closure (m_{imb}) from Equation ?? and the intercept in H vs. ΔT is also plotted as shown in Fig. 3.2d, with no discernible pattern emerging. For most sites, the slope (m) was greater than 0.7, as shown in Fig. 3.2d. The average m_{imb} was highest for the AR site at approximately 0.85 (black box in Fig. 3.2d), with a relatively small c value (blue box in Fig. 3.2d).

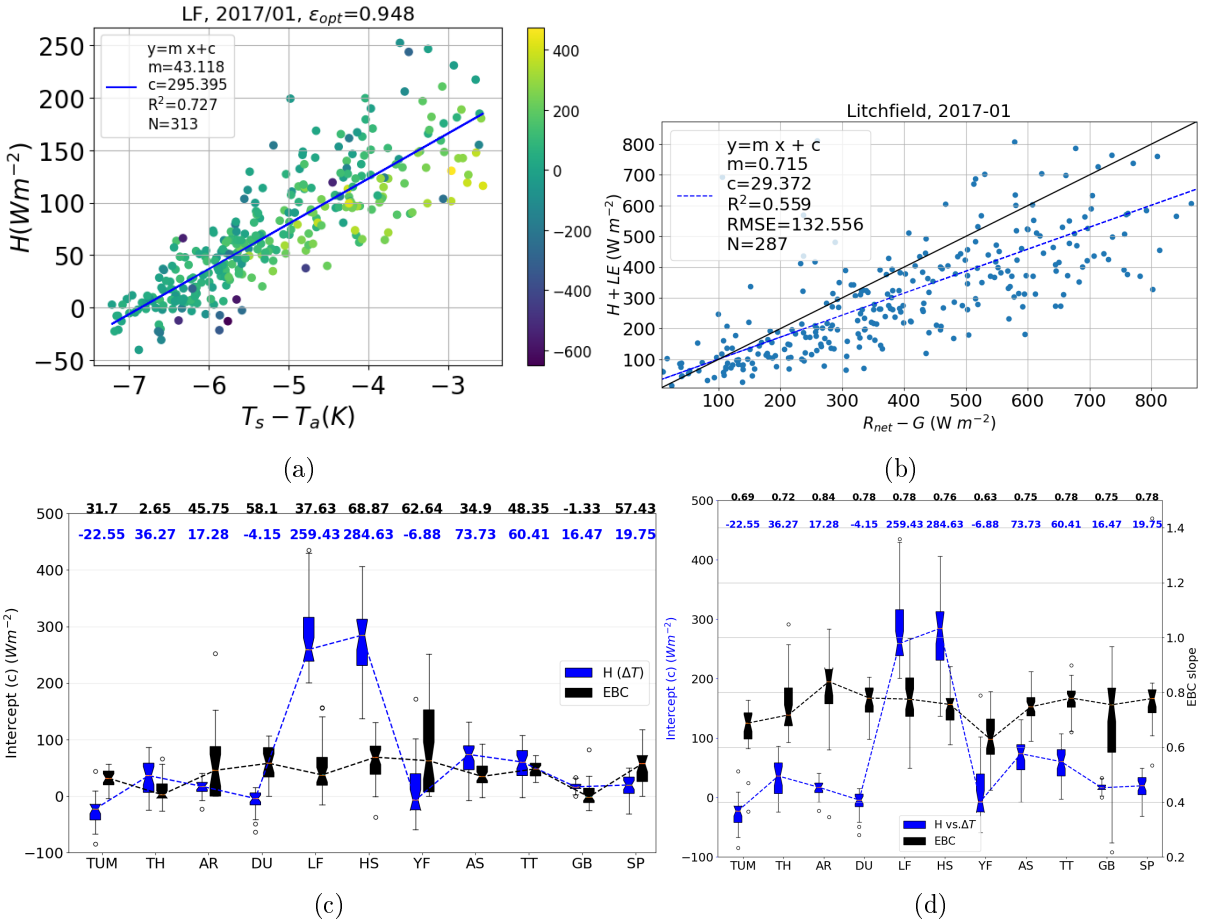

Figure 3.2: Intercept plot (a) monthly linear regression for observed H and ΔT estimated using ϵ_{opt} as given in the plot title along with the year and month;(b) monthly linear regression for observed H+LE and $R_{net} - G$ the year and month is shown in the title of the figure; (c) box-plot showing monthly c (Eq.3.5), c_{imb} (Eq.3.6) obtained using a linear regression as shown in Fig. 3.2a,b is calculated for three years of data across the study sites (d) box-plot shown monthly c and m_{imb} as shown in Eq. (3.6) for three years of data across the study sites

3.3.2 Simulation of footprint mismatch using TSEB model

In this section, we are presenting the result for one site (AS) where the C and C_{imb} values are similar Fig. 3.2a presents an exemplary plot for one month at the AS, showing the relationship between measured sensible heat flux (H) and the estimated temperature difference ($T_s - T_a$), where T_s is calculated using the optimum emissivity and observed energy balance regression is shown in Fig. B.1. TSEB model was applied and the result simulating foot-print mismatch between the radiometer ($F_{v,rad}$) and the eddy covariance

tower ($F_{v,ec}$) in shown in Fig. 3.3 b,c,d. Fluxes were simulated under two conditions, (a) no footprint mismatch, meaning that both the radiometer and the EC system see the same vegetated fractions ($F_{v,rad} = F_{v,ec}$), Fig.3.3b), and (b) maximum mismatch the radiometer sees only vegetation ($F_{v,rad}$=1), while the EC footprint contains only 50% vegetation ($F_{v,ec} = 0.5$). In case of no mismatch, a negative intercept is seen with a magnitude equal to 10% of maximum H (H_{tot}), whereas, for maximum mismatch, the value of c is almost 50% of the maximun H, indicating the impact of footprint mismatch. In Fig. 3.3d, an attempt was made to reduce the intercept resulting from the maximum mismatch simulation by optimising emissivity. The intercept value reduced from from 231 to 104 $W\ m^{-2}$ for an emissivity value of 0.79. This adjustment improved the R^2 and RMSE without significantly altering the slope, as shown by comparing Fig. 3.3b and 3.3c.

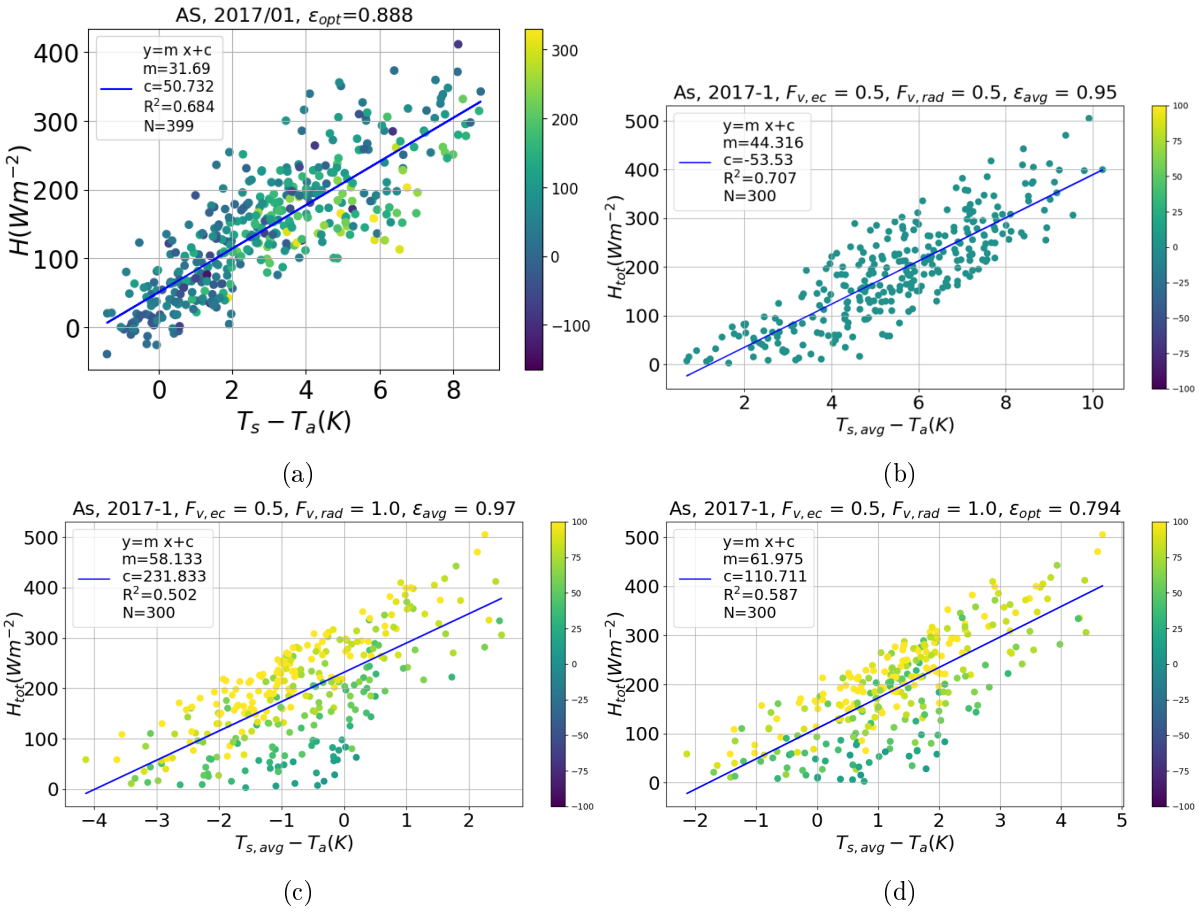

Figure 3.3: Comparison of H vs. ΔT plot using observed values and the TSEB model for 2017/01 at AS. (a) Observed values of H, where T_a is used and T_s is estimated using observed R_{lup} and ϵ_{opt} (the value is shown in the plot title); (b) Simulated H vs. ΔT assuming no mismatch ($F_{v,rad} = F_{v,ec}$); (c) Simulated H vs. ΔT for maximum mismatch ($F_{v,ec} = 0.5$, $F_{v,rad} = 1$) using average emissivity; and (d) Simulated H vs. ΔT for maximum mismatch using optimized emissivity ($\epsilon_{opt} = 0.794$). For all simulations, $F_{v,ec} = 0.5$, where H_{tot} refers to the sum of H_{veg} + H_{gr}, while $T_{s,avg}$ was calculated based on the sum of simulated upwelling longwave radiation from the vegetation and the ground hypothetically detected by the radiometer based on $F_{v,rad}$. The color bar represents the energy imbalance of each data point.

3.3.3 TSEB: correcting consequence of footprint mismatch by correcting R_{lup}

To correct the intercept in H vs. ΔT resulting from maximum mismatch, a correction was applied to upwelling longwave flux (R_{lup}) and it was found that by applying a 10% correction to R_{lup}, the intercept reduced from 231 to 2.34 $W\ m^{-2}$ (99% reduction in intercept),correction in R_{lup} reduces the slope by 22% and R^2 by 2.1% (Fig. 3.4a) in comparison to Fig. 3.3c. The slope of energy imbalance improved from 0.842 (Energy imbalance regression for Fig. 3.3c (shown in SI) to 0.87, as shown in the Fig. 3.4b.

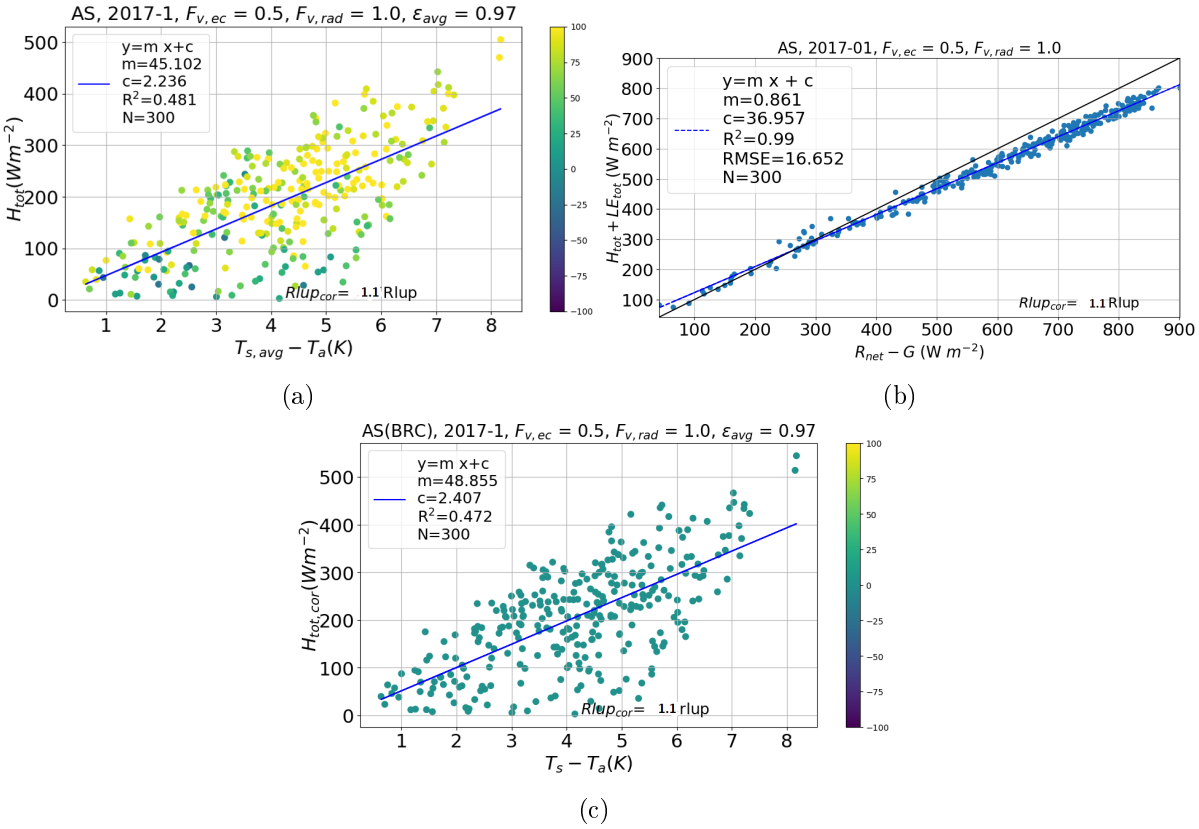

Figure 3.4: Comparison of H vs. $T_s - T_a$ plot using observed values and TSEB model for 2017/01 at AS (a) observed value of H, T_a is used and T_s is estimated using observed R_{lup} and ϵ_{opt} the value is shown in the plot title; (b) H in the y-axis is the H_{tot} simulated from the TSEB model, T_a is the observed air temperature and T_s is estimated using $R_{lout,tot}$ and ϵ_{opt} for no mismatch condition ($F_{v,ec} = F_{v,rad}$); (c) reproduction of (b) and the Bowen ratio closure has been applied.

3.3.4 Comparison of average surface (ground and vegetation) temperatures using TSEB

In the previous section, it was demonstrated that correcting R_{lup}, rather than optimizing emissivity, is a more effective method for removing the positive intercept caused by footprint mismatch. Here we investigate which approach (optimizing emissivity or R_{lup} correction) is best to improve the effects of footprint mismatch for representing realistic surface to air temperature difference. The average surface temperature of the

vegetation-ground surface ($T_{s,v}$) with the compared with the $T_{s,avg}$, estimated using the model-simulated $R_{lup,tot}$ and ϵ_{avg}. As shown in Fig. 3.5a the R^2 is low between the average temperature (TSEB) of the surface and the radiative temperature (TSEB) . The R^2 improves slightly in Fig. 3.5b by optimising emissivity (ϵ_{opt}) and by correcting R_{lup} by 55% as shown in Fig. 3.5c, R^2 increases to 0.25 and this also improves the energy balance closure, as detailed in the supplementary information (see Fig. SI).These results underscore the importance of addressing footprint mismatch through R_{lup} correction rather than emissivity optimization, thereby ensuring more accurate surface temperature estimations and better energy balance closure.

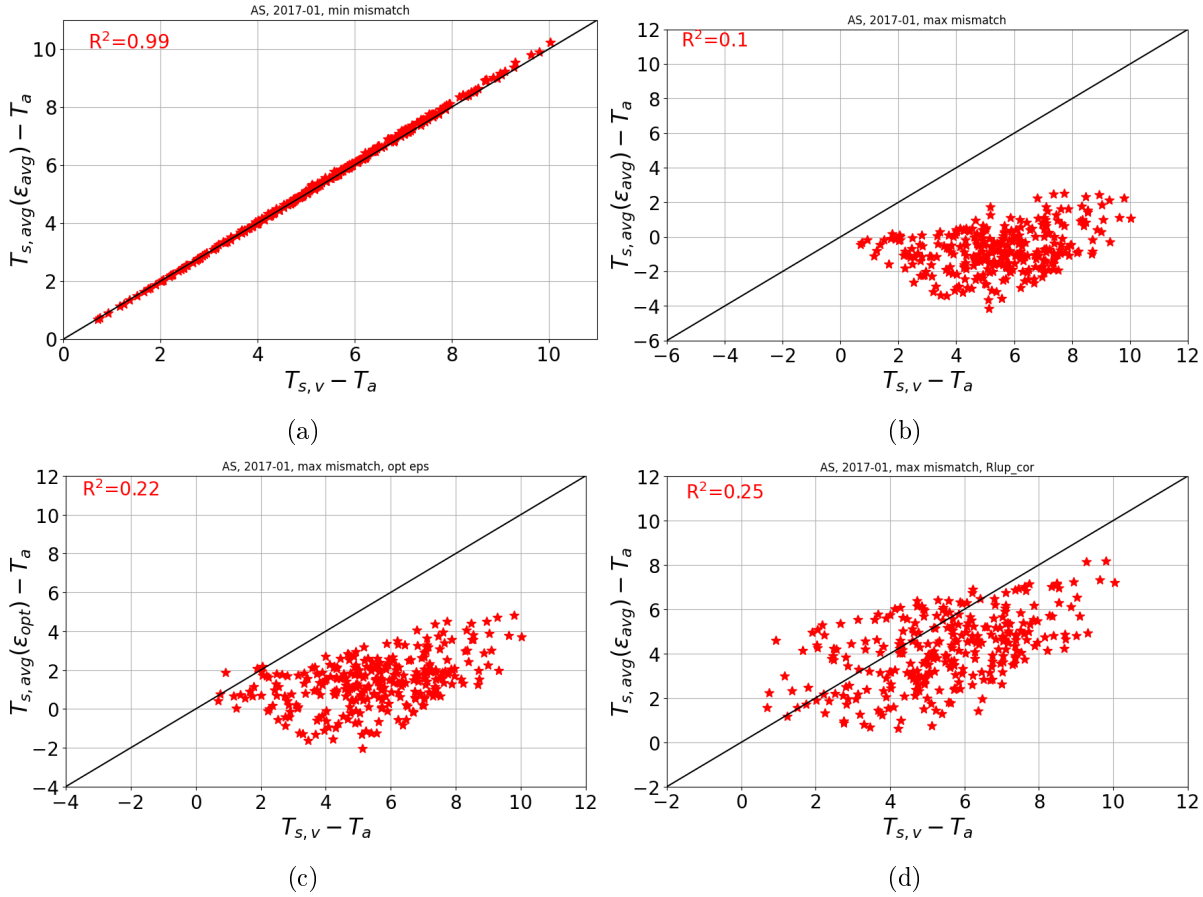

Figure 3.5: Comparison of ecosystem-scale surface-to-air temperature difference estimated using different TSEB model for 2017/01 at AS,$T_{s,v}$ is obtained by averaging the soil and vegetation temperature obtained using the two source model $(T_{soil}(1 - F_{v,rad}) + T_{veg}(F_{v,rad})$ and $T_{s,avg}$ is obtained using ϵ values and $R_{lup,tot}$as shown in Eq. (3.22) (a)using $\epsilon_{avg} = 0.95$ for mimimum-mismatch (b)using $\epsilon_{avg} = 0.97$ for max-mismatch (c) using $\epsilon_{opt} = 0.786$ for max-mismatch, (b) using $\epsilon_{avg} = 0.97$ for max-mismatch and correcting R_{lup} by 10% of of its value which lead to minimum +ve intercept in Fig. 3.4a.

3.4 Discussion

The analysis of the monthly intercepts of the H vs. ΔT plot across the study sites, in conjunction with the energy imbalance slope and intercept, reveals no consistent pattern.

The high positive intercept values observed at HS and LF suggest the radiometer underestimates the upwelling longwave radiation (R_{lup}) at these sites. This could be the case if the radiometer predominantly captures the cooler vegetation surface, while the eddy covariance tower's footprint observes the warmer ground surface. To investigate this scenario in the field, the TSEB model was employed to simulate conditions where the radiometer views only vegetation ($F_{v,rad} = 1$), resulting in R_{lup} contributions primarily from the vegetation. Conversely, with 50% vegetation present within the ECS footprint ($F_{v,ec} = 0.5$), H from TSEB combines 50% vegetation and 50% soil. This simulation resulted in an intercept value of approximately 50% of the maximum H measured by TSEB, indicating clearly that when the radiometer sees more vegetation than the EC tower, a positive value of intercept is seen. The H vs ΔT intercept value for one year of measurement (2017) is shown in SI, emphasizing the importance of acknowledging footprint mismatch before combining the radiometric and aerodynamic measurement.

The intercept value decreases when optimizing emissivity; however, the optimized emissivity is significantly lower (0.786) than the emissivity used (0.97) for parameterizing the vegetation surface in TSEB. This discrepancy indicates that optimizing emissivity alone cannot accurately retrieve the accurate surface emissivity, showing its ineffectiveness in obtaining a consistent H vs ΔT relationship in cases of footprint mismatch. The model simulation also indicates that footprint mismatch results in an energy imbalance, evidenced by a slope smaller than one and a positive intercept value in the energy balance ($H_{tot} + LE_{tot} = R_{net} - G$) regression. To achieve a consistent H vs ΔT plot by removing the intercept resulting from the footprint mismatch, an absolute correction in R_{lup}, was applied in Chapter 2 (Thakur et al. 2022). In this chapter we found that applying a relative correction in R_{lup} reduced the intercept close to zero for H vs ΔT and improved the slope (m_{imb}) of the energy imbalance curve by 2.5%, though the intercept increased by 1.6%. We also saw that for maximum footprint mismatch we got an energy imbalance of 16% in TSEB (m of energy balance changes from 1 for no mismatch to 0.84 for maximum mismatch) and approximately 10% correction in R_{lup} partially corrected the resulting energy imbalance, improving the slope by 2.5% and increasing the intercept from 2.4% to 4%. To get a clear picture about the impact of R_{lup} correction on energy imbalance, the average imbalance was estimated for the whole month and it was found that with correction the average imbalance decreases from 72 to 47 Wm^2. Relative correction in R_{lup} also improved the correspondance between the temperature of the soil-vegetation surface with the $R_{lup,tot}$ derived temperature (compare Fig. 3.5c,d).

Surface heterogeneity has been recognized as a potential cause for the lack of energy balance closure (Wohlfahrt, Klumpp, and Soussana 2011) and it has been suggested that a footprint mismatch could result in a positive intercept of H vs ΔT(Thakur et al. 2022). Quantifying the impact of surface heterogeneity using measurements is challenging due to the complex interactions between spatial heterogeneity and other processes (e.g.,

advection, atmospheric stability) (Masseroni, Corbari, and Mancini 2014). The role of radiometric measurements in energy imbalance is not explored most of the time and energy imbalance is mostly associated with the underestimation of H and LE (eddies not reaching ECS) and therefore, Bowen ratio closure is applied, which corrects H and LE to close the resulting energy imbalance. One study by Kidston et.al (Kidston et al. 2010) discusses the overestimation of net radiation (R_{lup} underestimation can be one reason) due to systematic heterogeneity between radiometric measurements and the eddy covariance measurements footprint. In this study the mismatch in footprint was caused by the inclusion of the tower with low emissivity material (e.g., aluminium) resulting in overestimation of R_{net} measurements at a pine forest. Using TSEB simulations, our work shows that footprint mismatch creates a bias in the R_{lup} representation (so bias in R_{lup}), resulting in an inconsistent H vs ΔT relationship. In the literature, an intercept in energy balance was supposed to be related to systematic errors due to the different source location of R_{net} vs H and LE (Wilson et al. 2002),(Kidston et al. 2010) and it does not give a clear picture of the result of footprint mismatch on energy balance closure.

Energy imbalance persists at real sites across all seasons and hours. The regression slope is typically closer to one during the warm season due to enhanced exchange. A strong correlation is found between the closure and friction velocity (U^*), atmospheric stability, and time of day (Barr et al. 2006). The solar angle changes throughout the day, thus affecting the radiometric footprint and the correspondence between the aerodynamic and radiometric footprints depending on the site characteristics, instrumentation, and tower geometry (Kidston et al. 2010). The presence of a positive intercept in the H vs ΔT plot could indicate footprint mismatch between the radiometric and aerodynamic footprints (Thakur et al. 2022) however, sensor calibration issues leading leading to an underestimation. Minimizing intercept by correcting for R_{lup} accounts for the bias due to footprint mismatch.However, this correction only slightly improves the energy imbalance. Therefore, applying the Bowen ratio closure in addition to the R_{lup} correction is necessary to achieve a closed energy balance.

3.5 Conclusions

When plot-scale emissivity estimation by combining radiometric and aerodynamic measurements fails due to a footprint mismatch between the radiometer and the eddy covariance tower, compensating for the bias in reflected longwave radiation (R_{lup}) can help correcting retrievals of aurface temperature. In such cases, the Bowen ratio closure method, combined with a three-step process we propose, is practical and effective:

1. In the absence of plot-scale emissivity data for flux-tower sites, use MODIS emissivity (ϵ_{MOD}) to generate H vs. ΔT plots.

2. In presence of a positive intercept in the H vs ΔT plot, correct the upwelling longwave radiation (R_{lup}) by applying a relative percentage adjustment to eliminate intercept (close to zero).

3. Once the footprint mismatch is resolved and we have consistent H vs ΔT plots , apply the Bowen ratio closure method to close the energy imbalance (due to H and LE underestimation).

By following the proposed three-step process, a consistent H vs ΔT plot is obtained with closed energy imbalance. These results can then be used to validate fluxes from land-surface models, potentially giving a fresh perspective to understand and interpret the flux tower measurements. The proposed methodology represents a novel approach to testing the hypothesis regarding the impact of footprint mismatch on H vs ΔT plots and energy imbalance. It offers a practical solution for correcting footprint mismatch leading to bias in surface temperature which additionally improves the energy balance closure. By adopting this procedure, researchers can enhance the consistency of results by accurately combining fluxes. This represents a significant step forward in understanding the consequences of footprint mismatch and correcting fluxes to accommodate this discrepancy.

3.6 Code and data availability

The data and code used for this study is freely available from zenodo.org (https://zenodo.org/records/8015542)

Chapter 4

Ecosystem resistance to energy & water exchange: quantification & prediction

An edited version of this paper will be submitted to Biogeosciences as:
Thakur, G., Schymanski, S.J., Mallick, K. et al. "Bridging the gap between the leaf surface and the canopy air space: Leaf size matters for heat transfer resistance at canopy-scale".

Contents

4.1 Introduction

Vegetation-atmosphere energy exchange originates predominantly at the leaf-surface where the net available solar energy (R_{net}) is partitioned into sensible (H) and latent heat (LE) flux. Here we refer to this energy partitioning as the surface energy balance (SEB). In analogy to Ohm's law (Boulet et al. 1999), SEB components can be expressed mathematically using a flux gradient relationship. Leaf-scale H is driven by the leaf-to-air temperature difference and is controlled by the leaf boundary layer resistance to heat exchange (r_{lh}), which can be parameterized using a flat-plate analogy (for heat exchange) by combining leaf width (L_l) with wind speed (U_z) and other atmospheric properties (Schuepp 1993; Schymanski and Or 2017; Incropera et al. 1996). Similarly, transpiration, which drives the LE flux, is driven by the leaf-to-air water vapor gradient and is controlled by stomatal resistance (biological control) and r_{lh} (McNaughton and Jarvis 1983). The evaluation of leaf-scale exchanges is important at the ecosystem-scale (canopy-scale) for both meteorological forecasting of the atmospheric boundary layer (Raupach and Finnigan 1995; Mauder, Foken, and Cuxart 2020) and water resource management (computation of evapo-transpiration). The most common approaches to compute evapo-transpiration at the canopy-scale are based on the Penman-Monteith equation (PM) (Monteith 1965), which combines the SEB with the flux gradient approach. Schymanski and Or showed that the PM equation does not work at the leaf-scale (Schymanski and Or 2017). However, the model is used widely at the canopy-scale by introducing simplifications such as R_{net} dependency on the surface temperature (T_s) (Liu et al. 2020; Mallick et al. 2013).

Commonly, the surface is hereby represented by a 'big-leaf' with appropriate properties, where a canopy resistance, the equivalent to stomatal resistance at the leaf-scale, is added to the aerodynamic resistance to water vapor transfer (Sprintsin et al. 2012; Cuxart and Boone 2020; Bonan et al. 2021). Enormous attention has been devoted to parametrizing stomatal resistance, which is particularly important when aerodynamic resistance is low (Raupach and Finnigan 1988). Estimates of stomatal resistance used for parametrization are commonly obtained by inverting the PM equation using measured evapo-transpiration and presumably known aerodynamic resistance (Raupach and Finnigan 1988; Maes et al. 2019). Therefore, errors in quantifying aerodynamic resistance will propagate into errors in estimated stomatal resistance and associated parameterizations. As opposed to stomatal resistance, which affects water vapor exchange but not the exchange of sensible heat (Schymanski and Or 2017), the aerodynamic resistance to water vapor exchange is directly coupled with the resistance to sensible heat (Trebs et al. 2021b). This enables direct estimation of aerodynamic resistance from observed sensible heat flux and surface-air temperature differences.

The measurements of ecosystem-scale exchange by the eddy covariance (EC) towers in the surface layer give us a unique opportunity to extensively investigate water and energy exchange controls and their parameterization using first principles (flux gradient relationship). In the current work, we primarily focus on canopy-atmosphere heat exchange and the convective component of the canopy-scale resistance.The fluxes observed by the EC tower in the surface layer correspond to the surface value (Baldocchi, Law, and Anthoni 2000). The observed energy flux (H) is commonly expressed as a function of canopy surface-to-air temperature difference and heat exchange resistance (r_{ah}) as in Eq. (4.1).

$$H = \frac{\rho C_p}{r_{ah}}(T_s - T_a) \tag{4.1}$$

Here, C_p ($J\ kg^{-1}\ K^{-1}$) is the specific heat capacity of the air, ρ ($kg\ m^{-3}$) is the air density, T_a (K) is the temperature of the air measured at a reference height above the surface, T_s (K) is the surface temperature of the vegetation canopy obtained using MODIS (Abdelghani et al. 2008) or by inverting tower-observed longwave radiation (Thakur et al. 2022) and, r_{ah} ($m\ s^{-1}$) is the canopy-scale effective resistance to the heat exchange. Commonly, r_{ah} is estimated as a function of observed shear velocity (U_*), horizontal wind speed (U_z), and the roughness lengths obtained using a roughness length parameterization (RLP) (Cowan 1968; Lettau 1969; Voogt and Oke 1997; Mahrt 1996). The RLP is used to characterize the drag or resistance to airflow caused by the roughness of the surface over which the wind is moving and was initially established for the exchange of momentum. The bulk formulation for resistance to momentum exchange between surface and atmosphere is derived using the eddy diffusivity theory. Eddy diffusivity is a measure of how effectively turbulent eddies can transport heat (K_h) or momentum (K_m) in the air column. The theory's mathematical form represents the momentum exchange rate as a product of K_m and the vertical gradient of the wind speed. Following the logarithmic wind profile above a surface, the wind speed at any reference height Z is parameterized using U^* and roughness length of momentum (Z_{om}). The logarithmic boundary layer over a surface with uniformly distributed roughness height,Z_h, is displaced by 60-70% of Z_h. This height is called displacement height (d), and the modified roughness length is $Z_{om} + d$. The bulk formulation for momentum resistance is estimated by integrating the resistivity profile (r_{az}) between $d + Z_{om}$ and the measurement height Z_m as shown in Fig. 4.1. The resistivity to momentum exchange (r_{az}) is the reciprocal of K_m estimated using U^* and d (Cowan 1968).

The eddy diffusivity theory is extended for the heat exchange by assuming similarity between resistivity for momentum and heat exchange (K_m=K_h) under neutral conditions, and H is represented as a function of the air temperature gradient and r_{az} is as in Eq. (4.2).

$$H = \frac{\rho C_p}{r_{az}(Z)}(-\frac{\partial T}{\partial Z}) \tag{4.2}$$

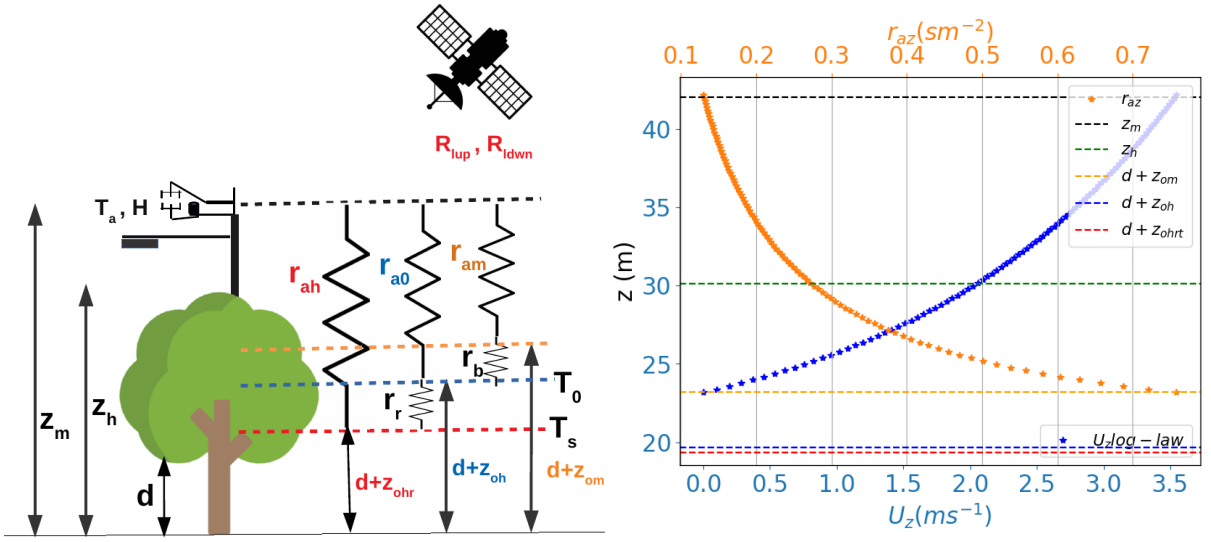

(a) (b)

Figure 4.1: Representation of canopy-scale parameterization for heat exchange resistance and logarithmic wind profile (a) representation of vertical and conceptual levels within a vegetation canopy equipped with an EC tower and radiometer for measuring surface-atmosphere exchange in the surface layer, Z_m is the measurement height, Z_h is the canopy height, d is the displacement height, Z_{om} is the roughness length for momentum exchange, Z_{oh} is the roughness length for heat exchange, Z_{ohr} is the radiometric roughness length of heat transport based on T_s (Voogt and Grimmond 2000), r_{am} is the resistance to momentum exchange, r_{a0} is the resistance to heat exchange using T_0, r_{ah} is the resistance when T_s is used for the estimation of H, r_b is the difference between r_{a0} and r_{am}, r_r is the difference between r_{a0} and r_{ah}. For homogeneous canopy, using rule of thumb, d is $\approx 60-70\%$ of Z_h and Z_{om} is $\approx 10-13\%$ of Z_h and Z_{oh} is $\approx 10-13\%$ of Z_{om} (using constant KB^{-1} of 2.3). (b) The mid-day profile for U_z using log-law and r_{az} is shown by blue cross and orange dots, respectively. r_{am} is defined as the integral r_{az} curve between $d+Z_{om}$ and Z_m (Troufleau et al. 1997), r_{a0} is the integral between $d+Z_{oh}$ and Z_m and r_{ah} is the curve area $d+Z_{ohr}$ and Z_m.

Here, $r_{az}(Z)$ $(s\ m^{-2})$ is the resistivity to sensible heat flux at a given height, Z, see Eq. (4.29), the bulk formulation for heat exchange resistance is derived by integrating the r_{az} between heat exchange roughness length (Z_{oh}) (blue dotted lines in Fig. 4.1a) to Z_m (black dotted lines in Fig. 4.1a), and the bulk heat transfer is represented as in Eq. (4.3).

$$H = \frac{\rho C_p}{r_{a0}}(T_0 - T_a) \tag{4.3}$$

Comparing Eq. (4.3) with Eq. (4.2), we can interpret r_{a0} as the integral of r_{az} between measurement height (T_a is measured) and $d+Z_{oh}$ (T_0 is measured) (area of the curve shown by orange dots in Fig. 4.1 between blue and black line), T_a is the air temperature at Z_m, and T_0 is the aerodynamic temperature. T_0 is assumed as the average air temperature near the vegetation elements within the canopy, representing the air temperature at a height $d+Z_{oh}$ above the ground. From various experimental studies it was found that $Z_{oh} \approx 10$ to 13% of Z_{om}. Since the logarithmic wind profile only begins at $d+Z_{om}$, the

resistance between $d+Z_{om}$ and $d+Z_{oh}$ is given by r_b (Fig. 4.1) and the bulk formulation for r_{a0} is expressed as a sum of r_{am} and r_b (Owen and Thomson 1963; Chamberlain 1968; Thom 1972). r_b is parameterized using the observed U^* and the logarithmic ratio of Z_{om} and Z_{oh}, often expressed as a dimensionless term KB^{-1} (Landsberg and Thom 1971; Shaw and Pereira 1982). Note that T_0 is not measured, and is usually inverted from H by satisfying the SEB (Boulet et al. 2012). Thus, T_0 and observed T_s are not similar or equal and the difference between them depends mainly on the canopy structure and vegetation type (Colaizzi et al. 2004). For the direct estimation of ecosystem-scale H using Eq. (4.1), T_s is required, which is observed widely using remote sensing at the regional-scale (Norman, Kustas, and Humes 1995). To accommodate the difference between T_0 and T_s, an additional resistance r_r is added to r_{a0} to represent r_{ah} (Fig. 4.1a). The roughness length is conceptually extended further below $d+Z_{oh}$ upto the height of the leaves surfaces, contributing to most of the emitting longwave radiation measured by the radiometers (estimation of T_s). The relevant roughness length is called radiometric roughness length (Z_{ohr}) and r_r is defined using the logarithmic ratio of Z_{om} and Z_{ohr} (Lhomme, Katerji, and Bertolini 1992; Cahill, Parlange, and Albertson 1997; Voogt and Grimmond 2000). Note that there are studies which consider T_0 is equal to T_s by modifying KB^{-1} and for these studies $r_r = 0, (Z_{ohr} = Z_{oh})$ (Verma 1989; Rigden, Li, and Salvucci 2018a).

From the above explanation, it is clear that the existing bulk formulations for heat exchange resistance, r_{ah} is an approximation of the heat exchange process by implying similarity between eddy diffusivity of momentum and heat ($K_m = K_h$). However, heat and momentum transfer mechanisms within the vegetation canopy differ as the leaf- surface's absorption and emission of solar radiation creates a temperature gradient (depending of the leaves contributing actively to the energy exchange). This makes the extension of the T_a profile within the canopy up to $d+Z_{oh}$ using the similarity theory an unrealistic assumption for H estimation. Fundamentally H is heat energy transferred between the surface and air when there is a temperature difference ($T_s - T_a$) and controlled by r_{ah} (Troufleau et al. 1997); thus, the r_{ah} parameterization plays a pivotal role in the modeling of H and LE. Due to the lack of leaf-surface representation in the existing (big-leaf, r_{ah}) formulation, empirical parameters, e.g., r_b and r_r are introduced, which also makes the direct use of field measurement difficult for r_{ah} estimation. As the value for r_b and r_r depends on Z_{oh} and Z_{ohr}, which changes with the land cover characteristics, including canopy height (Chu et al. 2018), leaf area index (Lu et al. 2009; Yang and Friedl 2003; Raupach 1994), stem density (Young et al. 2021) and atmospheric stability (Banerjee, De Roo, and Mauder 2017) and accounting for all these factors, in reality, is challenging. Previous studies have linked the model deficiencies in estimating SEB to the inadequate representation of surface roughness (Meier et al. 2022; Subin, Riley, and Mironov 2012) as Z_{oh} and Z_{ohr} are purely conceptual parameters, and estimating their optimum value

for a vegetation canopy is difficult. Studies exist where r_b parameterizations were derived and validated using eddy covariance observation (Knauer et al. 2018; Rigden, Li, and Salvucci 2018b; Troufleau et al. 1997). Due to the empirical nature of the parameterization, the validity of the formulation is limited only to the specific sites. To tackle this, a non-parametric estimate of r_{ah} is desirable that can provide insights for developing a robust resistance model for canopy-scale heat exchange.

In this chapter, we hypothesize that by coupling eddy diffusivity theory with the leaf-boundary layer resistance, we can formulate a robust model for canopy-scale heat exchange.

The objectives of the study are:

1. Infer total canopy-scale heat and momentum transport resistance from eddy covariance measurements.

2. Compare total canopy-scale resistance with existing formulations of r_{am}, r_{a0}, and r_{ah}.

3. Formulate a heat exchange resistance model by coupling vegetation sub-canopy using leaf-boundary layer resistance to the overhead canopy using eddy diffusivity.

The chapter is arranged as follows: In the section 4.2, we describe the details of the study sites and the methodology adopted for inferring r_{ah} and r_{am} using EC measurements. We also propose a new model of canopy-scale resistance, combining eddy diffusivity theory with leaf-boundary layer resistance. In Section 4.3, we present the site-specific variation in inferred r_{ah} and r_{am}. We also compared inferred resistance with resistance estimated using established parameterizations from the literature. The insights gained from the results are discussed inlight of previous findings in Section 4.4, and the conclusions are presented in Section 4.5

4.2 Methods

In this section, we describe in detail the methodology to (i) infer canopy-scale effective resistance to heat and momentum exchange using flux gradient relationship, (ii) estimate big-leaf resistance using status quo formulations, (iii) formulate self-consistent canopy-scale resistance formulations by explicitly considering leaf-canopy boundary layer. Three years of level-3 half-hourly data with quality flag zero were downloaded from terrestrial ecosystem research network (TERN) (Australia's land ecosystem observatory) and integrated carbon observation system (ICOS) for eleven EC sites with good data records, as shown in Table 4.1. The daytime observation of momentum flux (M), sensible heat flux (H), air temperature (T_a), shear wind velocity (U^*), wind speed (W_s), net radiation

(R_{net}), upwelling longwave (R_{lup}), downwelling longwave (R_{ldwn}) were used for the analysis. The criteria used to filter data for the analysis were $R_{net} > 25\ W\ m^{-2}$, $W_s > 2\ m\ s^{-1}$, $U^* > 0.1\ m\ s^{-1}$, $H > 0\ W\ m^{-2}$.

Table 4.1: Description of study sites

Study site	Latitude, Longitude	Landcover	LAI	Leaf width (m)	Canopy height (m)	Measurement height (m)
Adelaide River **(AR)**	13.0769, 131.1178	Savanna dominated by Eucalyptus tectifica and Planchonia careya	1.7	0.025	16.4	21
Alice Springs **(AS)**	22.2828, 133.2493	Mulga woodland, hummock grassland, river red gum forest	0.5	0.008	4.5	9.25
Daly Uncleared **(DU)**	14.1592, 131.3881	Woodland savanna	1.5	0.031	16.4	21
Gebesee **(GB)**	51.09973, 10.91463	Cropland	1.4	0.032	1	3.5
Howard Springs **(HS)**	12.4943, 131.1523	Open woodland savanna	1.3	0.05	16	23
Litchfield **(LF)**	13.1790, 130.7945	Tropical savanna	1.5	0.05	16	23
Neustift **(NS)**	47.1167, 11.3175	Grassland	2.6	0.002	0.7	3
Oensingen **(OS)**	47.29, 7.71	Cropland	3.9	0.01	0.7	3
Rollesbroich **(ROL)**	50.621, 6.304	Grassland	2.6	0.002	0.7	2.6
Sturt Plains **(SP)**	17.1507, 133.3502	Mitchell Grass	0.49	0.004	0.5	5
Tharandt **(TH)**	50.963, 13.566	72% spruce and 13% deciduous forest (10% larch)	4.5	0.002	30.1	42
Ti Tree East **(TT)**	22.2870, 133.6400	Grassy mulga woodland, Corymbia/ Triodia savanna	0.3	0.008	4.25	6.25
Tumbarumba **(TUM)**	35.6566, 148.1517	Wet sclerophyll	4.17	0.034	40	70
Yatir Forest **(YF)**	31.3448, 35.0519	Evergreen need-leaf forest	1.3	0.002	12	19

4.2.1 Resistance estimation using flux-tower observations

Resistance to heat exchange ($r_{ah,slope}$)

For the estimation of $r_{ah,slope}$, in the first step, the radiometric surface temperature T_s is estimated by using Eq. (4.4) with measured longwave radiation (R_{lup}, R_{ldwn}) and plot-scale emissivity (ϵ) (Thakur et al. 2022).

$$T_s = \sqrt[4]{\frac{R_{ldwn}}{\sigma} - \frac{R_{ldwn}}{\epsilon\sigma} + \frac{R_{lup}}{\epsilon\sigma}} \tag{4.4}$$

In Eq. (4.4), ϵ is the effective emissivity of the canopy footprint seen by the radiometer and σ is the Stefan-Boltzmann constant. In the second step, a robust linear regression model (scipy.stats.linegress version 1.7.0) was applied to the monthly observation of H and estimated $T_s - T_a$ as in Eq. (4.5) (Thakur et al. 2022).

$$H = m(T_s - T_a) \pm c \tag{4.5}$$

In Eq. (4.5), H is the sensible heat flux observed by EC tower, m is the monthly slope between H and ΔT, and depends on the surface characteristics and micro-meteorology (Lhomme et al. 1988) and, c is the intercept of the linear regression (interpreted as the H from EC tower footprint which is not seen by the radiometer) (Thakur et al. 2022). The functional relationship between H vs ΔT was optimized by choosing ϵ such that the root mean square error (RMSE) between H vs ΔT is minimum by optimizing T_s. The ϵ iteration starts with the maximum possible value for a grey body, 0.99, and progressively reduced with a step size of 0.002 until we reach a minimum RMSE for monthly Z_h vs ΔT regression. By comparing Eq. (4.5) with Eq. (4.1), the slope m is inverted as in Eq. (4.6) to estimate the total effective resistance between the heating surface contributing to longwave radiation (T_s) and measurement height (Z_m).

$$r_{ah} = \frac{C_p \rho_a}{m} \tag{4.6}$$

Here, r_{ah} ($s\ m^{-1}$) is the total estimated resistance to H from the longwave emitting surface seen by the radiometer to the EC measurement height (Z_m).

Total resistance to momentum transfer ($r_{am,est}$)

The total resistance to momentum transfer is given by r_{am}; it represents the resistance between $d + Z_{om}$ to Z_m as shown in Fig. 4.1. The log-law simplifies the impact of drag by considering only vegetation height Z_h and the wind speed at $d + Z_{om}$ is approximated by zero and is used widely for modeling purposes in the absence of the measured momentum flux. For direct estimation of r_{am} using flux tower measurements, we can use observed

momentum flux (M), measured wind speed (U_{Z_m}), and wind speed at $d + Z_{om}$ in Eq. (4.7).

$$r_{am,est} = \frac{\rho_a \left(U_{Z_m} - U_{d+Z_{om}}\right)}{M} \tag{4.7}$$

To estimate the wind speed at $d + Z_{om}$, we used the equations proposed by Cowan et al. (Cowan 1968), which considers the momentum transfer by the boundary layer above the plant into the air occupied by the leaves. The momentum below the canopy is dissipated with the drag force sustained by the plant surfaces (mainly leaves); thus, canopy top drag is related to the drag below canopy using an extinction factor β. To estimate top canopy wind, momentum measured above the canopy is directly proportional to the wind speed gradient as in Eq. (4.8).

$$M = \frac{\partial U z}{\partial Z} K_m \rho_a \tag{4.8}$$

Here, K_m ($s\ m^{-2}$) is called as the eddy diffusivity for momentum flux, and $\rho_a = 1.276$ ($kg\ m^{-3}$). Under the neutral atmospheric condition, the K_m immediately above the stand is related to the friction velocity by using Eq. (4.9) (Cowan 1968).

$$K_m = kU^* \left(Z - d\right) \tag{4.9}$$

Here, k is the Von Kármán constant. Substituting Eq. (4.9) in Eq. (4.8), and by substituting $M = 0.5\rho_a * U^{*2}$ with U^* constant above the stand, leads to the well-known logarithmic wind profile as in Eq. (4.10).

$$U_{z_h} = \frac{U^*}{k} \log \frac{Z_h - d}{Z_{om}} \tag{4.10}$$

U_{z_h} ($m\ s^{-1}$) is the horizontal wind speed at the canopy top estimated using log-law as a function of U^* and RLP (d, Z_{om}). The wind speed at $d + z_{om}$ ($U_{d+z_{om}}$) decreases exponentially and is expressed as a function of canopy top wind speed as in Eq. (4.11) (Cowan 1968).

$$U_{d+Z_{om}} = U_{z_h} e^{-\frac{Z_h\left(-\frac{Z}{Z_h}+1\right)}{\left(-d+Z_h\right)\log\left(\frac{-d+Z_h}{Z_{om}}\right)}} \tag{4.11}$$

Here, U_{Z_h} is the canopy top wind speed, estimated using Eq. (4.10), the log-law estimation is considered reasonable at Z_h (Verma 1989). $U_{d+Z_{om}}$ is estimated using Eq. (4.11) with measured U^*, Z_h and RLP (Z_{om}, and d) estimated using the rule of thumb given by: $d = (2/3)Z_h$, $Z_{om} = 0.123 * Z_h$. Eq. (4.7) is substituted by observed M and wind speeds to estimate $r_{am,est}$ for each half-hourly data point. The monthly value is the median of half-hourly estimated $r_{am,est}$.

4.2.2 Comparison of estimated resistance with existing aerodynamic resistance models

To compare the estimated resistance (using flux tower observations), we have chosen four widely used aerodynamic resistance models for heat exchange under both neutral and non-neutral conditions (r_{ah}, r_{a0}): (Allen et al. 1998; Verma 1989; Owen and Thomson 1963; Choudhury, Reginato, and Idso 1986a). Monthly segregated observations of U, U^*, and T_a are used to estimate half-hourly values of resistance using the following equations: Eq. (4.12), Eq. (4.14), Eq. (4.19), and Eq. (4.21).

4.2.3 Aerodynamic resistance formulation for neutral atmospheric condition

Aerodynamic resistance formulation by Allen et al.

This empirical formulation (Eq. (4.12)) was originally proposed to estimate the exchange of heat and water between the crop canopies and the atmosphere (Allen et al. 1998). It was used by the Food and Agriculture Organization (FAO) later; it was also used for the natural vegetation canopies (Liu, Mao, and Lu 2006; Trebs et al. 2021b).

$$r_{a0,Allen} = \frac{\log\left(\frac{Z_m - d}{Z_{om}}\right)\log\left(\frac{Z_m - d}{Z_{oh}}\right)}{k^2 U_z} \tag{4.12}$$

The input variables for $r_{ah,Allen}$ are: U_z, Z_m, Z_h, d, Z_{om} estimated using the rule of thumb $d = 0.67Z_h$, $Z_{om} = 0.123Z_h$, $Z_{oh} = 0.1Z_{om}$.

Aerodynamic resistance formulation by Verma et al.

One of the most widely used bulk formulation for r_{am} is shown in Eq. (4.13) (Penman and Long 1960; Verma 1989) using observed half-hourly U_z and U^* at Z_m.

$$r_{am,Verma} = \frac{U_z}{U^{*2}} \tag{4.13}$$

The r_{am} formulation is extended to r_{a0} as by assuming similarity between K_m and K_h under neutral conditions and Z_{oh} is defined below Z_{om} as shown in Fig. 4.1. Since the heat exchange from a vegetated surface encounters greater aerodynamic resistance than the momentum exchange thus, an "excess resistance" called quasi-laminar boundary layer (QBL) resistance r_b, is added to r_{am} (Verma 1989) as in Eq. (4.14).

$$r_{a0,Verma} = \frac{U_z}{U^{*2}} + \frac{\log\left(\frac{Z_{om}}{Z_{oh}}\right)}{kU^*} \tag{4.14}$$

In Eq. (4.14) Z_{oh} is estimated as 10% of Z_{om} and KB^{-1} is given by $\log(Z_{om}/Z_{oh})$.

4.2.4 Aerodynamic resistance formulation for non-neutral conditions

As the logarithmic wind profile is not valid Eq. (4.14) is modified for the non-neutral atmospheric conditions (atmospheric stability). A correction is applied to the formulation derived for the neutral conditions, which is characterized mainly by Obukhov length (L) (Owen and Thomson 1963). L is calculated by using daytime observation of canopy height (Z_h), measured air temperature(T_a), measured shear wind velocity (U^*) as in Eq. (4.15) (Thom 1972; Owen and Thomson 1963).

$$L = -\frac{T_a C_p \rho_a U^{*3}}{Hgk} \tag{4.15}$$

Here, g is the acceleration due to gravity ($m\ s^{-2}$). Half-hourly estimate of L using Eq. (4.15) is divided by measurement height (Z_m) and the ratio is represented as ξ as in Eq. (4.16).

$$\xi = \frac{Z_m}{L} \tag{4.16}$$

The range of ξ varies from -1 to 1, and its value is used to define atmospheric stability into stable, unstable, and neutral. Under stable conditions, the profile functions are linear functions of the stability parameters, and the exact solutions for aerodynamic resistance can be easily obtained. Under unstable conditions, on the contrary, the profiles are highly non-linear equations of the stability parameters, and an iterative technique (Busch, Chang, and Anthes 1976) is used to obtain the solutions. Depending on the ξ value, the correction term (ψ_h) is estimated for neutral, stable and unstable conditions as in Eq. (4.17)

$$\psi_h = \begin{cases} 2\log\left(\frac{(1-16\xi)^{0.5}}{2} + \frac{1}{2}\right) & \text{for } \xi < 0 \\ -5\xi & \text{for } \xi \leq 1 \\ -5\log(\xi) - 5 & \text{otherwise} \end{cases} \tag{4.17}$$

Verma corrected for atmospheric stability

For non neutral conditions Eq. (4.14) is corrected using ψ_h as in Eq. (4.18)

$$r_{a0Ver,cor} = \frac{-\psi_h + \log\left(\frac{Z_m}{Z_{om}}\right)}{kU^*} + \frac{\log\left(\frac{Z_{om}}{Z_h}\right)}{kU^*} \tag{4.18}$$

Formulation by Thomson et al.

Another formulation for non-neutral condition uses ψ_h to estimate $r_{a0,Thom}$ by using Eq. (4.19). This formulation gives the resistance between Z_{om} to Z_m, which is corrected for the atmospheric stability using ψ_h.

$$r_{a0,Thom} = \frac{\log\left(\frac{Z_m - d}{Z_{om}}\right) + \frac{Z_{om}\psi_h}{L} - \frac{\psi_h(Z_m - d)}{L}}{kU^*} \tag{4.19}$$

In Eq. (4.19), the RLP (d, Z_{om}, Z_{oh}) are estimated using the rule of thumb as mentioned above. The monthly median of half-hourly estimates $r_{ah,Thom}$ is compared with $r_{ah,slope}$.

Aerodynamic resistance formulation by Choudhury et al.

The atmospheric corrected r_{ah} formulation is given by using Choudhury et al. (Choudhury, Reginato, and Idso 1986b) that uses the Richardson number (RiB) to characterize the stability. It is estimated using Eq. (4.20) (Lhomme, Katerji, and Bertolini 1992). Half-hourly observation of T_a, U_z and estimated T_s are used as input dataset along with Z_m and d. T_s is estimated using Eq. (4.4) monthly optimum ϵ and observed longwave radiation (R_{ldwn}, R_{lup}) (Thakur et al. 2022)

$$Ri_B = \frac{g\,(T_a - T_s)\,(Z_m - d)}{T_a U_z^2} \tag{4.20}$$

The estimated Ri_B is used to correct the r_{ah} formulation as in Eq. (4.21):

$$r_{ah,Chou} = \frac{\log\left(\frac{Z_m - d}{Z_h}\right)\log\left(\frac{Z_m - d}{Z_{om}}\right)}{k^2 U_z\,(-\beta Ri_B + 1)^{0.75}} \tag{4.21}$$

In Eq. (4.21), Z_m is the measurement height, d is the displacement height, β is an empirical constant which accounts for the difference between T_0 and T_s and for constant variation between Z_{oh} and Z_{ohr} , $\beta = 5$ is used, $d = 0.56Z_h$, $Z_{om} = 0.3(h - d)$, $Z_{oh} = Z_{om}/7$. The monthly median of half-hourly estimates $r_{ah,Chou}$ is compared with $r_{ah,slope}$.

4.2.5 Leaf-canopy-air resistance model (r_{lca})

For the realistic representation of leaf-canopy-air exchange, we proposed a novel resistance model named the leaf-canopy-air resistance model (r_{lca}) by diving the resistance component in leaf-canopy (r_{lc}) and canopy-air resistance (r_{ca}) as shown in Fig. 4.2. Comparing the proposed resistance components to a big-leaf model, we can express H as in Eq. (4.22).

$$H = \frac{C_p \rho_a\,(T_0 - T_a)}{r_{ca}} + \frac{C_p \rho_a\,(T_s - T_0)}{r_{lc}} \tag{4.22}$$

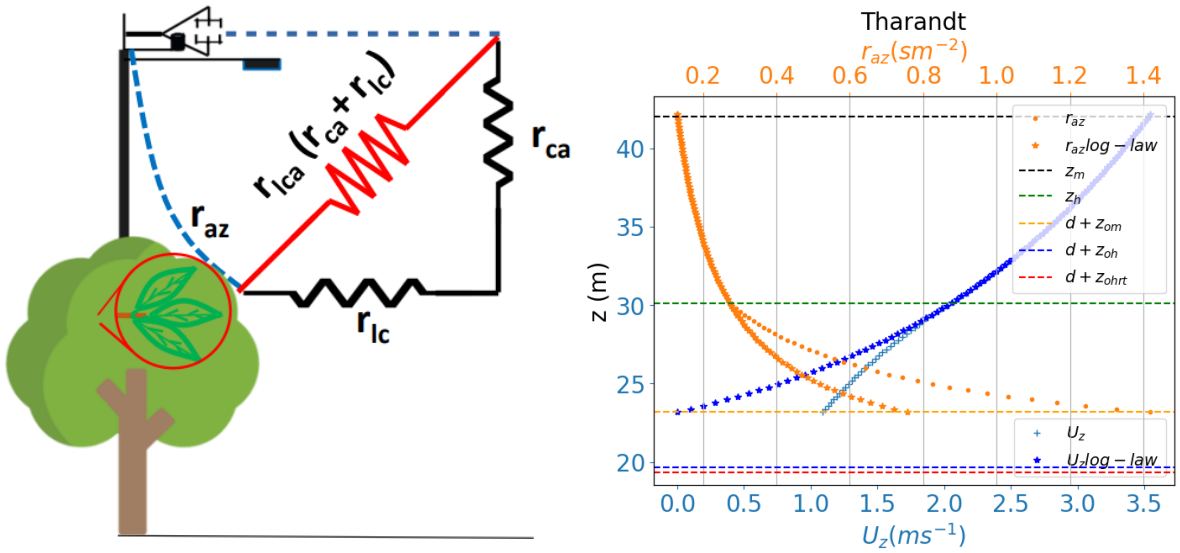

(a) (b)

Figure 4.2: Schematic representation of proposed leaf-canopy-air resistance model and wind variation within canopy using log-law and exponential function. (a) The canopy-air resistance (r_{ca}), which is equal to the integral of r_{az} between source height (Z_h or Z_{om} or Z_{oh}) and Z_m. r_{lc} is the leaf boundary layer resistance at source height obtained using L_l, LAI and U_z, r_{lca} is the total resistance to heat exchange obtained by adding r_{lc} to r_{ca} and will represent the r_{ah} as shown in Fig. 4.1. (b) U_z (blue stars) estimated using Eq. (C.2) and r_{az} (orange stars) considering logarithmic variation in the wind speed (Chamberlain 1968). r_{az} and U_z profile (blue cross) estimated using Eq. (C.1) r_{az} (orange dots) using exponential decay within canopy assuming constant LAI (Cowan 1968). The mid day data used for the plot is from a pine forest site in Germany, Tharandt(2017/06)

As turbulent eddies mainly drive the momentum exchange within and above the canopy, the transfer of heat within the canopy is also affected by both turbulent and radiative processes. Thus, using similarity ($K_m = K_h$), we only extended T_a profile up to the canopy top (Z_h) starting from the measurement height Z_m. Note that in big-leaf models the T_a profile in extended upto $d + Z_{oh}$ (T_0, shown by blue dotted line Fig. 4.1a).

Canopy-air resistance (r_{ca})

The wind speed in the lower atmosphere is expressed in two ways: (i) using log-law, which assumes that the wind speed varies logarithmically with height above the ground; as we go higher, the wind speed increases at a decreasing rate (Penman and Long 1960; Thom 1972) and (ii) the exponential profile which assumes the vegetation structure acts as a drag on the wind, and the wind speed decreases rapidly as it moves through the canopy (Inoue 1963; Cowan 1968). By assuming a logarithmic wind profile above the canopy and exponential wind below the canopy, the piecewise equation for U_z is defined as shown in

Fig.4.2.

$$U_z = \begin{cases} \dfrac{U^* e^{-\frac{h\left(-\frac{Z}{h}+1\right)}{(-d+h)\log\left(\frac{-d+h}{Z_o}\right)}} \log\left(\frac{-d+h}{Z_o}\right)}{k} & \text{for } Z \leq h \wedge Z > 0 \\ \dfrac{U^* \log\left(\frac{Z-d}{Z_o}\right)}{k} & \text{for } Z > h \end{cases} \tag{4.23}$$

Following an approximate similarity between (K_m/U_z) ratio below and above canopy and we express the below canopy wind speed as a function of above canopy wind as shown in Eq. (4.11) and using Eq. (4.8) we obtain the K_M profile and by inverting the K_M equation we obtain the momentum resistivity (r_{az}) as in Eq. (4.24).

$$r_{az}(z) = \begin{cases} \dfrac{e^{\frac{h\left(-\frac{Z}{h}+1\right)}{(-d+h)\log\left(\frac{-d+h}{Z_o}\right)}}}{kU^*(Z-d)} & \text{for } Z \leq h \wedge Z > 0 \\ \dfrac{1}{kU^*(Z-d)} & \text{for } Z > h \end{cases} \tag{4.24}$$

An exemplary r_{az} profile for one of the study sites (TH) is shown in Fig. 4.2b. The integral of the r_{az} between two vertical levels give us the r_{ca} value as in Eq. (4.25).

$$r_{ca} = \int_{Z_1}^{Z_m} r_{az}\, dz \tag{4.25}$$

We estimated r_{ca} by using $Z_1 = Z_h$ or Z_{om} in Eq. (4.25).

Leaf-canopy resistance

Surface resistance close to the heat-exchanging leaves is represented using leaf-boundary layer resistance (r_{lc}). By considering heat exchange from both sides of the leaf and considering all leaf's resistance are in parallel contributing to the within canopy exchange, the r_l formulations proposed by Schymanski et al. (Schymanski and Or 2017) is divided by twice the average LAI at the study sites (see Table 2.1 for LAI values).

$$r_{lc} = \frac{L_l C_p \rho_a}{2 L_{ai} N_{Nu_L} k_a} \tag{4.26}$$

L_l is estimated by calculating the weightage percentage contribution of leaf sizes at the study site. The yearly average LAI values at the study sites are used to estimate r_{lc} (Table. 2.1). For the estimation of critical reynolds number (Re_c), U_z at Z_h is used, which is estimated using Eq. (4.11). For the estimation of N_{NuL} measured T_a is used. Note that the difference between r_{lc} estimated using canopy top $T_{a,h}$ (using Eq. (4.3)) and measured T_a was negligible (as shown in Fig. C.11), so for the ease of calculation we used observed T_a. Estimated r_{lc} at two heights (canopy top (Z_h, aerodynamic height of

heat exchange (Z_{d+oh}) and r_{ca} for each time-stamp is added using Eq. (4.27).

$$r_{lca} = \frac{L_l C_p \rho_a}{2 L_{ai} N_{Nu_L} k_a} + \int_{Z_h}^{Z_m} r_{az}\, dz \tag{4.27}$$

The monthly median of modeled r_{lca} is compared to the monthly median of $r_{ah,slope}$ by using a scipy linear regression model. To quantify the the range of variation in r_{lca} with varying L_l and Z_h we plotted a contour plot for r_{lca} by using measured data at AR and varying Z_h between (1 to 16.4 m) and L_l in the range of 0.0025 m to 0.005 m (Fig.C.10b)

4.2.6 Modeling diurnal H using r_{lca}

Keeping SEB modeling perspective in mind, we attempted to test our resistance model (r_{lca}) for daily prediction of H at the study sites using Eq. (4.28). Note that to use Eq. (4.22) we require $T_{a,h}$ (which can be obtained using Eq. (4.2) and H). To simplify the calculations (without iterations), Eq. (4.22) is simplified to Eq. (4.28) as shown below:

$$H_{mod} = \frac{C_p \rho_a \left(T_s - T_a\right)}{r_{lc} + r_{ca}} \tag{4.28}$$

In Eq. (4.28), r_{lc} is estimated using Eq. (4.26) with observed U^*, U_z, T_a and r_{ca} is estimated by integrating Eq. (4.29) from Z_h to Z_m. In the absence of U^*, the observed wind speed at the meteorological station can be used to estimate the U_* roughly, as shown by Kent et al. (Kent et al. 2018).

$$r_{az} = \frac{1}{kU^* \left(Z - d\right)} \tag{4.29}$$

r_{lc} is estimated using Eq. (4.26). The diurnal value of r_{lca} (r_{lc}+r_{ca}) with estimated $T_s - T_a$ is used in Eq. (4.28) to obtain H_{mod}. The median value of hourly H_{mod} is compared with the measured H at the study sites to evaluate the performance of r_{lca}.

4.3 Results

4.3.1 Inferred canopy-scale resistance ($r_{ah,slope}$ and $r_{am,est}$)

The slope of monthly H vs ΔT estimates the ecosystem-scale effective resistance to daytime heat exchange represented by $r_{ah,slope}$. The inferred resistance using three years of daytime measurements decreases exponentially with increasing Z_m at the study sites as shown in Fig. 4.3a. An exponential curve was fitted through the median values of the $r_{ah,slope}$ (Fig. 4.3b). Note that the measurement height depends on the canopy height, land-cover type, and wind speed. We calculated the resistance to momentum exchange

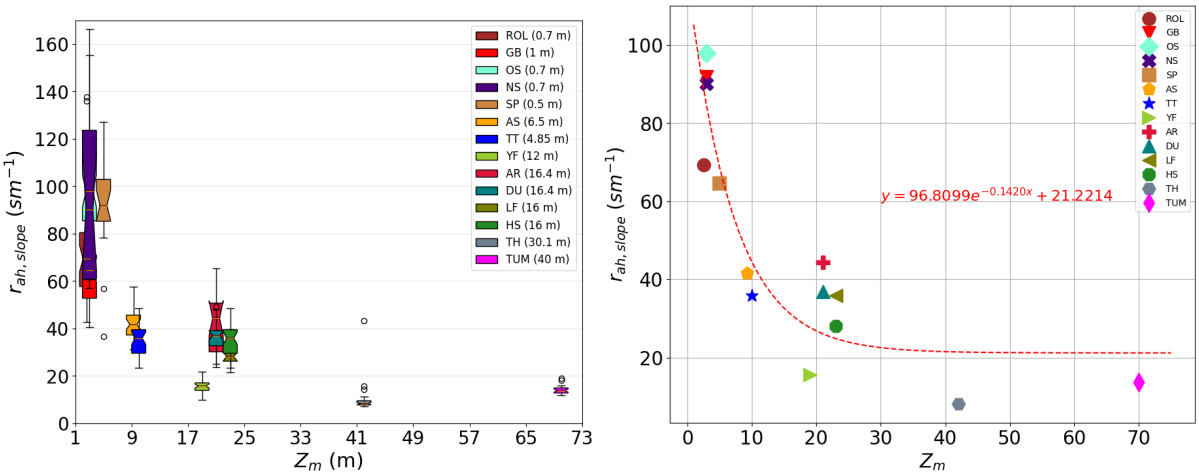

(a) (b)

Figure 4.3: Variation in $r_{ah,slope}$ with the measurement height across the study sites. (a) total resistance to heat exchange for three years with the measurement height (Z_m) at the study sites. The plot legend (in bracket) shows the average canopy height at the study sites. Monthly r_{ah} is estimated by inverting the slope (m) of monthly H vs ΔT plot as shown in Eq. (4.6). Lower and upper box boundaries represent the 25th and 75th percentiles, respectively; line inside the box median; lower and upper error lines 10th and 90th percentiles, respectively, filled circles data falling outside the 10th and 90th percentiles. (b) Exponential function ($ae^{-bx} + c$) fitted through the median of $r_{ah,slope}$ using optimize curve fit from SciPy().

($r_{am,est}$) using observed M, U_z, and estimated wind speed at $Z_{om} + d$, and found an approximate exponential decrease in the values of $r_{am,est}$ with increase in Z_m as shown in Fig. C.2c. TUM was an outlier as the measurement height was 30 m above the canopy top wind speed at the height is very high resulting in exceptionally low resistance. The inferred momentum resistance ($r_{am,est}$) was lower than heat exchange resistance $r_{ah,slope}$ at all the study sites (see Fig. C.2b and Fig. C.2c).

4.3.2 Comparison between inferred resistance value with existing resistance formulations

Five widely used big-leaf resistance formulations (r_{a0}, r_{ah}) from the literature and $r_{am,est}$ are used with EC measurements to estimate hourly values at the study sites. A linear regression model (SciPy linregress()) was used to compare the monthly median of inferred resistance, $r_{ah,slope}$, with the estimated resistances. The comparison was made using Pearson coefficient (ρ), slope (m), and RMSEs (one for linear regression and the other for 1:1 line) as shown in Table 4.2. An exemplary comparison plot between $r_{ah,slope}$ and $r_{a0,Verma}$ is shown in Fig. 4.4, and a comparison plot for other formulations is shown in the Fig. C.4. An exponential curve was fitted to the median values of the $r_{a0,Verma}$ at the study sites, and AS and TT was placed outside the exponential curve as shown in Fig. 4.4b, exponential curve fitting with the other formulations are shown in Fig. C.2. The highest ρ was estimated for $r_{a0,Verma}$ followed by $r_{a0,Ver,corr}$ and $r_{am,est}$. The

resistance formulations corrected for atmospheric stability (Thom 1972; Choudhury and Monteith 1988; Verma 1989) have lower m, and high RMSE. The ρ is lower for $r_{ah,Chou}$ and $r_{a0,Thom}$ and highest for $r_{a0,Ver,Cor}$. The lowest value of RMSE (1:1) was for $r_{a0,Allen}$ followed by $r_{a0,Verma}$ and $r_{am,est}$. The regression slope < 1, indicates, on average, an underestimation of r_{ah} by existing formulations. All r_{ah} estimated for neutral condition shows an underestimation for the inferred resistance (benchmark resistance) $r_{ah,slope}$ and the stability corrected formulations shows a different seasonality (exemplary plot for DU is shown in Fig. C.8).

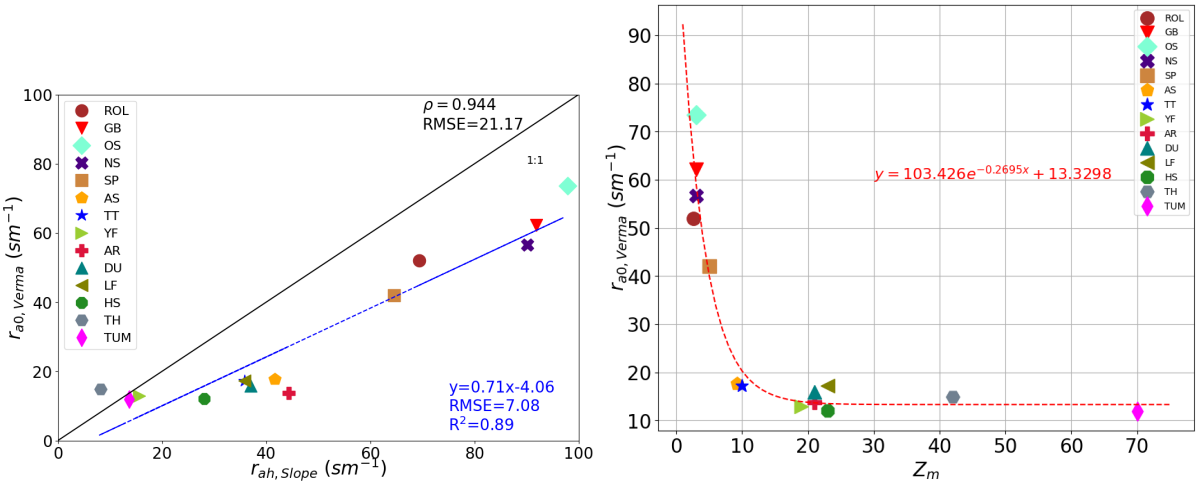

(a) (b)

Figure 4.4: Median values of $r_{a0,Verma}$ estimated using three years of eddy covariance data using Eq. (4.14) at the study sites (a) Comparison between the median values of inferred resistance ($r_{ah,slope}$) in the x-axis and $r_{a0,Verma}$ in the y-axis using linear regression model (SciPy) (b) exponential curve ($ae^{-bx} + c$) fitted to the $r_{a0,Verma}$ using optimize from SciPy curve fit().

Table 4.2: Comparison table for $r_{ah,slope}$ with status quo bulk resistance model using half hourly eddy covariance data for three years by combining measurements from all sites. The Pearson coefficient (ρ) RMSE (1:1) is estimated for a 1:1 line, and the other regression parameters, slope (m) and RMSE are estimated using SciPy().

Bulk Formulation	Pearson coefficient	Equation (y=mx+c)	RMSE (1:1)	RMSE
$r_{a0,Verma}$ (1989)	0.944	0.71x - 4.06	21.17	7.08
$r_{a0,Ver,cor}$ (1989)	0.932	0.33x + 0.23	36.98	3.73
$r_{a0,Allen}$ (1998)	0.775	0.28x + 9.15	33.23	6.55
$r_{am,est}$ (2022)	0.891	0.47x + 0.05	30.58	8.72
$r_{ah,Chou}$ (1986)	0.658	0.24x + 7.71	36.92	7.76
$r_{a0,Thom}$ (1980)	0.46	-0.28x + 40.8	45.2	15.68

4.3.3 Proposed leaf-canopy-air resistance model for heat exchange

The proposed leaf-canopy resistance (r_{lca}) model calculates total resistance by coupling canopy-air resistance (r_{ca}) with leaf-canopy resistance (r_{lc}). r_{ca} is estimated as the area

of the r_{az} curve, integrated between heat source height (Z_h or Z_{om}) and the measurement height (Z_m). The aggregated resistance of all the leaf surfaces participating in the surface-energy partioning (r_{lc}) is estimated as explained in section 4.2.5. Site-specific r_{lca} is represented as the monthly median of daytime $r_{ca} + r_{lc}$ and is compared to the $r_{ah,slope}$ as shown in Fig. 4.5. The comparison of $r_{ah,slope}$ with r_{lca} resulted in ρ (0.725) and m (1.14) as shown in Fig. 4.5a. Comparing Fig. 4.5a and Fig. 4.5b we see that to reproduce $r_{ah,slope}$ the source height at TUM, TH, LF should be located at Z_h as shown in Fig. C.6a, whereas the source height at Z_{om} for other sites resulted in Fig. C.6b. The estimated r_{ca} for SP is resulting in a very high value (due to lower vegetation height meaning 0.5 meters) which is also reducing ρ=0.70 (Fig. 4.4), by eliminating SP from the plot considering the non-realibality of eddy diffusivity theory near ground (used to estimate r_{ca}) we get ρ=0.945. The underestimation of r_{lca} at savanna sites can be attributed to the patchy distribution of trees and grasses, making the source height location site-specific (meaning it can be Z_h, Z_{om} or other heights). Also, the adequate leaf size at AR is half the effective L_l at other Savana sites. Additionally, the Z_m for HS and LF is 2 m higher than for DU and AR; however, the average Z_h at DU and AR is 0.4 m higher than LF and HS affecting the estimate of r_{ca} (Fig. C.3). The contour plot (Fig. C.10b) for r_{lca} with varying average Z_h and L_l shows that with vegetation canopy of eight meters or above both L_l and Z_h have a similar effect on the magnitude of r_{lca} considering Z_m and LAI are constant. All the existing parameterizations underestimate resistance compared

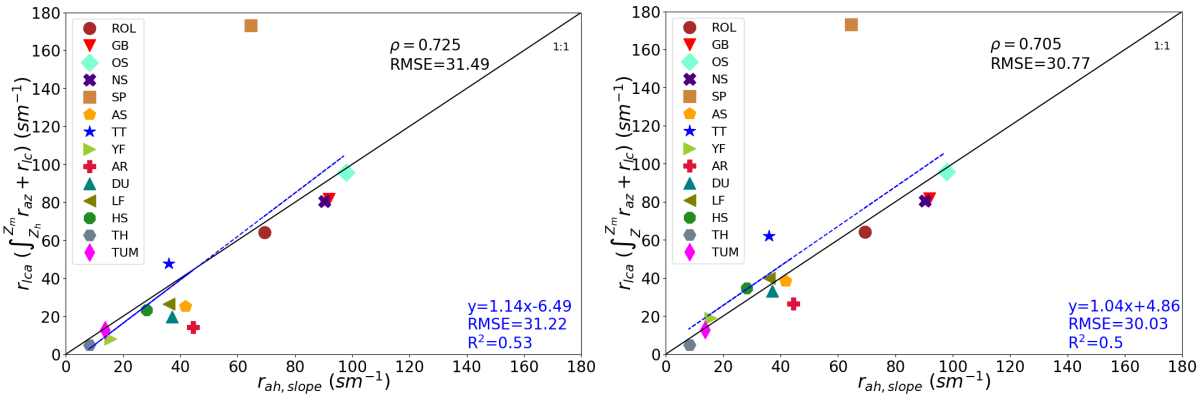

(a) (b)

Figure 4.5: Comparison plot between median values of r_{lca} and $r_{ah,slope}$ at study-sites having $LAI > 1$.(a) r_{ca} estimated by integrating r_{az} between Z_h to Z_m added to and r_{lc} is estimated using Eq. (4.26) to represent r_{lca} (b) r_{ca} is estimated by integrating r_{az} between Z_{om} to Z_m and r_{lc} is estimated using Eq. (4.26) and is added to represent r_{lca}.

to $r_{ah,slope}$ as shown in Table. 4.2 we added r_{lc} to check if the RMSE (1:1) decreases as shown in Table. 4.3. We found for all the formulations; the RMSE (1:1) decreased. The maximum ρ is obtained by adding $r_{a0,Verma}$ to r_{lc} followed by $r_{a0,Verma}$ (Fig. C.5) and r_{ac} (Fig. 4.5a,b). For sites with LAI > 1 we found adding r_{lc} to existing formulation results in an increase in the ρ and m.

Table 4.3: Comparison table between $r_{ah,slope}$ and $r_{ac} + r_{lc}$. r_{lc} is estimated using Eq. (4.26) with wind speed at Z_h and the r_{ac} value is replaced by the existing bulk formulations. The Pearson coefficient (ρ) is estimated for a 1:1 line, and the other regression parameters, slope (m) and RMSE, and correlation coefficient (R^2) are estimated using SciPy linregress().

Bulk Formulation	Pearson coefficient	Equation (y=mx+c)	RMSE (1:1)	RMSE
$r_{a0,Verma} + r_{lc}$	0.92	0.68x + 9.57	13.52	8.34
$r_{a0,Allen} + r_{lc}$	0.625	0.26x + 22.46	26.42	9.4
$r_{am,est} + r_{lc}$	0.681	0.45x + 13.46	24.44	13.73
$r_{a0,Thom} + r_{lc}$	0.76	0.39x + 19.89	22.04	9.57
$r_{lc} + \int_{Z_h}^{Z_m} r_{az}$	0.725	1.14x - 6.49	31.49	31.22
$r_{lc} + \int_{Z_{om}}^{Z_m} r_{az}$	0.705	1.04x + 48.6	30.77	30.03

As shown in Table 4.2 existing formulations underestimate the resistance value at most of the study sites in comparison to the $r_{ah,slope}$ and resulted in the high value of RMSE (1:1). To check the applicability of the proposed r_{lc} for the existing model, we added r_{lc} to $r_{a0,Verma}$ formulations and compared it with inferred resistance as shown in Fig. B.6a. To understand the component-wise difference between the surface resistance to the canopy-air resistance, we compared proposed r_{lc} with r_b estimated and r_{ca} with r_{am} estimated using Verma et al. (Verma 1989) as shown in Fig. B.6b,c. Comparison of estimated r_{ca} (by using r_{az} integral between Z_{om} to Z_m) with $r_{am,Verma}$ results into a lower value than the r_{ac} as shown in Fig. B.6c). It is because $r_{am,Verma}$ is derived using log-law, which is valid above $d + Z_{om}$ so the area of r_{az} curve is smaller (orange stars in Fig. 4.2b) compared to r_{az} profile using exponential profile for sub-canopy wind variation (orange dots in Fig. 4.2b). Comparison of $r_{a0,Verma}$ with r_{lca} (r_{ca} between Z_h and Z_m) results into higher ρ overall, overestimation at pine forest by $r_{a0,Verma}$ and an underestimation at HS and GB (Fig. B.6d).

4.3.4 Modeling sensible heat (H_{mod}) using r_{lca}

Hourly estimates of $T_s - T_a$ and r_{lca} are used to model hourly H as shown in Fig. 4.7. We have chosen four sites to compare the hourly variation in modeled sensible heat (H_{mod}) with measured sensible heat (H_{meas}) and $H_{rah,slope}$ using $r_{ah,slope}$ with estimated $T_s - T_a$. The difference between H_{mod} and $H_{rah,slope}$ was inversely proportional to the difference between r_{lca} and $r_{ah,slope}$ and directly proportional to the difference between $T_{a,h}$ and T_a as we have simplified Eq. (4.22) by using Eq. (4.28). The difference between $T_{a,h}$ and T_a is higher for YF (see Fig. C.1b), and the magnitude of r_{lca} (Eq. (4.28)) is smaller resulting into an overestimation of H_{mod}. At GB with a high value of $r_{ah,slope}$, the H_{mod} is closer to H_{meas} as higher r_{lca} counterbalance the effect T_a (Fig. 4.7d). The difference between H_{mod} and $H_{rah,slope}$ will depend on the sign and value of intercept (Thakur et al.

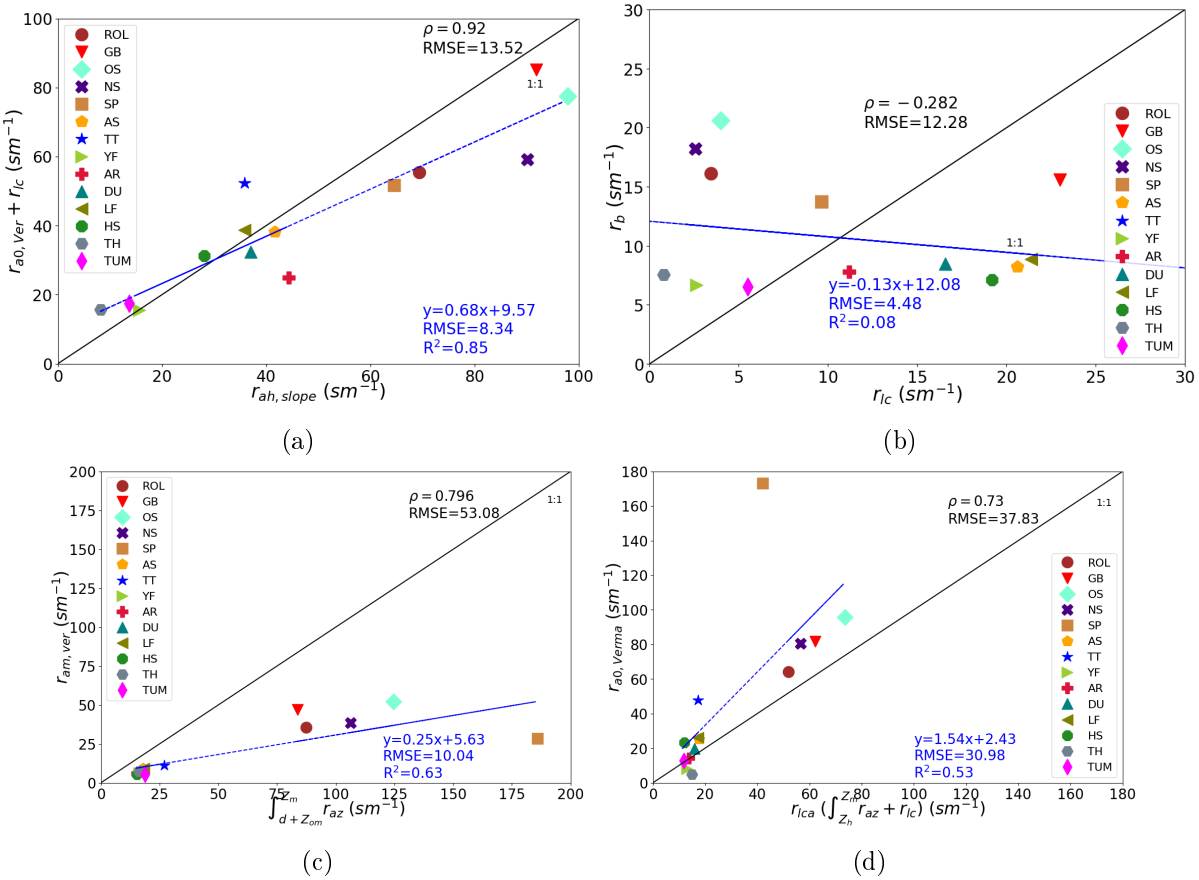

Figure 4.6: Comparison of the resistance formulations (a) $r_{ah,slope}$ in the x-axis by combining r_{lc}+ $r_{a0,Verma}$ in the y-axis.(b) near-surface resistance to heat exchange r_{lc} in x-axis with r_b in y-axis estimated using Eq. (C.12) (c) canopy-air resistance (r_{ca} between $Z_{d+Z_{om}}$ to Z_m) with r_{am} estimated using Eq. (4.13) (d) estimated r_{lca} (by combining r_{lc} with estimated r_{ca} between Z_h and Z_m in the x-axis with $r_{a0,Verma}$ in y-axis.

2022). For instance, at YF and TUM, the intercept (c) for H vs. ΔT is negative, which means the sensor sees more soil than trees leading to a higher value of average T_s. The combined effect of lower r_{ah} values and overestimation of $T_s - T_a$ (we assume $T_{a,h} = T_a$) lead to an overestimation at YF and TUM. (Fig. 4.7).

4.4 Discussion

Our results show that the monthly slope of daytime H vs ΔT regression can, on average, represent the site-specific variation in the total effective resistance to heat exchange ($r_{ah,slope}$) at the ecosystem-scale. We found an exponential decrease in the heat exchange resistances with increasing Z_m (see in Fig. 4.3b). This trend can be attributed mainly to two concepts used to derive these formulations: (i) the wind speed increases at a decreasing rate as Z_m increases (log-law), (ii) parameterization of resistance near the heat-exchanging surfaces (QBL resistance). The logarithmic increases in the wind speed result in an exponential decay of air resistance due to enhanced mixing. All the aerodynamic resistance formulations follow the exponential pattern on average, as shown in Fig.

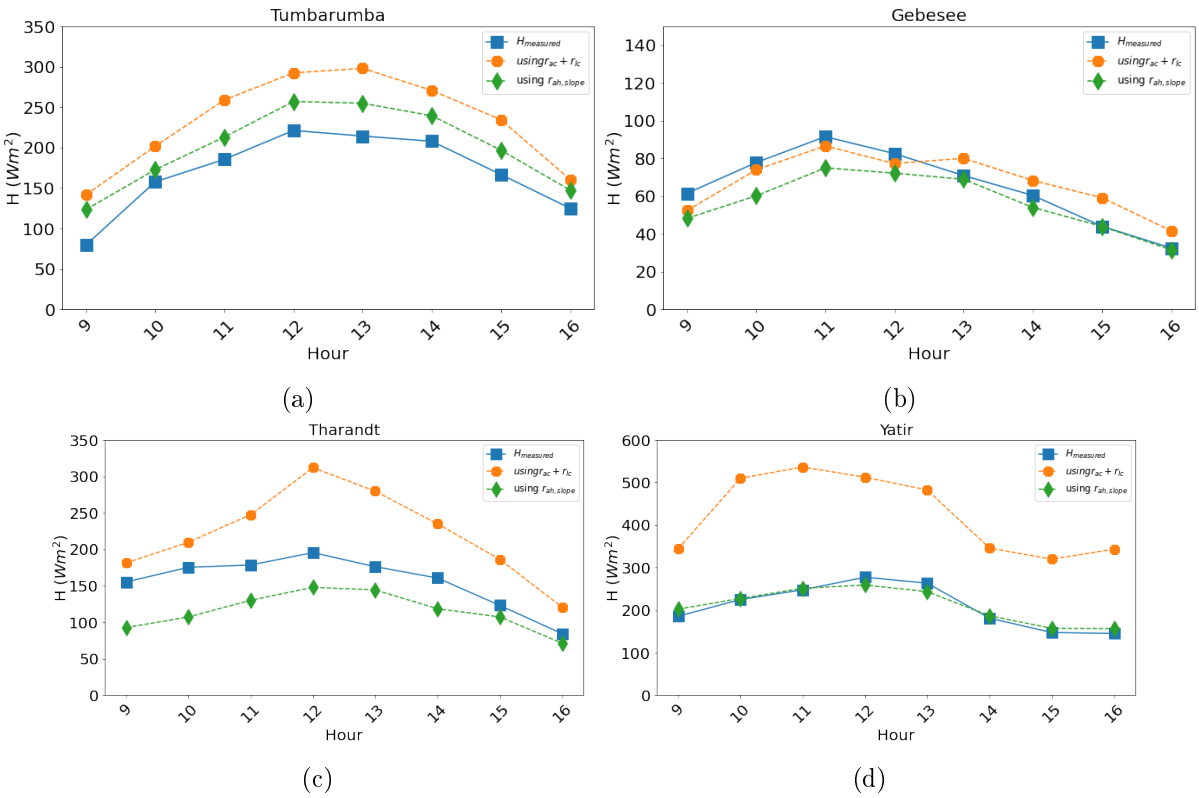

Figure 4.7: Comparison plot for hourly median values using three years of observed H, H_{mod} generated using estimated $T_s - T_a$ and r_{lca}. $H_{rah,slope}$ is estimated using $r_{ah,slope}$ and $T_s - T_a$ for (a) TUM, (b) GB, (c) TH, and (d) YF.

C.2. However, the outliers to the exponential $r_{ah,slope}$ curve (lower value at YF, TH and higher value at AR see Fig. 4.3b) are not captured by any of the bulk formulations. It is because these formulations use KB^{-1} instead of the surface characteristic length and within canopy microclimate for parameterizing near-surface resistance (r_b, r_r). Our proposed parameterization for QBL resistance is r_{lc}, which uses the sub-canopy wind speed, characteristic leaf length, and LAI to capture near-surface resistance at the study sites adequately. The proposed canopy-air resistance (r_{ca}) accounts for the canopy structure by using different integral length-scale (Z_h, $d + Z_{om}$) to represent the position of heat source height at the EC sites. Therefore, our proposed resistance model r_{lca} best reproduces $r_{ah,slope}$ across most of the land cover types in comparison to previous bulk formulations (compare Table 4.3 to Table 4.2). The r_{ca} estimate at the SP results in a significantly higher value, which can be explained by the assumption of eddy diffusivity, which states turbulent eddies exist at all scales and can be modeled using an eddy diffusivity coefficient. However, in small canopies, the size of the canopy elements (e.g., individual leaves, canopy arrangement) becomes comparable to the size of the turbulent eddies, leading to a breakdown of the assumption of constant flux, as the interaction between the canopy elements and the turbulence becomes more significant and local (Denmead and Bradley 1985). The physically based representation of r_{lca} explains the site-specific resistance values using canopy structural characteristics (heterogeneity due to trees, grasses, leaf shapes, sizes, and densities). Thus, the smaller r_{lca} at patchy study sites can be ex-

plained by the non-representativeness of source height using a single value, as tall trees are sparsely distributed with grass cover in between. The difference in the observed H and H_{mod} modeled (using r_{lca} and estimated $T_s - T_a$) across study sites was consistently explainable by the difference of r_{lca} and $r_{ah,slope}$. However, the adequacy of $r_{ah,slope}$ to represent observed H depends on the intercept, which accounts for the footprint mismatch between estimated T_s and observed H and T_a (Thakur et al. 2022). These results show that the proposed r_{lca} represents the complex coupling of leaf-canopy-air resistance in a physically consistent manner.

The inferred resistance to heat exchange ($r_{ah,slope}$) at YF is smaller than the other broad-leaf forest sites with a similar range of canopy height as shown in Fig. 4.3. The observed smaller value of r_{ah} at YF has been referred to as the canopy convector effect (CCE) by stating that the r_{ah} is inversely proportional to the plant area index (PAI), which includes the area of all heat exchanging surfaces, including stems, branches, and total needle surface (Rotenberg and Yakir 2010; Sellers et al. 1996). The open canopy structure and low tree density at YF increases the PAI, which efficiently reduces the resistance to heat exchange, making YF relatively cooler ($T_s - T_a < 5K$) than the surrounding Negev desert ($25K < T_s - T_a < 35K$) and the shrublands (Rotenberg and Yakir 2011). Since r_{az} is parameterized using U^* and d (see Eq. (4.24)) without considering the shape of the leaves, thus, none of the bulk formulations could capture the differences in resistance at YF compared to broad-leaf forests (shown in Fig. C.4). In the introduction, we explained how the bulk parameterizations account for the surface resistance (QBL resistance) by extending the r_{az} curve below $d + Z_{om}$ to $d + Z_{oh}$ without accounting for the distributed heat emitting sources (leaves). As shown in Fig. C.1, the r_{az} increases drastically within the canopy, and the area of the curve between $d + Z_{om}$ to $d + Z_{oh}$ will depend on the interactions between the flow of air and the complex structure of the canopy. Theoretically speaking, the curve should be different for heat and momentum exchange within the canopy as the driving force for the momentum exchange is friction; on the other hand, heat exchange is governed by the difference in temperature between the surface and the air (which varies within canopy), thermal conductivity and specific heat capacity. The canopy structure and the geometry of the heat-contributing surfaces (leaves) can affect the heat exchange largely in comparison to the momentum exchange (see Fig. C.2a,c). Therefore, the needle-shaped leaf at YF and TH interferes with the QBL by forming more eddies (increasing mixing). In contrast, the patchy land cover consisting of grass and trees at AR will reduce the effective surface roughness, leading to increased resistance (see contour plot of r_{lca}, Fig. C.10b).

For most of the North Australian Transect (NATT) forest sites ($LAI > 1$), the r_b estimate is smaller than r_{lc} (except for TUM), whereas, for the needle forests, the r_b estimate is significantly greater than r_{lc} as shown in Fig. B.6b. The difference in the two QBL resistance values (r_b and r_{lc}) can be explained by the heterogeneous canopy

structure at the NATT sites comprised of trees and long grasses, creating a larger surface for heat exchange as shown by the higher value of r_{lc}, whereas, needle-shaped leaves at YF and TH decreases the total area of surfaces as shown in Fig. B.6b. For sites with LAI values between 1 to 2.5, we found similarity in the seasonality of r_b and r_{lc} (Fig. B.6b, c), however, the estimated r_b is half the value of r_{lc}. Previous studies have discussed the underestimation of r_b for forested and cropland sites inlight of the constant KB^{-1}, as with the increase in the LAI, the Z_{oh} increases faster than Z_{om} (see the second term of Eq. (4.14) (Landsberg and Thom 1971). As shown in Fig. C.9b,c, estimated r_b value is almost constant across sites although, the canopy composition is different (Table 2.1). Practically, the magnitude of heat exchange surface resistance should depend significantly on: solar angle, solar radiation, and geometry of vegetation (leaves, stems, branches, and their arrangement), and no existing r_b framework can adequately model all the factors, since the parameterization uses U^* and Z_h to parameterize source height (d+Z_{oh}). Looking at the canopy structure at TUM, we found that the canopy consists of tall trees sparsely distributed with long bushes between, which means our assumption of constant LAI is not valid. Our analysis showed that the source height depends on the canopy type, as shown in Fig. 4.5 for closed canopies with high LAI, the source height can be considered at Z_h whereas, for open canopy and patchy canopy, we need to consider source height within the canopy ($d + Z_{om}$). We also found that the resistance underestimation using r_{lca} (in comparison to the inferred value) at patchy study sites (mix vegetation type with different average height) is due to the inadequate representation of the source height (in reality, there will be two sets of RLP representing the trees and grasses). As seen in Fig. C.10b, to reproduce the median of $r_{ah,slope}$ at AR using r_{lca}, we can add the resistance offered by a tree ($Z_h = 16.4\ m$) having L_l =0.0025 m with the resistance offered by grasses ($Z_h = 1.5\ m$) having L_l =0.0025 m. The Z_m at HS and LF is 2 m higher than the Z_m at DU and AR. The average Z_h at DU and AR is 0.5 m higher than LF and HS, resulting in different values of r_{ca}. The r_{lc} value at LF and HS is similar, while, it is smaller at AR, due to smaller effective L_l (see Table 2.1). The difference between r_{lca} values at LF and HS is mainly due to the observed U_z and U^*.

All of the existing resistance formulations for neutral condition, underestimates of r_{ah} resulting in an overestimated T_s the error in T_s is compensated by assigning KB^{-1} correction such that the observed $H + LE$ is reproduced. The resistance to water vapor exchange is represented as the sum of $r_{ah} + r_s$. In inverse modeling where r_s is deduced from measured LE, r_{ah} underestimation lead to r_s overestimation resulting in a biased estimate of carbon exchange and underestimation of water use effeciency, which affects our understanding of land-cover response to changes in environmental conditions (changes in temperature and precipitation).

4.5 Conclusion

The proposed leaf-canopy-air resistance model (r_{lca}) significantly improved the reproduction of benchmark resistance to heat exchange between the canopy and the atmosphere. This improvement is significant as it enhances our ability to accurately predict and understand heat exchange processes in the canopy-atmosphere interface. The r_{lca} model consistently couples the leaf boundary layer with study-specific observations (fluxes, wind speed, and air temperature) and outperforms all existing resistance models. Among the existing parameterizations, the resistance formulation by Verma et al. (Verma 1989) performed best. However, it overestimated surface resistance in needle forests and underestimated canopy-air resistance. Conversely, surface resistance was underestimated for broad-leaf forests, and canopy-air resistance was overestimated. The proposed canopy-air resistance model integrates resistivity between two heights, simplifying model parameterization by considering the canopy structure. For a mixed canopy-like savanna consisting of long bushes and trees, the lower integral is within the canopy more so than in a homogeneous forest, forming a smooth surface with lower resistance. Additionally, the lower limit of the integral is closer to the canopy top. Proposed resistance model integrates the canopy-air resistance (canopy microclimate, canopy height) with leaf-canopy resistance (leaf length, leaf area index, air temperature, wind speed), making it robust for understanding site-specific processes that determine vegetation-atmosphere interactions. Physically-based description of the the complex interactions between leaf-surfaces and eddies in the proposed model, with its straightforward nature user-friendly provides a more accurate estimation of aerodynamic resistance compared to existing empirical models, making it a valuable tool for making informed decisions about the impact of land cover types on microclimate and for estimating ecosystem-scale heat exchange.

4.6 Code and data availability

The data and code used for this study is freely available from zenodo.org (https://zenodo.org/records/8015487)

Chapter 5

Conclusions and Summary

Contents

5.1 Summary

The main goal of the research was to:
1. Develop a method to estimate ecosystem-scale emissivity and surface temperature using flux tower measurements.
2. Quantify the impact of surface heterogeneity on footprint mismatch and its implication for combining eddy-covariance and radiometric measurements.
3. Formulate a self-consistent model (considering leaf surface and canopy-air space) to estimate ecosystem-scale physical resistance to energy and water exchange.

In Chapter 2, a novel method for simultaneous estimation of LST and emissivity at the ecosystem-scale is developed by combining the observed longwave (emitted and reflected) components with H and T_a at flux tower sites with different land cover types. The consequences of omitting downwelling longwave radiation, a common practice in the literature for estimating LST and emissivity, are addressed in detail. Also, ecosystem-scale surface temperature is compared with satellite-derived LST (MODIS product MOD11A1). It was found that the LST values obtained using both upwelling and downwelling longwave radiation components were 0.5–1.5 K lower than estimates using only upwelling longwave radiation. Neglecting the reflected downwelling component of the longwave balance for

surface temperature (T_s) estimation leads to substantial bias in plot-scale LST estimation. The equation ignoring reflected longwave (used in literature) overestimates the sensitivity to emissivity meaning small error in emissivity can cause substantial discrepancies in land surface temperature (LST) estimation. When the downwelling longwave component is ignored, this can lead to significant inaccuracies in LST values. Conversely, adjusting the emissivity value slightly can artificially correct unrealistic LST measurements. The reduced sensitivity of emissivity by considering reflected longwave is advantageous for ecosystem-scale LST estimation since ecosystem-scale emissivity is usually unknown and, therefore, used as an approximate value. The correspondence between plot-scale LST and landscape-scale LST obtained using MODIS depends on site-specific characteristics, such as canopy density, sensor locations, and viewing angles. Ecosystem-scale LST retrieved using ϵ_{MODIS} values at sparse canopy shows a strong negative bias in comparison to MODIS LST due to a sizeable off-Nadir viewing angle, MODIS overpass would lead to an elongated footprint resulting in a different distribution of bare soil and vegetated areas compared to the mostly Nadir viewing angle of the tower-mounted sensor (due to their hemispherical footprint). The difference in footprint and viewing angles between the tower-mounted pyrometers and MODIS radiometers could also be the reason for the bias between the two LST estimates. The small-scale surface heterogeneity at the flux tower sites resulted in a footprint mismatch between the radiometer (measuring longwave) and the EC measurement (measuring H and LE), resulting in a bias in the upwelling longwave radiation. Due to this mismatch, the estimated surface temperature does not represent the H. To make the surface temperature values consistent with the measured H and to remove the intercept, the $T_s - T_a$ values were optimized, which resulted in a low value of ϵ to remove the low bias in LST. The intercept suggests a poor correspondence between observed H and estimated T_s due to footprint mismatch or the canopy's stratified structure, meaning the radiometer does not see all the leaves contributing to the sensible heat and hypothesizing that the intercept results from a footprint mismatch between the aerodynamic and radiometric measurements, minor correction in upwelling longwave (6-9%) removed the intercept. It produced realistic emissivity values and self-consistent monthly H vs ΔT plots.

Combining radiometric (longwave) and aerodynamic measurements (H) for estimating ecosystem-scale emissivity and LST also provides a quality check on the correspondence between observed fluxes and temperatures consistently at the ecosystem-scale. Thus fitting a model with an intercept is the more robust approach, and a significant intercept should be used as a red flag for the utility of the data for the estimation of plot-scale LST. The intercept value can be used as a consistency criterion for observed data (radiometric and aerodynamic measurements) before using them in combination, as a significant value of intercept indicates inconsistency between observed sensible heat flux and surface-to-air temperature difference. Therefore, the proposed method of fitting a linear relation with

an intercept to H and $T_s - T_a$ has the potential to provide more reliable benchmark data sets for model evaluation and validation at the ecosystem-scale (plot-scale). The plot-scale epsilon estimates could also be used to parameterize climate and weather prediction models at the ecosystem-scale, but this was not tested in the present study.

In Chapter 3, a ground-vegetation (two-source) model is used to simulate the footprint mismatch by varying the soil and vegetation surface seen by the radiometer and eddy-covariance tower. The model was used to investigate the impact of surface heterogeneity resulting in footprint mismatch and associated energy imbalance. The footprint mismatch between the radiometer meter and the EC measurement system resulted in a positive value of intercept. The underestimation of longwave measurements leads to a positive intercept, and the overestimation of the longwave measurements leads to a negative intercept. Surface heterogeneity has also been recognized as one of the potential causes for the lack of energy balance closure; however, quantifying the impact of surface heterogeneity is challenging due to the complex interactions between spatial heterogeneity and other processes (e.g., secondary eddies) at a flux tower site. In the formulated two-source model, the energy imbalance can only be introduced by implementing footprint mismatch, and we found that a small component of the resulting energy imbalance can be improved by correcting the bias in the upwelling longwave. Optimizing the emissivity in TSEB when simulating footprint mismatch conditions led to a lower emissivity value. The plot-scale emissivity estimation by combining radiometric and aerodynamic measurements fails when there is a footprint mismatch between the radiometer and the EC tower as emissivity compensates for the bias in R_{lup} by varying both ϵ_{opt} and c, which means one need to look for both quantify footprint mismatch. Hence, in the presence of footprint mismatch, constant ϵ derived from MODIS can be used. In the case of positive intercept (c), the value of c can be used to quantify the footprint mismatch and required correction in R_{lup} is applied, which compensates for the mismatch. In the next step, Bowen ratio closure can be applied to obtain a closed energy balance with a consistent H vs ΔT plot.

Following consistent H vs ΔT, in Chapter 4, ecosystem-scale benchmark resistance to heat and water exchange is estimated directly from the flux tower observation using the slope of H and $T_s - T_a$. The results showed that the monthly slope of daytime H vs ΔT regression could, on average, represent the site-specific variations in the total effective resistance to heat exchange. We found an exponential decrease in the heat exchange resistances with increasing measurement height. As the wind speed increases at a decreasing rate (log-law) it results in an exponential decay of aerodynamic resistance due to enhanced mixing. The estimated benchmark resistance was used to develop the concept of canopy-scale aerodynamic resistances to investigate and evaluate the controls of momentum, heat, and mass transfer from the leaf surface to the canopy air space and the atmosphere. A comprehensive comparison of observations derived using total

resistance with commonly used stability and roughness-based resistance formulations revealed that total benchmark resistance deduced from observed fluxes and temperatures was consistently better than the roughness length-based resistance parameterizations at most study sites. The difference in the two resistance value was removed by combining the leaf boundary layer resistances and aerodynamic canopy-atmosphere resistance. Based on these results, a canopy-scale aerodynamic resistance model was proposed by dividing the canopy into two components: the leaf boundary layer resistance (leaves at the canopy-top) and canopy-air-to-atmosphere resistance. By explicitly considering the effect of dominant leaf sizes and assuming a uniform distribution of the leaf area index within the canopy, the proposed leaf-canopy-air resistance model consistently captures the variations in estimated benchmark resistance. Estimating the canopy-air resistance by integrating the resistivity profile (derived from the eddy diffusivity theorem) enables better integration of the site-specific measured values (e.g., measurement height, canopy height). It allows for a more tailored estimation of the leaf-canopy resistance by integrating the site-specific data (air temperature, wind speed) and avoiding reliance solely on roughness length parameter values (estimated using the rule of thumb). The proposed ecosystem-scale aerodynamic resistance model enables a more consistent coupling between aerodynamic and physiological leaf-scale processes, such as photosynthesis and stomatal control, which depend on and interact with leaf temperature. All existing resistance formulations for neutral conditions underestimate the aerodynamic resistance estimate compared to the benchmark resistance, resulting in an overestimated T_s. The error in T_s is compensated by adding an extra resistance or a correction term, KB^{-1}, such that the observed $H + LE$ is reproduced. The proposed resistance accounted for the canopy structure using different integral length scales to represent the position of the height of the heat source within the canopy. In addition to this, a physically based representation of the proposed resistance provides an opportunity to investigate site-specific resistance values using canopy structural characteristics (heterogeneity due to trees, grasses, leaf shapes, sizes, and densities). The difference in the observed H and modelled H using canopy-scale aerodynamic resistance was consistently explainable by the difference in the benchmark and canopy-scale aerodynamic resistance across the sites with low intercept values. The intercept value shows the bias in estimated $T_s - T_a$, which also impacts the estimation of modelled H. The results showed that the proposed canopy-scale aerodynamic resistance represents the complex coupling of leaf-canopy-air resistance in a physically consistent manner.

5.2 Conclusions

To summarize the work presented in the thesis:

1. Combining radiometric and aerodynamic measurements to estimate ecosystem-

scale emissivity and surface temperature enables a comprehensive evaluation of the representativeness of measured turbulent fluxes of heat and water vapor relative to observed radiometric fluxes, which are also used to estimate surface temperature, as discussed in Chapter 2. The intercept value between the sensible heat flux (H) and the surface-to-air temperature difference ΔT is a consistency criterion for the observed data from radiometric and aerodynamic measurements before they are integrated. A significant intercept suggests a discrepancy in the representativeness between the radiometric and eddy-covariance footprints. This method involves fitting a linear relationship with an intercept to the observed H vs ΔT to estimate emissivity and surface temperature consistent with the observed fluxes, providing all necessary data at the ecosystem-scale for model validation.

2. A two-source surface energy balance model, which simulates vegetation and ground surface and has a footprint mismatch between the radiometer and eddy covariance tower, can lead to a positive intercept in H vs ΔT plots and energy imbalance, as shown in Chapter 3. Combining radiometric and aerodynamic measurements to estimate plot-scale emissivity in the presence of footprint mismatch is not ideal as in order to reduce the intercept between H and ΔT, the method reduces emissivity unrealistically and the resulting surface temperature is not representative of the average site temperature. Instead, landscape emissivity, such as MODIS-derived emissivity, is preferable in cases of a significant positive intercept between monthly H vs ΔT using MODIS emissivity, correcting the upwelling longwave radiation by a relative percentage to remove intercept in the best approach. This correction removes the intercept and slightly improves the energy balance closure. The energy imbalance due to surface heterogeneity cannot be corrected using conventional energy balance closure schemes, such as the Bowen ratio closure, but by correcting the radiometric measurements (net radiation).

3. The novel leaf-canopy-air resistance model proposed in Chapter 3 represents a significant advancement in estimating resistance values derived from eddy-covariance (EC) measurements. It significantly enhances the reproduction of benchmark resistance to heat exchange between the canopy and the atmosphere, thereby improving our understanding and prediction of canopy-atmosphere heat exchange processes. The model (r_{lca}) effectively couples the leaf boundary layer with specific observations such as fluxes, wind speed, and air temperature, consistently outperforming existing resistance models. Comparative analysis among existing parameterizations highlights that the resistance formulation by Verma et al. (Verma 1989) demonstrated superior performance overall. However, it overestimated surface resistance in needle forests while underestimating canopy-air resistance. Conversely, it underestimated surface resistance in broad-leaf forests while overestimating canopy-air resistance. The proposed canopy-air resistance model integrates resistivity between two heights, which enhances model parameterization by incorporating canopy structure considerations. For mixed canopies like savannas composed of long bushes

and trees, the lower integral lies predominantly within the canopy compared to homogeneous forests, resulting in a smoother surface with reduced resistance. Additionally, the lower limit of the integral closely approximates the canopy top. This integrated resistance model incorporates canopy-air interactions (canopy microclimate, canopy height) and leaf-canopy interactions (leaf length, leaf area index, air temperature, wind speed), enhancing its robustness in understanding site-specific processes governing vegetation-atmosphere interactions. The physically-based description of complex interactions between leaf surfaces and eddies within the model provides a more accurate estimation of aerodynamic resistance than existing empirical models. Its straightforward nature make it a valuable tool for estimating ecosystem-scale heat exchange processes and informed decision-making regarding the impact of land cover types on microclimate.

5.3 Future work

The methodology presented in this study demonstrates substantial potential for application across diverse ecosystem types, providing valuable insights into the underlying mechanisms governing ecosystem-scale energy partitioning. By combining radiometric and aerodynamic measurements (turbulent fluxes), the study enables precise quantification of surface emissivity, surface temperature, and surface energy balance. The integrated approach of analyzing flux tower measurements presented in this work advances the use of ecosystem-scale observations for process-based understanding. Future work can incorporate eddy-covariance (EC) measurements alongside considerations of anthropogenic heat contributions, allowing the methodology to be adapted for urban environments to estimate the surface energy balance. The proposed resistance formulation can be integrated with evapotranspiration models to assess whether improved parameterization of canopy-scale resistance leads to improved evapotranspiration predictions. Nevertheless, it is crucial to acknowledge that the aerodynamic theory, which forms the basis of the proposed canopy-air resistance model have limitations (constant U^*), particularly for low vegetation heights (croplands and grasslands). The flux tower measurement height for croplands and grasslands is approximately eight to ten times above the canopy height and the U^* measured at that height is not representative of the surface. Therefore, future research efforts should consider measurement of U^* more closer to the the surface for grasslands and croplands which can help in having a realistic resistivity profile and total resistance to heat exchange can be estimated with more confidence.

Epilogue

,

Vegetation is used as a carbon sink without thinking about its other link.
Under limited groundwater resources, vegetation can still be heat relief sources.

Vegetation is a potential solution to climate change, but its effective implementation needs more research exchange!
To beat the heat: vegetation height got all the limelight, is that alright?

What about the leaf size which we never hypothesize!
Leaves clatter: their size matter!
Devil is in the detail. Surface-to-air temperature difference can be the trail.

Surface heterogeneity causes temperature ambiguity, due to which the climate models lack clarity.
For the research to cohere, we need to connect all these here: Soil, vegetation, and the atmosphere.

Bibliography

Abdelghani, Chehbouni et al. (2008). "Using remotely sensed data to estimate area-averaged daily surface fluxes over a semi-arid mixed agricultural land". In: *agricultural and forest meteorology* 148.3, pp. 330–342.

Allen, Richard G et al. (1998). "Crop evapotranspiration-Guidelines for computing crop water requirements-FAO Irrigation and drainage paper 56". In: *Fao, Rome* 300.9, p. D05109.

Bahir, Malik et al. (2017). "Evaluation and aggregation properties of thermal infra-red-based evapotranspiration algorithms from 100 m to the km scale over a semi-arid irrigated agricultural area". In: *Remote Sensing* 9.11, p. 1178.

Baldocchi, Dennis et al. (2001). "FLUXNET: A new tool to study the temporal and spatial variability of ecosystem-scale carbon dioxide, water vapor, and energy flux densities". In: *Bulletin of the American Meteorological Society* 82.11, pp. 2415–2434.

Baldocchi, Dennis D., Beverly E. Law, and Peter M. Anthoni (May 2000). "On measuring and modeling energy fluxes above the floor of a homogeneous and heterogeneous conifer forest". en. In: *Agricultural and Forest Meteorology* 102.2-3, pp. 187–206. ISSN: 01681923. DOI: 10.1016/S0168-1923(00)00098-8. URL: https://linkinghub.elsevier.com/retrieve/pii/S0168192300000988.

Banerjee, Tirtha, Frederik De Roo, and Matthias Mauder (2017). "Explaining the convector effect in canopy turbulence by means of large-eddy simulation". In: *Hydrology and Earth System Sciences* 21.6, pp. 2987–3000.

Barr, AG et al. (2006). "Surface energy balance closure by the eddy-covariance method above three boreal forest stands and implications for the measurement of the CO2 flux". In: *Agricultural and Forest Meteorology* 140.1-4, pp. 322–337.

Bonan, Gordon B et al. (2021). "Moving beyond the incorrect but useful paradigm: reevaluating big-leaf and multilayer plant canopies to model biosphere-atmosphere fluxes–a review". In: *Agricultural and Forest Meteorology* 306, p. 108435.

Boulet, Gérard et al. (1999). "Mosaic versus dual source approaches for modelling the surface energy balance of a semi-arid land". In: *Hydrology and Earth System Sciences* 3.2, pp. 247–258.

Boulet, Gilles et al. (2012). "An empirical expression to relate aerodynamic and surface temperatures for use within single-source energy balance models". In: *Agricultural and Forest Meteorology* 161, pp. 148–155.

Buchan, Graeme D (2000). "Soil temperature regime". In: *Soil and Environmental Analysis*. CRC Press, pp. 551–606.

Busch, Niels E, Simon W Chang, and Richard A Anthes (1976). "A multi-level model of the planetary boundary layer suitable for use with mesoscale dynamic models". In: *Journal of Applied Meteorology and Climatology* 15.9, pp. 909–919.

Butterworth, Brian J et al. (2021). "Connecting land–atmosphere interactions to surface heterogeneity in CHEESEHEAD19". In: *Bulletin of the American Meteorological Society* 102.2, E421–E445.

Cahill, Anthony T., Marc B. Parlange, and John D. Albertson (Oct. 1997). "On the Brutsaert temperature roughness length model for sensible heat flux estimation". en. In: *Water Resources Research* 33.10, pp. 2315–2324. ISSN: 00431397. DOI: 10.1029/97WR01638. URL: http://doi.wiley.com/10.1029/97WR01638.

Chakraborty, TC et al. (2021). "On the land emissivity assumption and Landsat-derived surface urban heat islands: A global analysis". In: *Remote Sensing of Environment* 265, p. 112682.

Chakraborty, Tirthankar et al. (2019). "Biases in model-simulated surface energy fluxes during the Indian monsoon onset period". In: *Boundary-Layer Meteorology* 170.2, pp. 323–348.

Chamberlain, AC (1968). "Transport of gases to and from surfaces with bluff and wave-like roughness elements". In: *Quarterly Journal of the Royal Meteorological Society* 94.401, pp. 318–332.

Chen, Chiachung (2015). "Determining the leaf emissivity of three crops by infrared thermometry". In: *Sensors* 15.5, pp. 11387–11401.

Choudhury, B J and JL Monteith (1988). "A four-layer model for the heat budget of homogeneous land surfaces". In: *Quarterly Journal of the Royal Meteorological Society* 114.480, pp. 373–398.

Choudhury, BJ, RJ Reginato, and SB Idso (1986a). "An analysis of infrared temperature observations over wheat and calculation of latent heat flux". In: *Agricultural and Forest Meteorology* 37.1, pp. 75–88.

Choudhury, B.J., R.J. Reginato, and S.B. Idso (May 1986b). "An analysis of infrared temperature observations over wheat and calculation of latent heat flux". en. In: *Agricultural and Forest Meteorology* 37.1, pp. 75–88. ISSN: 01681923. DOI: 10.1016/0168-1923(86)90029-8. URL: https://linkinghub.elsevier.com/retrieve/pii/0168192386900298.

Chu, Housen et al. (2018). “Temporal dynamics of aerodynamic canopy height derived from eddy covariance momentum flux data across North American flux networks”. In: *Geophysical research letters* 45.17, pp. 9275–9287.

Chu, Housen et al. (2021). “Representativeness of Eddy-Covariance flux footprints for areas surrounding AmeriFlux sites”. In: *Agricultural and Forest Meteorology* 301, p. 108350.

Colaizzi, Paul D et al. (2004). “Comparison of aerodynamic and radiometric surface temperature using precision weighing lysimeters”. In: *Remote sensing and modeling of ecosystems for sustainability*. Vol. 5544. SPIE, pp. 215–229.

Corbari, CHIARA et al. (2010). “Land surface temperature representativeness in a heterogeneous area through a distributed energy-water balance model and remote sensing data”. In: *Hydrology and Earth System Sciences* 14.10, pp. 2141–2151.

Cowan, IR (1968). “Mass, heat and momentum exchange between stands of plants and their atmospheric environment”. In: *Quarterly Journal of the Royal Meteorological Society* 94.402, pp. 523–544.

Crago, Richard D and Russell J Qualls (2014). “Use of land surface temperature to estimate surface energy fluxes: Contributions of Wilfried Brutsaert and collaborators”. In: *Water Resources Research* 50.4, pp. 3396–3408.

Cullen, Nicolas J et al. (2007). “Energy-balance model validation on the top of Kilimanjaro, Tanzania, using eddy covariance data”. In: *Annals of Glaciology* 46, pp. 227–233.

Cuxart, J and AA Boone (2020). “Evapotranspiration over land from a boundary-layer meteorology perspective”. In: *Boundary-Layer Meteorology* 177.2, pp. 427–459.

Delucchi, L (2014). “pyModis: from satellite to GIS maps”. In: *FOSS4G 2014*.

Denmead, OT and EF Bradley (1985). “Flux-gradient relationships in a forest canopy”. In: *The Forest-Atmosphere Interaction: Proceedings of the Forest Environmental Measurements Conference held at Oak Ridge, Tennessee, October 23–28, 1983*. Springer, pp. 421–442.

Ehret, Uwe et al. (2012). “HESS Opinions" Should we apply bias correction to global and regional climate model data?"”. In: *Hydrology and Earth System Sciences* 16.9, pp. 3391–3404.

Eisenhauer, Joseph G (2003). “Regression through the origin”. In: *Teaching statistics* 25.3, pp. 76–80.

Foken, Thomas (2008). “The energy balance closure problem: an overview”. In: *Ecological Applications* 18.6, pp. 1351–1367.

Gilberto, Pastorello et al. (2020). “The FLUXNET2015 dataset and the ONEFlux processing pipeline for eddy covariance data”. In: *Scientific Data* 1.

Göckede, Mathias, Corinna Rebmann, and Thomas Foken (2004). “A combination of quality assessment tools for eddy covariance measurements with footprint modelling

for the characterisation of complex sites". In: *Agricultural and Forest Meteorology* 127.3-4, pp. 175–188.

Guillevic, P et al. (2003). "Thermal infrared radiative transfer within three-dimensional vegetation covers". In: *Journal of Geophysical Research: Atmospheres* 108.D8.

Guillevic, P et al. (2018). "Land surface temperature product validation best practice protocol. Version 1.1". In: *Best Practice for Satellite-Derived Land Product Validation*, p. 60.

Hoffmann, H et al. (2016). "<? xmltex\vspace* 5mm?> Estimating evaporation with thermal UAV data<? xmltex\newline?> and two-source energy balance models". In: *Hydrology and Earth System Sciences* 20.2, pp. 697–713.

Holmes, Thomas RH et al. (2016). "Cloud tolerance of remote-sensing technologies to measure land surface temperature". In: *Hydrology and Earth System Sciences* 20.8, pp. 3263–3275.

Holmes, TRH et al. (2009). "Land surface temperature from Ka band (37 GHz) passive microwave observations". In: *Journal of Geophysical Research: Atmospheres* 114.D4.

Hulley, Glynn C, Christopher G Hughes, and Simon J Hook (2012). "Quantifying uncertainties in land surface temperature and emissivity retrievals from ASTER and MODIS thermal infrared data". In: *Journal of Geophysical Research: Atmospheres* 117.D23.

Incropera, Frank P et al. (1996). *Fundamentals of heat and mass transfer*. Vol. 6. Wiley New York.

Inoue, Eiichi (1963). "On the turbulent structure of airflow within". In: *Journal of the Meteorological Society of Japan. Ser. II* 41.6, pp. 317–326.

Jacob, D et al. (2001). "A comprehensive model inter-comparison study investigating the water budget during the BALTEX-PIDCAP period". In: *Meteorology and Atmospheric Physics* 77.1-4, pp. 19–43.

Jiménez Cisneros, Blanca E et al. (2014). "Freshwater resources". In.

Jin, Menglin and Shunlin Liang (2006). "An improved land surface emissivity parameter for land surface models using global remote sensing observations". In: *Journal of Climate* 19.12, pp. 2867–2881.

Kent, Christoph W et al. (2018). "Assessing methods to extrapolate the vertical wind-speed profile from surface observations in a city centre during strong winds". In: *Journal of Wind Engineering and Industrial Aerodynamics* 173, pp. 100–111.

Kidston, Joe et al. (2010). "Energy balance closure using eddy covariance above two different land surfaces and implications for CO 2 flux measurements". In: *Boundary-Layer Meteorology* 136, pp. 193–218.

Knauer, Jürgen et al. (2018). "Bigleaf—An R package for the calculation of physical and physiological ecosystem properties from eddy covariance data". In: *PloS one* 13.8, e0201114.

Kustas, William and Martha Anderson (2009). "Advances in thermal infrared remote sensing for land surface modeling". In: *Agricultural and Forest Meteorology* 149.12, pp. 2071–2081.

Kustas, William P et al. (2007). "Utility of radiometric–aerodynamic temperature relations for heat flux estimation". In: *Boundary-Layer Meteorology* 122.1, pp. 167–187.

Kustas, William P. et al. (Oct. 2016). "Revisiting the paper "Using radiometric surface temperature for surface energy flux estimation in Mediterranean drylands from a two-source perspective"". en. In: *Remote Sensing of Environment* 184, pp. 645–653. ISSN: 00344257. DOI: 10.1016/j.rse.2016.07.024. URL: https://linkinghub.elsevier.com/retrieve/pii/S0034425716302814.

Landsberg, JJ and AS Thom (1971). "Aerodynamic properties of a plant of complex structure". In: *Quarterly Journal of the Royal Meteorological Society* 97.414, pp. 565–570.

Lettau, H_ (1969). "Note on aerodynamic roughness-parameter estimation on the basis of roughness-element description". In: *Journal of Applied Meteorology (1962-1982)* 8.5, pp. 828–832.

Lhomme, Jean-Paul (1991). "The concept of canopy resistance: historical survey and comparison of different approaches". In: *Agricultural and forest meteorology* 54.2-4, pp. 227–240.

Lhomme, Jean-Paul, Nader Katerji, and JM Bertolini (1992). "Estimating sensible heat flux from radiometric temperature over crop canopy". In: *Boundary-layer meteorology* 61.3, pp. 287–300.

Lhomme, Jean-Paul et al. (1988). "Radiative surface temperature and convective flux calculation over crop canopies". In: *Boundary-Layer Meteorology* 43.4, pp. 383–392.

Liu, S, D Mao, and L Lu (2006). "Measurement and estimation of the aerodynamic resistance". In: *Hydrology and Earth System Sciences Discussions* 3.3, pp. 681–705.

Liu, Xiaoyin et al. (2020). "Modeling rice evapotranspiration under water-saving irrigation condition: Improved canopy-resistance-based". In: *Journal of Hydrology* 590, p. 125435.

Lu, Li et al. (2009). "The characteristics and parameterization of aerodynamic roughness length over heterogeneous surfaces". In: *Advances in atmospheric sciences* 26, pp. 180–190.

Maes, Wouter H et al. (2019). "Potential evaporation at eddy-covariance sites across the globe". In: *Hydrology and Earth System Sciences* 23.2, pp. 925–948.

Mahrt, L (1996). *The bulk aerodynamic formulation over heterogeneous surfaces.*

Mallick, Kaniska et al. (2013). "Latent heat flux and canopy conductance based on Penman–Monteith, Priestley–Taylor Equation, and Bouchet's complementary hypothesis". In: *Journal of Hydrometeorology* 14.2, pp. 419–442.

Mallick, Kaniska et al. (2015). "Reintroducing radiometric surface temperature into the P enman-M onteith formulation". In: *Water Resources Research* 51.8, pp. 6214–6243.

Mallick, Kaniska et al. (2016). "Canopy-scale biophysical controls of transpiration and evaporation in the Amazon Basin". In: *Hydrology and Earth System Sciences* 20.10, pp. 4237–4264.

Mallick, Kaniska et al. (2018a). "A critical evaluation on the role of aerodynamic and canopy–surface conductance parameterization in SEB and SVAT models for simulating evapotranspiration: A case study in the upper biebrza national park wetland in poland". In: *Water* 10.12, p. 1753.

Mallick, Kaniska et al. (2018b). "Bridging Thermal Infrared Sensing and Physically-Based Evapotranspiration Modeling: From Theoretical Implementation to Validation Across an Aridity Gradient in Australian Ecosystems". In: *Water Resources Research* 54.5, pp. 3409–3435.

Marcolla, B and A Cescatti (2018). "Geometry of the hemispherical radiometric footprint over plant canopies". In: *Theoretical and Applied Climatology* 134.3, pp. 981–990.

Margulis, Steven A, Yufei Liu, and Elisabeth Baldo (2019). "A joint Landsat-and MODIS-based reanalysis approach for midlatitude montane seasonal snow characterization". In: *Frontiers in Earth Science*, p. 272.

Masseroni, Daniele, Chiara Corbari, and Marco Mancini (2014). "Limitations and improvements of the energy balance closure with reference to experimental data measured over a maize field". In: *Atmósfera* 27.4, pp. 335–352.

Mauder, Matthias, Thomas Foken, and Joan Cuxart (2020). "Surface-energy-balance closure over land: a review". In: *Boundary-Layer Meteorology* 177, pp. 395–426.

McNaughton, KG and PG Jarvis (1983). "Predicting effects of vegetation changes on transpiration and evaporation". In: *Water deficits and plant growth* 7, pp. 1–47.

Meier, Ronny et al. (2022). "Impacts of a revised surface roughness parameterization in the Community Land Model 5.1". In: *Geoscientific Model Development* 15.6, pp. 2365–2393.

Migliavacca, Mirco et al. (2021). "The three major axes of terrestrial ecosystem function". In: *Nature*, pp. 1–5.

Mira, M et al. (2007). "Influence of soil water content on the thermal infrared emissivity of bare soils: Implication for land surface temperature determination". In: *Journal of Geophysical Research: Earth Surface* 112.F4.

Montanari, Alberto et al. (2013). ""Panta Rhei—everything flows": change in hydrology and society—the IAHS scientific decade 2013–2022". In: *Hydrological Sciences Journal* 58.6, pp. 1256–1275.

Monteith, John L (1965). "Evaporation and environment". In: *Symposia of the society for experimental biology*. Vol. 19. Cambridge University Press (CUP) Cambridge, pp. 205–234.

Morillas, Laura et al. (2013). "Using radiometric surface temperature for surface energy flux estimation in Mediterranean drylands from a two-source perspective". In: *Remote Sensing of Environment* 136, pp. 234–246.

Norman, John M and Francois Becker (1995). "Terminology in thermal infrared remote sensing of natural surfaces". In: *Agricultural and Forest Meteorology* 77.3-4, pp. 153–166.

Norman, John M, William P Kustas, and Karen S Humes (1995). "Source approach for estimating soil and vegetation energy fluxes in observations of directional radiometric surface temperature". In: *Agricultural and Forest Meteorology* 77.3-4, pp. 263–293.

Owen, P R and WR Thomson (1963). "Heat transfer across rough surfaces". In: *Journal of Fluid Mechanics* 15.3, pp. 321–334.

Penman, HL and IF Long (1960). "Weather in wheat: An essay in micro-meteorology". In: *Quarterly Journal of the Royal Meteorological Society* 86.367, pp. 16–50.

Raupach, M R_ and JJ Finnigan (1988). "'Single-layer models of evaporation from plant canopies are incorrect but useful, whereas multilayer models are correct but useless': discuss". In: *Australian Journal of Plant Physiology (Australia)*.

Raupach, MR (1994). "Simplified expressions for vegetation roughness length and zero-plane displacement as functions of canopy height and area index". In: *Boundary-layer meteorology* 71.1, pp. 211–216.

Raupach, MR and JJ Finnigan (1995). "Scale issues in boundary-layer meteorology: Surface energy balances in heterogeneous terrain". In: *Hydrological Processes* 9.5-6, pp. 589–612.

Rigden, Angela, Dan Li, and Guido Salvucci (Feb. 2018a). "Dependence of thermal roughness length on friction velocity across land cover types: A synthesis analysis using AmeriFlux data". en. In: *Agricultural and Forest Meteorology* 249, pp. 512–519. ISSN: 01681923. DOI: 10.1016/j.agrformet.2017.06.003. URL: https://linkinghub.elsevier.com/retrieve/pii/S0168192317302022.

— (2018b). "Dependence of thermal roughness length on friction velocity across land cover types: A synthesis analysis using AmeriFlux data". In: *Agricultural and Forest Meteorology* 249, pp. 512–519.

Rosolem, Rafael et al. (2012). "A fully multiple-criteria implementation of the Sobol' method for parameter sensitivity analysis". In: *Journal of Geophysical Research: Atmospheres* 117.D7.

Rotenberg, Eyal and Dan Yakir (2010). "Contribution of semi-arid forests to the climate system". In: *Science* 327.5964, pp. 451–454.

— (Apr. 2011). "Distinct patterns of changes in surface energy budget associated with forestation in the semiarid region: DISTINCT PATTERNS OF CHANGES IN SURFACE ENERGY BUDGET". en. In: *Global Change Biology* 17.4, pp. 1536–1548.

ISSN: 13541013. DOI: 10.1111/j.1365-2486.2010.02320.x. URL: https://onlinelibrary.wiley.com/doi/10.1111/j.1365-2486.2010.02320.x.

Rowell, David P (2005). "A scenario of European climate change for the late twenty-first century: seasonal means and interannual variability". In: *Climate Dynamics* 25.7-8, pp. 837–849.

Saltelli, Andrea et al. (2017). "A new sample-based algorithms to compute the total sensitivity index". In: *arXiv preprint arXiv:1703.05799*.

Sánchez, JM et al. (2008). "Modelling surface energy fluxes over maize using a two-source patch model and radiometric soil and canopy temperature observations". In: *Remote sensing of Environment* 112.3, pp. 1130–1143.

Schmid, Hans Peter (2002). "Footprint modeling for vegetation atmosphere exchange studies: a review and perspective". In: *Agricultural and Forest Meteorology* 113.1-4, pp. 159–183.

Schmid, HP (1994). "Source areas for scalars and scalar fluxes". In: *Boundary-Layer Meteorology* 67.3, pp. 293–318.

Schuepp, PH (1993). "Tansley review No. 59. Leaf boundary layers". In: *New Phytologist*, pp. 477–507.

Schymanski, Stanislaus J and Dani Or (2017). "Leaf-scale experiments reveal an important omission in the Penman–Monteith equation". In: *Hydrology and Earth System Sciences* 21.2, pp. 685–706.

Schymanski, Stanislaus J, Dani Or, and Maciej Zwieniecki (2013). "Stomatal control and leaf thermal and hydraulic capacitances under rapid environmental fluctuations". In: *PloS one* 8.1, e54231.

Sellers, PJ et al. (1996). "A revised land surface parameterization (SiB2) for atmospheric GCMs. Part I: Model formulation". In: *Journal of climate* 9.4, pp. 676–705.

Shaver, Gaius R et al. (2000). "Global Warming and Terrestrial Ecosystems: A Conceptual Framework for Analysis: Ecosystem responses to global warming will be complex and varied. Ecosystem warming experiments hold great potential for providing insights on ways terrestrial ecosystems will respond to upcoming decades of climate change. Documentation of initial conditions provides the context for understanding and predicting ecosystem responses." In: *Bioscience* 50.10, pp. 871–882.

Shaw, Roger H and AR Pereira (1982). "Aerodynamic roughness of a plant canopy: a numerical experiment". In: *Agricultural Meteorology* 26.1, pp. 51–65.

Shuttleworth, W James and JS Wallace (1985). "Evaporation from sparse crops-an energy combination theory". In: *Quarterly Journal of the Royal Meteorological Society* 111.469, pp. 839–855.

Snyder, William C et al. (1998). "Classification-based emissivity for land surface temperature measurement from space". In: *International Journal of Remote Sensing* 19.14, pp. 2753–2774.

Sprintsin, Michael et al. (2012). "Evaluation of leaf-to-canopy upscaling methodologies against carbon flux data in North America". In: *Journal of Geophysical Research: Biogeosciences* 117.G1.

Stephens, Graeme L (1995). "Review of atmospheric radiation: 1991–1994". In: *Reviews of Geophysics* 33.S2, pp. 785–794.

Still, Christopher J et al. (2021). "Imaging canopy temperature: shedding (thermal) light on ecosystem processes". In: *New Phytologist* 230.5, pp. 1746–1753.

Stoy, Paul C et al. (2013). "A data-driven analysis of energy balance closure across FLUXNET research sites: The role of landscape scale heterogeneity". In: *Agricultural and forest meteorology* 171, pp. 137–152.

Su, Zhongbo (2002). "The Surface Energy Balance System (SEBS) for estimation of turbulent heat fluxes". In: *Hydrology and earth system sciences* 6.1, pp. 85–100.

Subin, Zachary M, William J Riley, and Dmitrii Mironov (2012). "An improved lake model for climate simulations: Model structure, evaluation, and sensitivity analyses in CESM1". In: *Journal of Advances in Modeling Earth Systems* 4.1.

Sugita, Michiaki and Wilfried Brutsaert (1996). "Optimal measurement strategy for surface temperature to determine sensible heat flux from anisothermal vegetation". In: *Water resources research* 32.7, pp. 2129–2134.

Sun, Jielun and Lawrence Mahrt (1995). "Relationship of surface heat flux to microscale temperature variations: Application to BOREAS". In: *Boundary-Layer Meteorology* 76.3, pp. 291–301.

Tanner, CB and M Fuchs (1968). "Evaporation from unsaturated surfaces: a generalized combination method". In: *Journal of Geophysical Research* 73.4, pp. 1299–1304.

Thakur, Gitanjali et al. (2022). "Downwelling longwave radiation and sensible heat flux observations are critical for surface temperature and emissivity estimation from flux tower data". In: *Scientific reports* 12.1, pp. 1–14.

Thom, AS et al. (1975). "Comparison of aerodynamic and energy budget estimates of fluxes over a pine forest". In: *Quarterly Journal of the Royal Meteorological Society* 101.427, pp. 93–105.

Thom, AS 1972 (1972). "Momentum, mass and heat exchange of vegetation". In: *Quarterly Journal of the Royal Meteorological Society* 98.415, pp. 124–134.

Timmermans, Wim J et al. (2007). "An intercomparison of the surface energy balance algorithm for land (SEBAL) and the two-source energy balance (TSEB) modeling schemes". In: *Remote Sensing of Environment* 108.4, pp. 369–384.

Trebs, Ivonne et al. (2021a). "The role of aerodynamic resistance in thermal remote sensing-based evapotranspiration models". In: *Remote Sensing of Environment* 264, p. 112602.

Trebs, Ivonne et al. (Oct. 2021b). "The role of aerodynamic resistance in thermal remote sensing-based evapotranspiration models". en. In: *Remote Sensing of Environment*

264, p. 112602. ISSN: 00344257. DOI: 10.1016/j.rse.2021.112602. URL: https://linkinghub.elsevier.com/retrieve/pii/S0034425721003229.

Trenberth, Kevin E and John T Fasullo (2012). "Tracking Earth's energy: From El Niño to global warming". In: *Surveys in geophysics* 33.3-4, pp. 413–426.

Troufleau, D et al. (1997). "Sensible heat flux and radiometric surface temperature over sparse Sahelian vegetation. I. An experimental analysis of the kB- 1 parameter". In: *Journal of Hydrology* 188, pp. 815–838.

Twine, Tracy E et al. (2000). "Correcting eddy-covariance flux underestimates over a grassland". In: *Agricultural and forest meteorology* 103.3, pp. 279–300.

Valayamkunnath, Prasanth et al. (2018). "Intercomparison of surface energy fluxes, soil moisture, and evapotranspiration from eddy covariance, large-aperture scintillometer, and modeling across three ecosystems in a semiarid climate". In: *Agricultural and Forest Meteorology* 248, pp. 22–47.

Verma, Manish et al. (2016). "Global surface net-radiation at 5 km from MODIS Terra". In: *Remote Sensing* 8.9, p. 739.

Verma, SB (1989). "Aerodynamic resistances to transfers of heat, mass and momentum". In.

Verma, Shashi B, Joon Kim, and Robert J Clement (1989). "Carbon dioxide, water vapor and sensible heat fluxes over a tallgrass prairie". In: *Boundary-Layer Meteorology* 46, pp. 53–67.

Vishnevetsky, Irina et al. (2019). "Method for accurate measurement of infrared emissivity for opaque low-reflectance materials". In: *Applied optics* 58.17, pp. 4599–4609.

Voogt, J. A. and C. S. B. Grimmond (Oct. 2000). "Modeling Surface Sensible Heat Flux Using Surface Radiative Temperatures in a Simple Urban Area". en. In: *Journal of Applied Meteorology* 39.10, pp. 1679–1699. ISSN: 1520-0450, 0894-8763. DOI: 10.1175/1520-0450-39.10.1679. URL: https://journals.ametsoc.org/doi/10.1175/JCLI-D-17-0352.1.

Voogt, J. A. and T. R. Oke (Sept. 1997). "Complete Urban Surface Temperatures". en. In: *Journal of Applied Meteorology* 36.9, pp. 1117–1132. ISSN: 0894-8763, 1520-0450. DOI: 10.1175/1520-0450(1997)036<1117:CUST>2.0.CO;2. URL: http://journals.ametsoc.org/doi/10.1175/1520-0450(1997)036<1117:CUST>2.0.CO;2.

Wan, Zhengming (2007). "Collection-5 MODIS land surface temperature products users' guide". In: *ICESS, University of California, Santa Barbara*.

Wang, Kaicun and Robert E Dickinson (2013). "Global atmospheric downward longwave radiation at the surface from ground-based observations, satellite retrievals, and reanalyses". In: *Reviews of Geophysics* 51.2, pp. 150–185.

Wang, Kaicun and Shunlin Liang (2009). "Evaluation of ASTER and MODIS land surface temperature and emissivity products using long-term surface longwave radiation ob-

servations at SURFRAD sites". In: *Remote Sensing of Environment* 113.7, pp. 1556–1565.

Wang, Wenhui, Shunlin Liang, and Tilden Meyers (2008). "Validating MODIS land surface temperature products using long-term nighttime ground measurements". In: *Remote Sensing of Environment* 112.3, pp. 623–635.

Wilson, Kell et al. (2002). "Energy balance closure at FLUXNET sites". In: *Agricultural and Forest Meteorology* 113.1-4, pp. 223–243.

Wohlfahrt, Georg, Katja Klumpp, and Jean-François Soussana (2011). "Eddy covariance measurements over grasslands". In: *Eddy covariance: a practical guide to measurement and data analysis*. Springer, pp. 333–344.

Wohlfahrt, Georg and Erich Tasser (2015). "A mobile system for quantifying the spatial variability of the surface energy balance: design and application". In: *International Journal of Biometeorology* 59, pp. 617–627.

Wohlfahrt, Georg et al. (2009). "On the consequences of the energy imbalance for calculating surface conductance to water vapour". In: *Agricultural and forest meteorology* 149.9, pp. 1556–1559.

Yang, Rongqian and Mark A Friedl (2003). "Determination of roughness lengths for heat and momentum over boreal forests". In: *Boundary-Layer Meteorology* 107.3, pp. 581–603.

Young, Adam M et al. (2021). "Seasonality in aerodynamic resistance across a range of North American ecosystems". In: *Agricultural and Forest Meteorology* 310, p. 108613.

Appendix A

Supplementary information for chapter 2

A.1 Comparison table of plot-scale LST with landscape LST using landscape and plot-scale ϵ

Table A.1: Comparison of plot-scale LST with landscape-scale daytime LST (MODIS, MODA001) at TERRA daily time of pass. Plot scale LST is obtained using landscape-scale emissivity (MODIS ϵ) (left column) and plot-scale emissivity obtained considering no intercept in H and ΔT (Optimum ϵ) at study sites. The reported plot-scale emissivity are median values and landscape emissivity are using channel 31 and 32 of MODA001 dataset. Bias is defined as mean of $T_s - T_{MODIS}$, R^2 is coefficient of determination between plot-scale LST in comparison to landscape-scale LST. The site acronyms can be found in **Table 2** of Chapter 2.

Sites	Landscape-scale ϵ					Plot-scale ϵ					
	ϵ	seq		leq		seq			leq		
		R^2	bias	R^2	bias	opt ϵ	R^2	bias	opt ϵ	R^2	bias
SP	0.974	0.80	-3.67	0.81	-4.61	0.96	0.81	-3.0	0.85	0.82	-1.91
AS	0.974	0.93	-4.78	0.93	-6.31	0.96	0.93	-3.4	0.82	0.93	-1.92
TT	0.974	0.55	-6.76	0.57	-8.30	0.95	0.58	-5.06	0.80	0.52	-4.02
HS	0.985	0.16	-8.89	0.16	-9.90	0.92	0.21	-4.78	0.6	0.22	-2.47
LF	0.985	0.40	-10.0	0.41	-11.0	0.92	0.40	-4.41	0.6	0.41	-2.57
AR	0.985	0.18	-2.61	0.27	-3.51	0.997	0.23	-2.93	0.96	0.252	-2.98
DU	0.985	0.80	-3.67	0.81	-4.61	0.99	0.428	-3.682	0.985	0.425	-3.926
TUM	0.983	0.82	-2.27	0.84	-2.10	0.99	0.89	0.99	0.97	0.89	1.93
BR	0.983	0.937	0.525	0.937	-0.195	0.98	0.917	1.87	0.82	0.895	2.72
YA	0.974	0.855	-2.081	0.855	-3.45	0.97	0.522	-4.517	0.93	0.793	-0.582

A.2 Emissivity estimation at Howard Springs and negative $T_s - T_a$

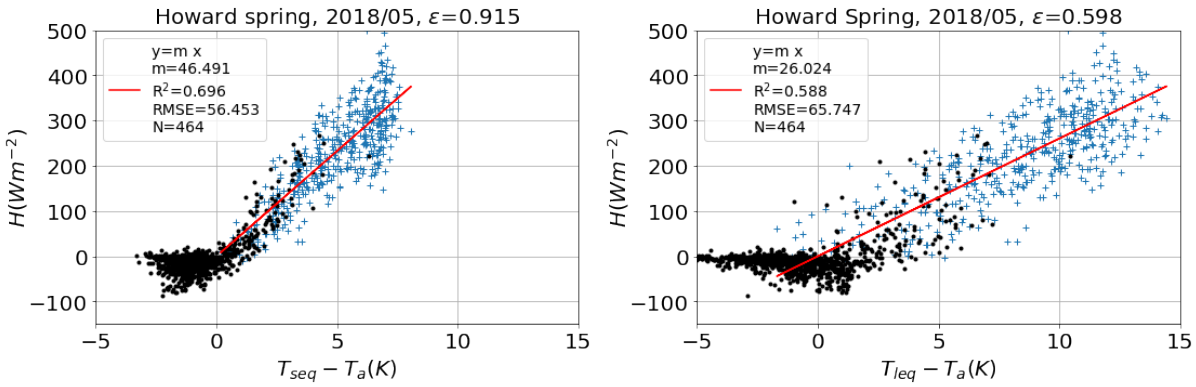

(a) (b)

Figure A.1: Monthly daytime ($R_n > 25\ W\ m^{-2}$) H and ΔT regression plots at HS using short (Eq. 2.7) and long equation. The value of optimised emissivity along with the year and month are shown on top of the plot.

A.3 T_s sensitivity to emissivity at Alice Spring and Tumbarumba

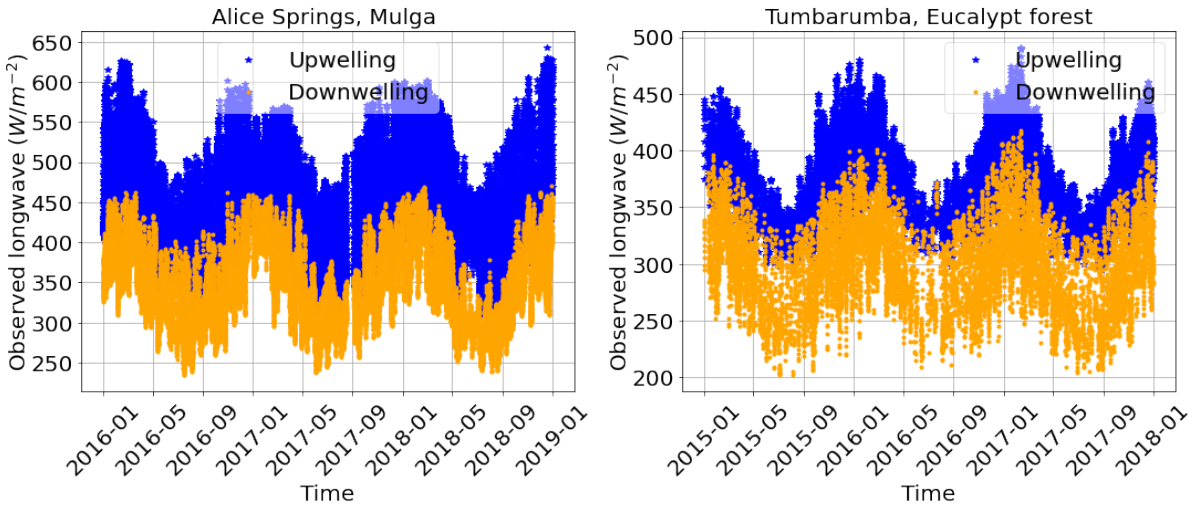

(a) (b)

Figure A.2: Timeseries of up-welling and down-welling longwave at sites having different land cover. (a) AS, a mulga site. (b) TUM, wet eucalypt forest

A.4 Variation of RMSE for monthly of $H(\Delta T)$ plot with surface emissivity

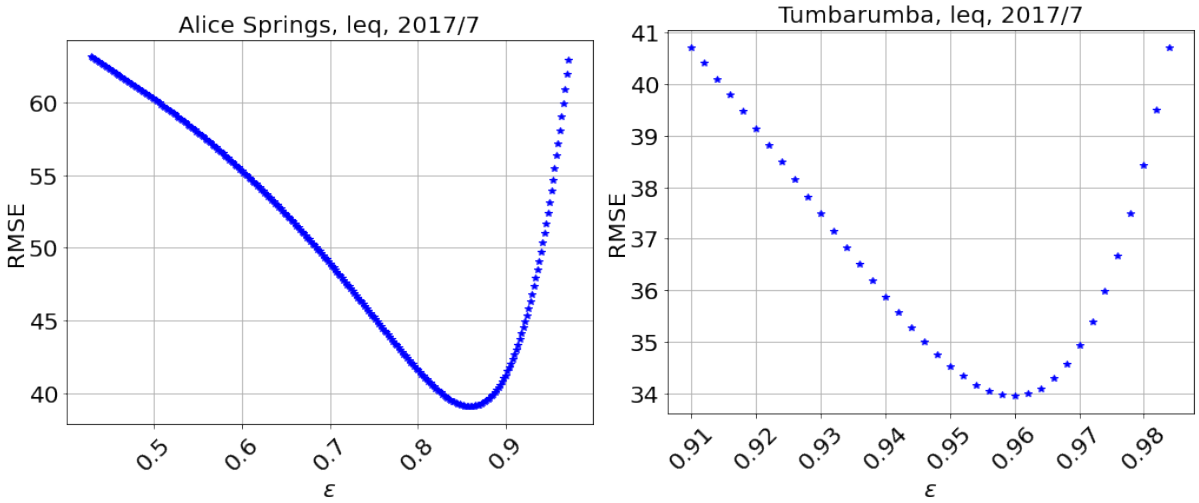

(a) (b)

Figure A.3: The RMSE and emissivity for $H(\Delta T)$ linear fit using long equation (a) AS (b) TUM

A.5 Sensitivity of short and long equation to surface emissivity

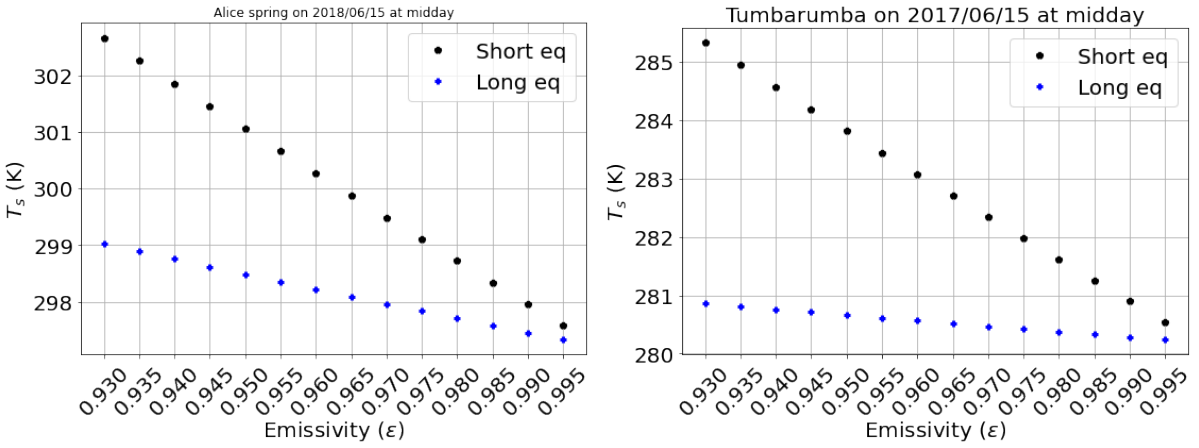

(a) (b)

Figure A.4: Sensitivity of LST estimated using two equations to the range of Broadband emissivity. The black dots and blue stars depicts LST using short (Eq. 2.7) and long (**Eq. 12** of Chapter 2). Midday longwave measurement for 15th June, 2016 at AS and TUM is used.

A.6 Energy imbalance closure reduces the correction in measured the up-welling longwave at Howard Springs

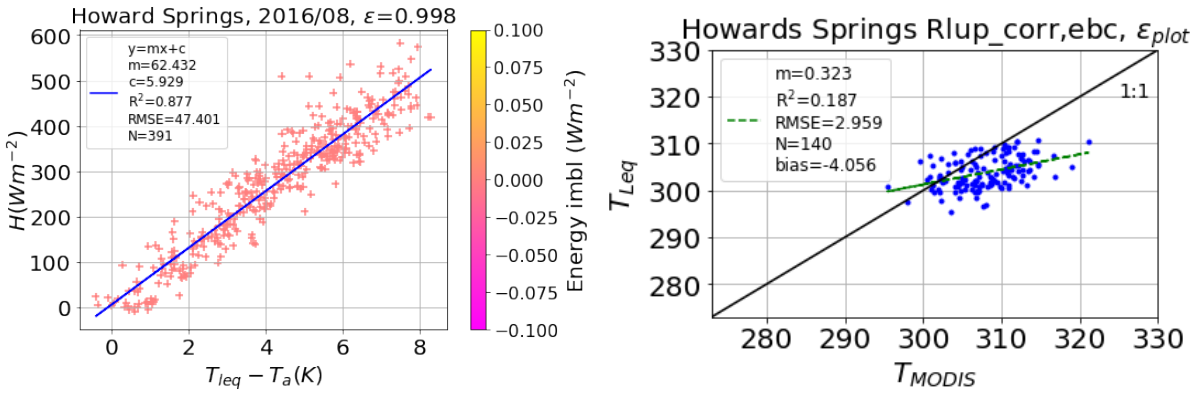

(a) (b)

Figure A.5: (a) Sensible heat flux as a function of surface-to-air temperature difference based on Eq. 2.10 of Chapter 2. Same analysis and legends as in **Fig 4c** of main Chapter 2, but after adding 35 ($W\ m^{-2}$) to measured R_{lup} and closing the energy balance using a Bowen ratio closure scheme. (b) Comparison of surface temperatures from (a) with landscape scale LST from MODIS.

A.7 SOBOL based uncertainity in epsilon and LST using long equation with accepting intercept in $H(\Delta T)$ and without intercept in $H(\Delta T)$

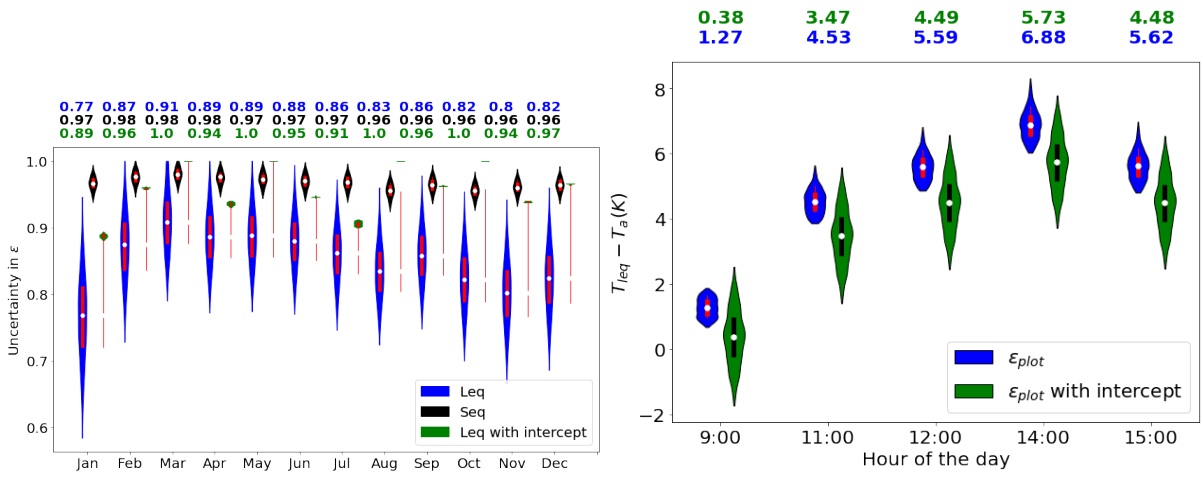

(a) (b)

Figure A.6: (a) Uncertainty in plot-scale ϵ using the short equation and long equation (with and without intercept in H and ΔT plots). (b) Uncertainty in hourly ΔT using long equation with and without intercept for July 15.

Appendix B

Supplementary information for chapter 3

B.1 Figure 2 replication with ϵ_{rad}

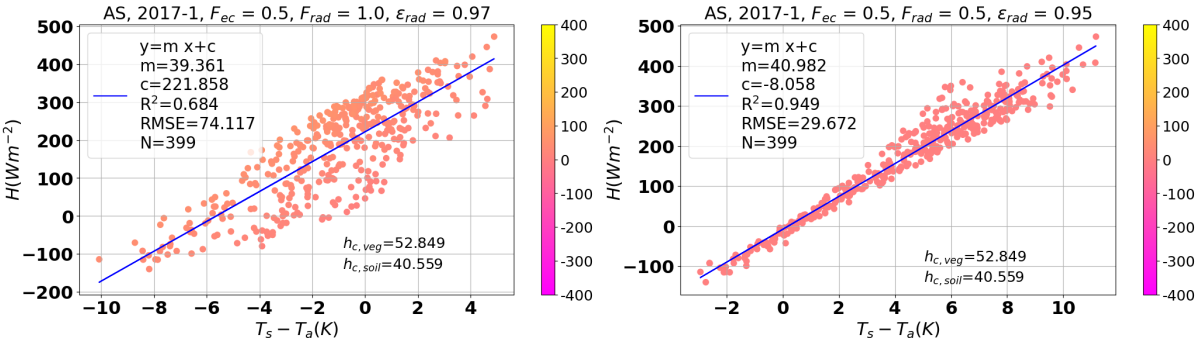

(a) (b)

Figure B.3: Two source model result for AS(2017/07)

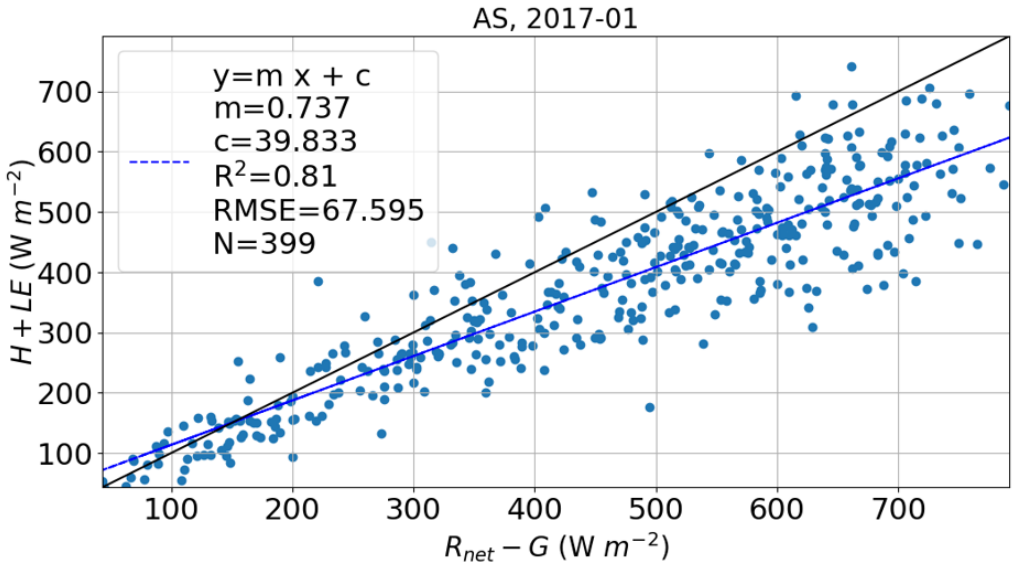

Figure B.1: Energy imbalance regression for AS 2017/01

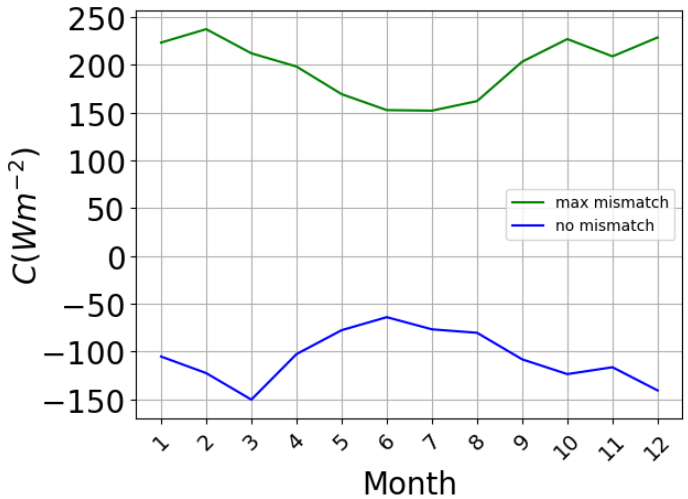

Figure B.2: TSEB to simulated the value of maximun and minium intercept for each month at AS for 2017

B.2 Observed monthly intercept at study sites

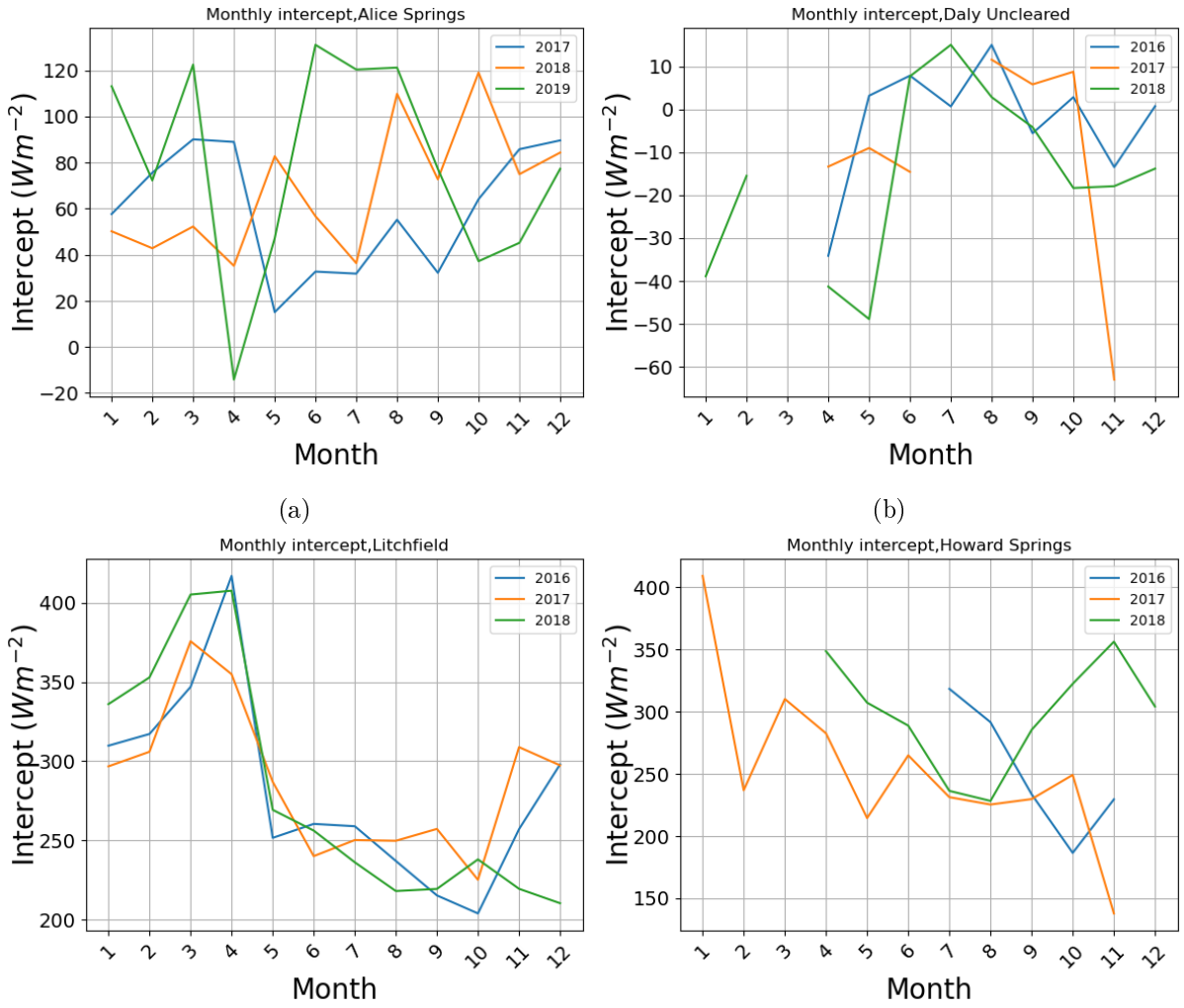

Figure B.4: Observed intercept at HS and LF

Explaining footprint mismatch with ϵ and c

The monthly value of c (H vs. ΔT) and estimated ϵ_{opt} is plotted for an year at AS using observation and TSEB simulating maximum and minimum mismatch condition as shown in Fig. B.5a,b.The monthly seasonality of c is also plotted using constant value of ϵ, for obervation ϵ_{MODIS} is used and for the TSEB model we used ϵ_{avg} and ϵ_{rad} as shown in Fig. B.5c,d. The value of ϵ_{opt} using observed data shown in green is closer to the no-mismatch simulation of TSEB model from November to April and for May, June and September, the estimate of ϵ_{opt} is closer to the max-mismatch. The ϵ_{opt} for max-mismatch is as low as 0.7 for January and August. The c obtained using observations and ϵ_{opt} is positive shown by the green line in Fig. 3.3b and is closer to the maximum mismatch case shown by the red line for most of the months. For July and August the value of c is similar for both no-mismatch and max-mismatch, but the value of intercept is much

lower for max-mismatch case as shown in Fig. 3.3a. For maximum mismatch condition there was an energy imbalance which was added to the R_{lup} and the ϵ_{opt} was estimated which resulted in no intercept shown by the black line. The constant value of ϵ_{MODIS} with the observed data and for TSEB model we used ϵ_{avg} and ϵ_{rad} to simulate the max mismatch and no-mismatch the observed c shown by the green lies between the blue and the black lines showing no-mismatch and maximum mismatch conditions respectively.

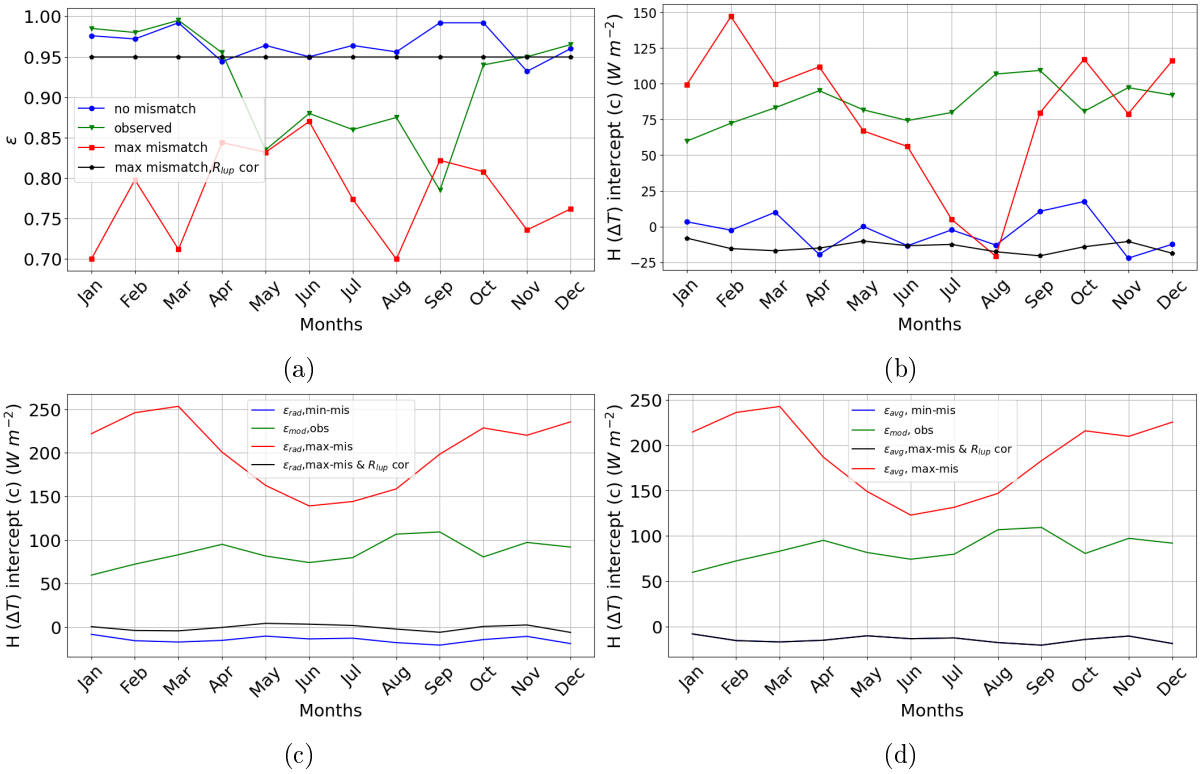

Figure B.5: Comparing seasonality in ϵ_{opt} and the intercept using observation and TSEB model for 2017 at AS (a)monthly plot of ϵ_{opt} using observation is in green and by simulating no mismatch and maximum mismatch using blue and black lines respectively; (b) the value of monthly intercept using ϵ_{opt} as shown in Eq. (2.8); (c) reproduction of (b) using ϵ_{rad} for all months instead of ϵ_{opt} (d) reproduction of (b) using ϵ_{avg} for all months instead of ϵ_{opt}.$\epsilon_{rad} = F_{v,rad} * \epsilon_v + (1 - F_{v,rad}) * \epsilon_s$ and $\epsilon_{avg} = F_{v,ec} * \epsilon_v + (1 - F_{v,ec}) * \epsilon_s$

B.3 TSEB model comparison with observations

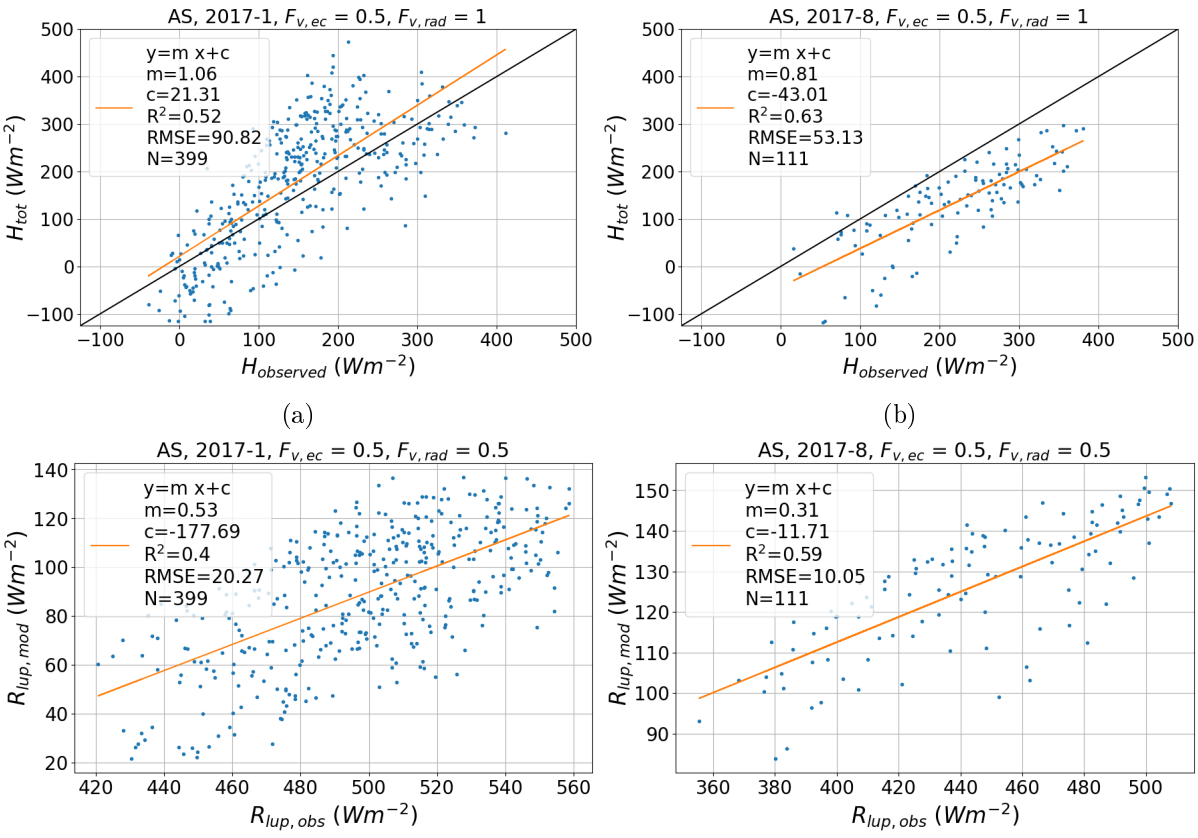

Figure B.6: Two source model result for AS(2017/07)

B.4 Energy imbalance

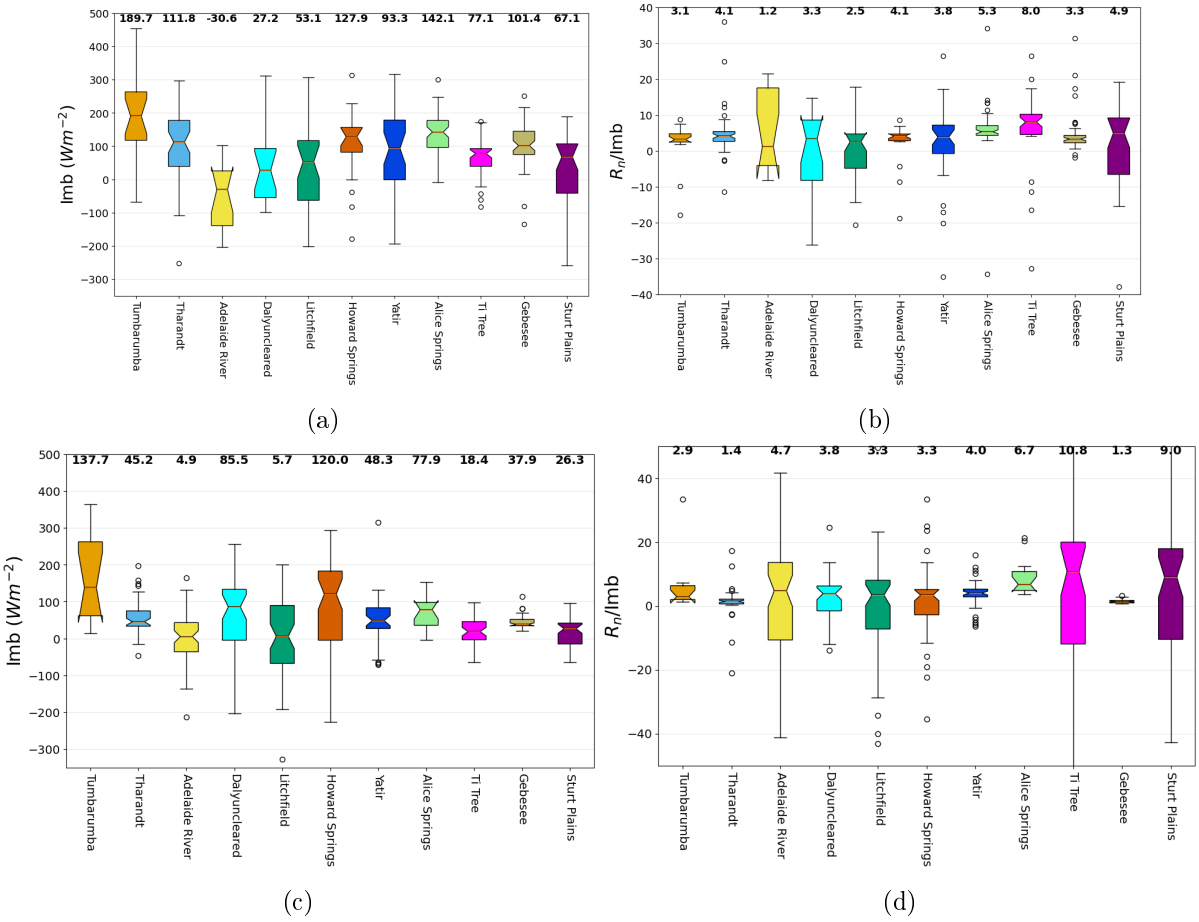

Figure B.7: a, b (Aus feb and other July) is for summer, c,d is for winters (in AUS august, for others 12)

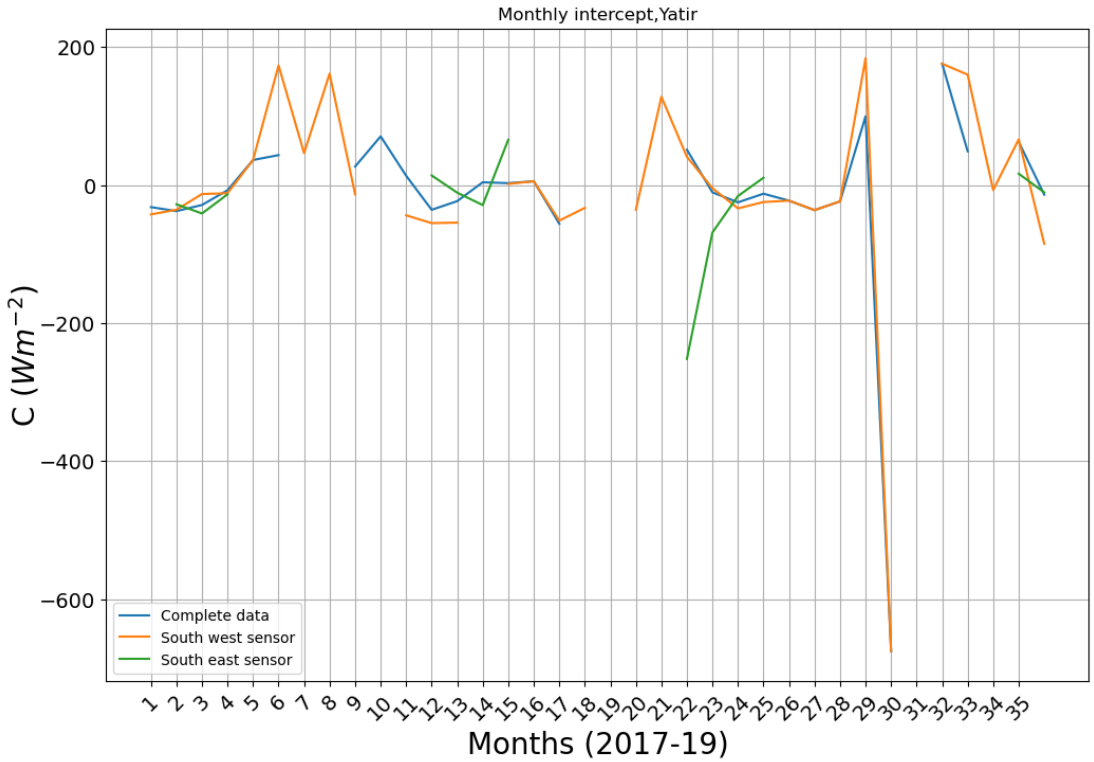

Figure B.8: C is the intercept obtained using monthly H vs ΔT plot using day time observation at Yatir for south west, south east radiometer position

Appendix C

Supplementary information for chapter 4

C.1 Equations

$$U_z = \begin{cases} \frac{U_* e^{-\frac{h\left(-\frac{Z}{Z_h}+1\right)}{(-d+Z_h)\log\left(\frac{-d+Z_h}{Z_{om}}\right)}} \log\left(\frac{-d+Z_h}{Z_{om}}\right)}{k} & \text{for } Z \leq h \wedge Z > 0 \\ \frac{U_* \log\left(\frac{Z-d}{Z_{om}}\right)}{k} & \text{for } Z > Z_h \end{cases} \tag{C.1}$$

$$U_z = \frac{U_* \log\left(\frac{Z-d}{Z_{om}}\right)}{k} \tag{C.2}$$

$$U_z = \frac{U_* \left(\psi_m + \log\left(\frac{Z-d}{Z_o}\right)\right)}{k} \tag{C.3}$$

In Eq. C.3 is estimated using ψ_m is corrected using Eq. C.4

$$\psi_m = \begin{cases} \frac{4.7Z}{L} & \text{for } \xi > 0 \\ -2\log\left(\frac{x}{2}+\frac{1}{2}\right) - \log\left(\frac{x^2}{2}+\frac{1}{2}\right) - 2\,\mathrm{atan}\,(x) - 1.5707963267949 & \text{for } \xi < 0 \end{cases} \tag{C.4}$$

$$\frac{K}{U} = (\frac{K}{U})_{Z_h} \tag{C.5}$$

We obtain the ratio of K/U at canopy top using Eq. C.1 and Eq. C.2 and by substituting $Z = h$. All the steps and equation are mentioned in the appendix. In Eq. C.1 U_z is the wind speed at any given height Z above the ground Cowan 1968, U_* is the shear wind velocity observed at the measurement height(Z_m), Z_h is the canopy height, d is the

displacement height, Z_{om} is the roughness length of momentum exchange.

$$u_{*bc} = \sqrt{\int_0^1 \alpha U_*^2 e^{-\frac{2h(1-\zeta)}{(-d+h)\log\left(\frac{-d+h}{Z_o}\right)}} d\zeta} \tag{C.6}$$

u_{*bc} is below value of U*, ζ is ratio of Z_h/Z, U_* measured value at or above the canopy top, α is the average leaf area index.

C.1.1 T_a and r_{az} profile at the study sites

Above canopy the heat flux is constant and is directly proportional to the temperature gradient as in Eq. C.7 we consider similarity in the between eddy diffusivity of heat and momentum.

$$H = -C_p \frac{\partial T}{\partial Z} k_m \rho_a \tag{C.7}$$

$$k_m = kU_* (Z - d) \tag{C.8}$$

$$\frac{\partial T}{\partial Z} = -\frac{H}{C_p k \rho_a U_* (Z - d)} \tag{C.9}$$

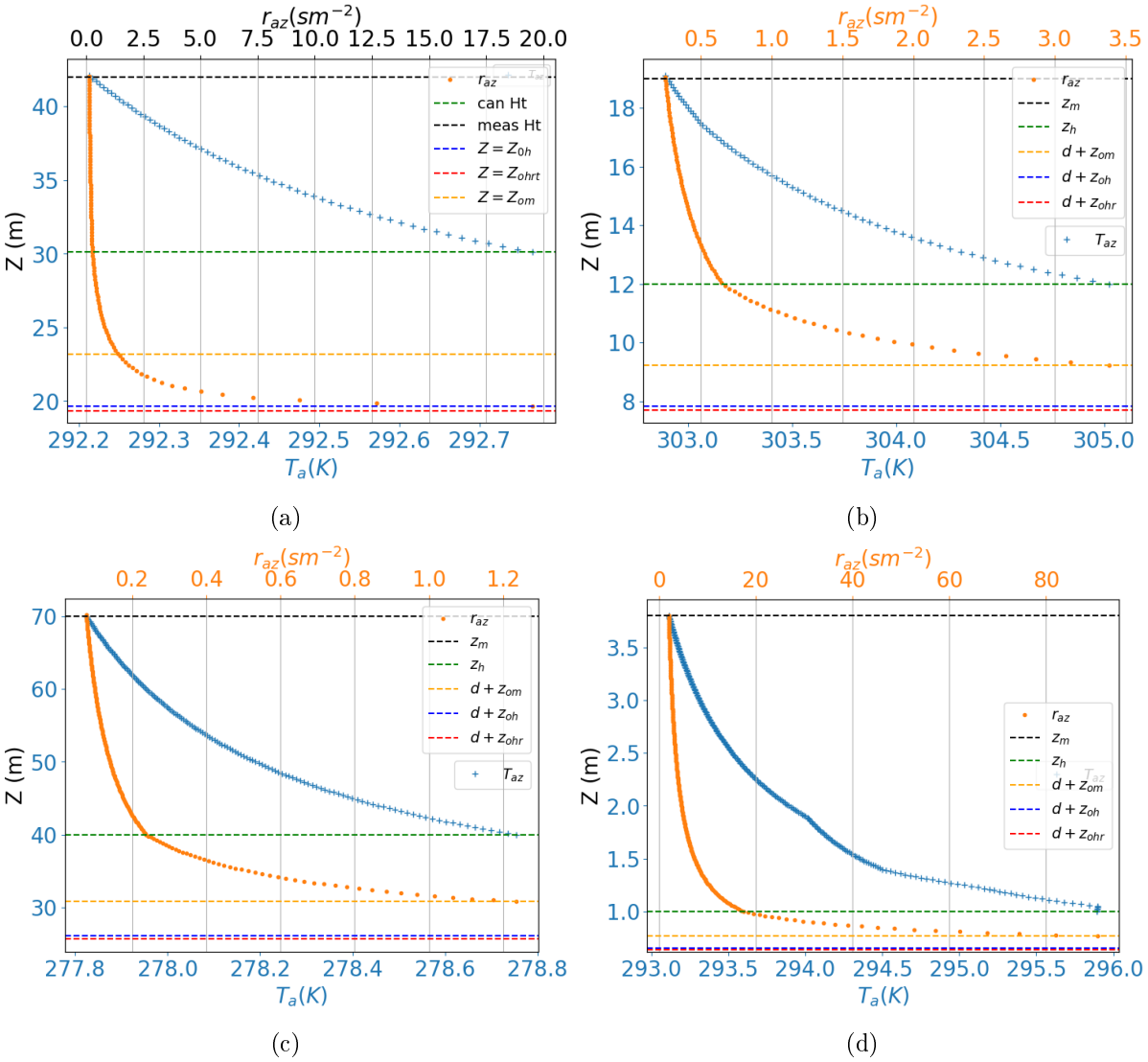

Figure C.1: r_{az} and T_a profile obtained using Eq. (C.9) with measurement mid-day measurements at the studysite: (a) TH on 2016/06, (b) YF 2017/06 (c) TUM on 2016/06 (d) GB on 2017/06

C.1.2 Resistance Profile

In this section we will formulate the three equations expressed by Grimmond and Voogt (Voogt and Grimmond 2000):

$$r_{am} = \frac{\log\left(\frac{Z_m - d}{Z_{om}}\right)}{kU_*} \tag{C.10}$$

$$r_r = \frac{\log\left(\frac{Z_{om}}{Z_{ohr}}\right)}{kU_*} \tag{C.11}$$

$$r_b = \frac{\log\left(\frac{Z_{om}}{Z_{oh}}\right)}{kU_*} \tag{C.12}$$

C.2 Exponential curve fitting

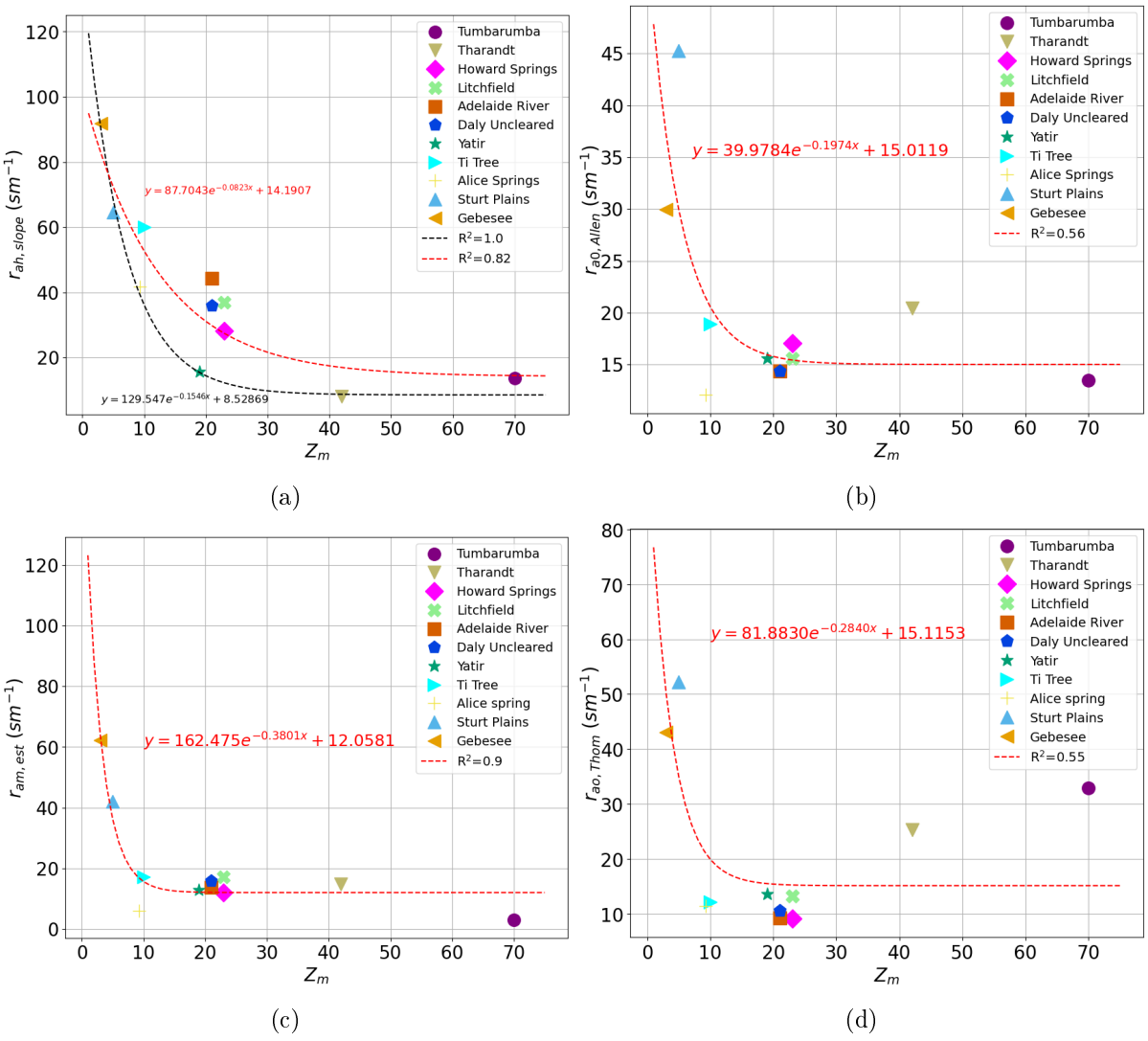

Figure C.2: Exponential curve fitting using scipy optimize curve fit function to the median of estimated resistance to heat exchange (a) Resistance inferred from observation $r_{ah,slope}$, (b) Resistance estimated using $r_{a0,Allen}$ with measured wind speed and measurement, (c) By inverting the momentum flux at the study sites $r_{am,est}$ and, (d) using stability based formulation from $r_{a0,Thom}$

C.3 Momentum resistivity (r_{az}) profile at study sites

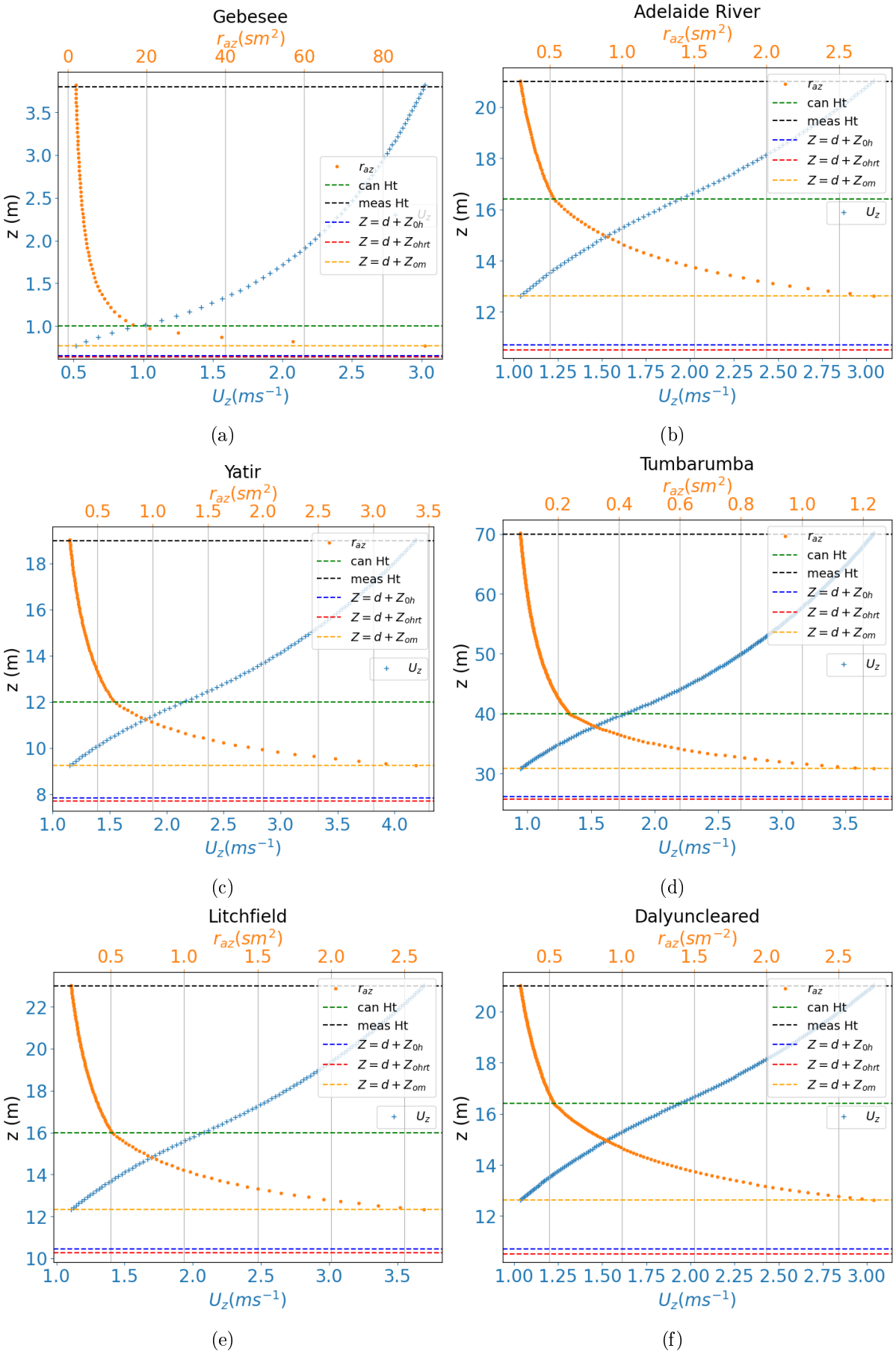

Figure C.3: Resistivity profile within and above canopy (a) GB (b)AR (c) LF and (d) DU

C.4 Estimated resistance and measurement height

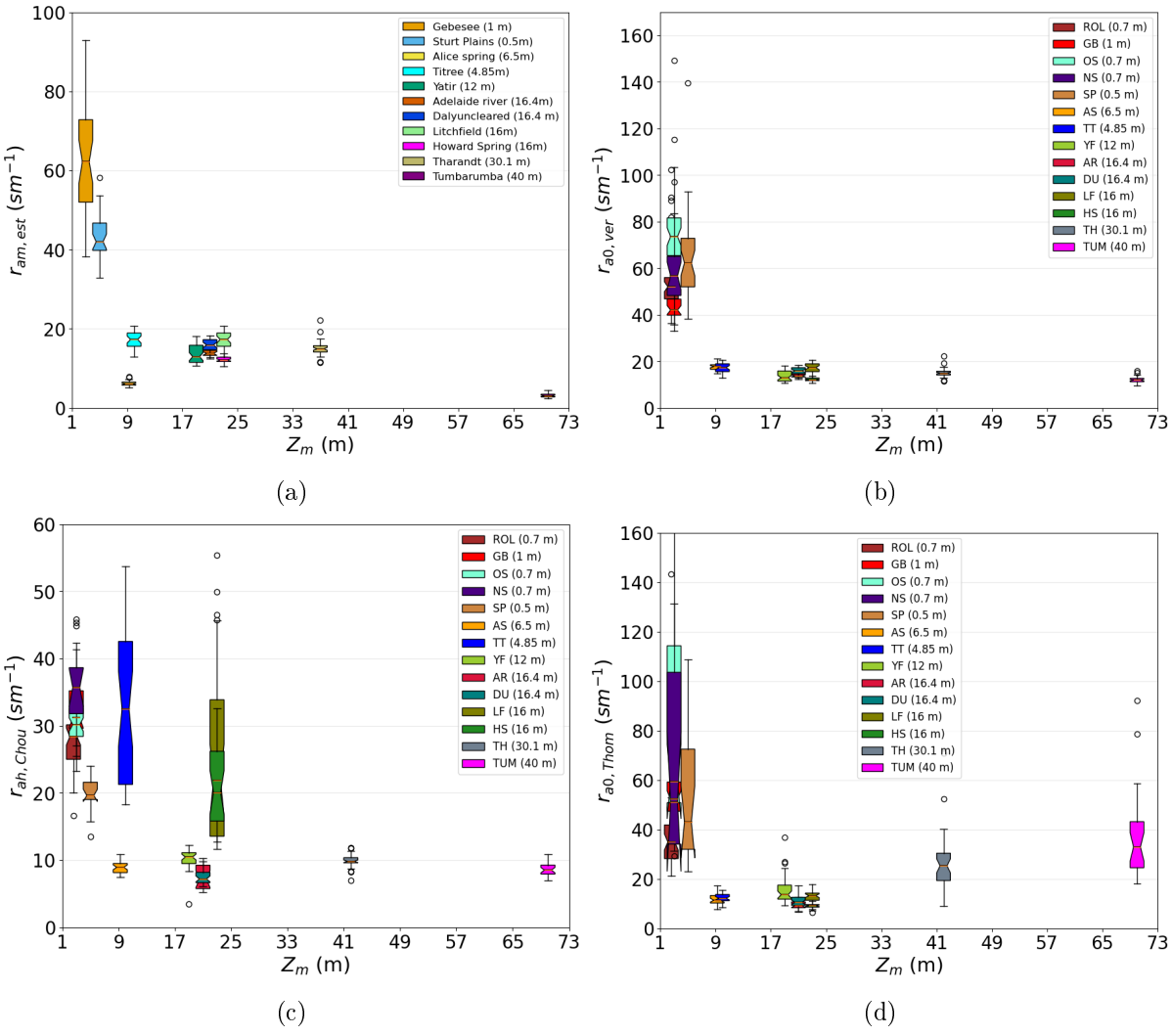

Figure C.4: Resistance estimated using three years of EC measurement and the measurement height

C.5 Comparison of 1:1 plot by adding leaf resistance to the existing formulations

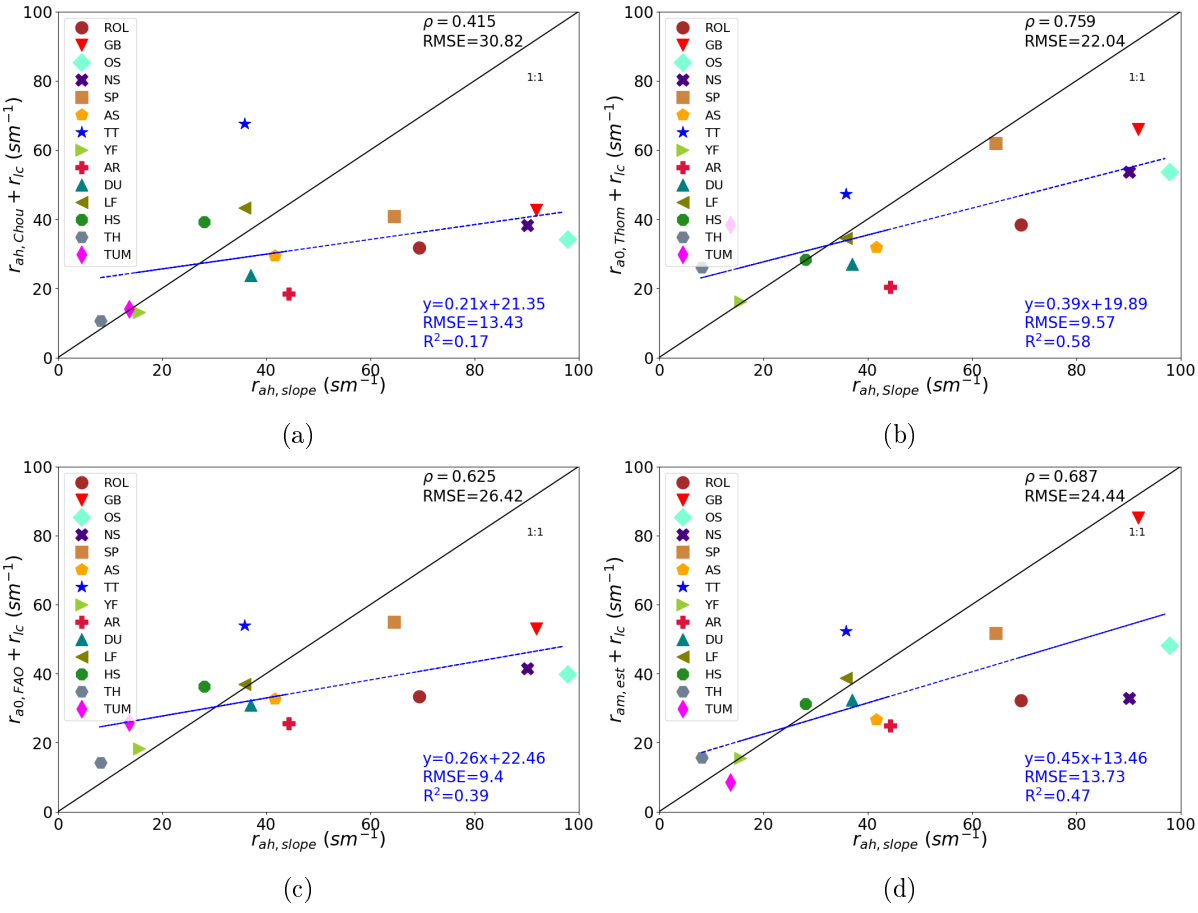

Figure C.5: Comparison $r_{ah,slope}$ by adding leaf boundary layer r_{lc} resistance to the existing formulations:(a) Choudhury et al. , (b) Thom et al., (c) Allen et al. (d) Estimated r_{am}

C.6 Comparing r_{ca} estimates at different height with the existing formulations $r_{ah,slope}$

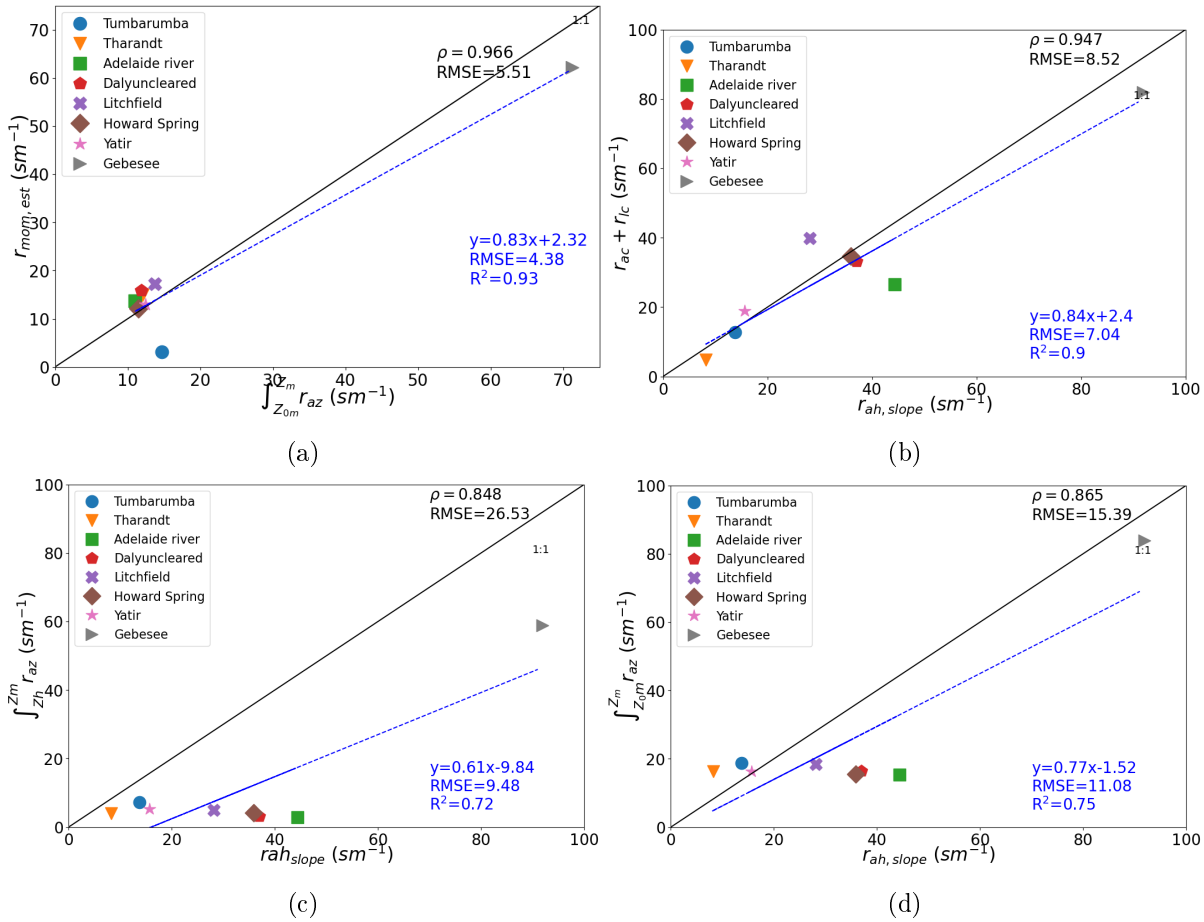

Figure C.6: (a)Comparison between r_{ca} estimated integrating r_{az} between Z_{om} to Z_m and $r_{am,est}$ (b) Estimating r_{ca} for closed canopies(TUM, TH, GB) by integrating r_{az} between Z_h to Z_m and for sparse canopies(HS, LF, AR, DU, YF) by integrating r_{az} between Z_{om} to Z_m. (c) Comparison between r_{ca} estimated by integrating r_{az} between Z_h to Z_m and $r_{ah,slope}$. (d) Comparison between r_{ca} estimated by integrating r_{az} between Z_{om} to Z_m and $r_{ah,slope}$

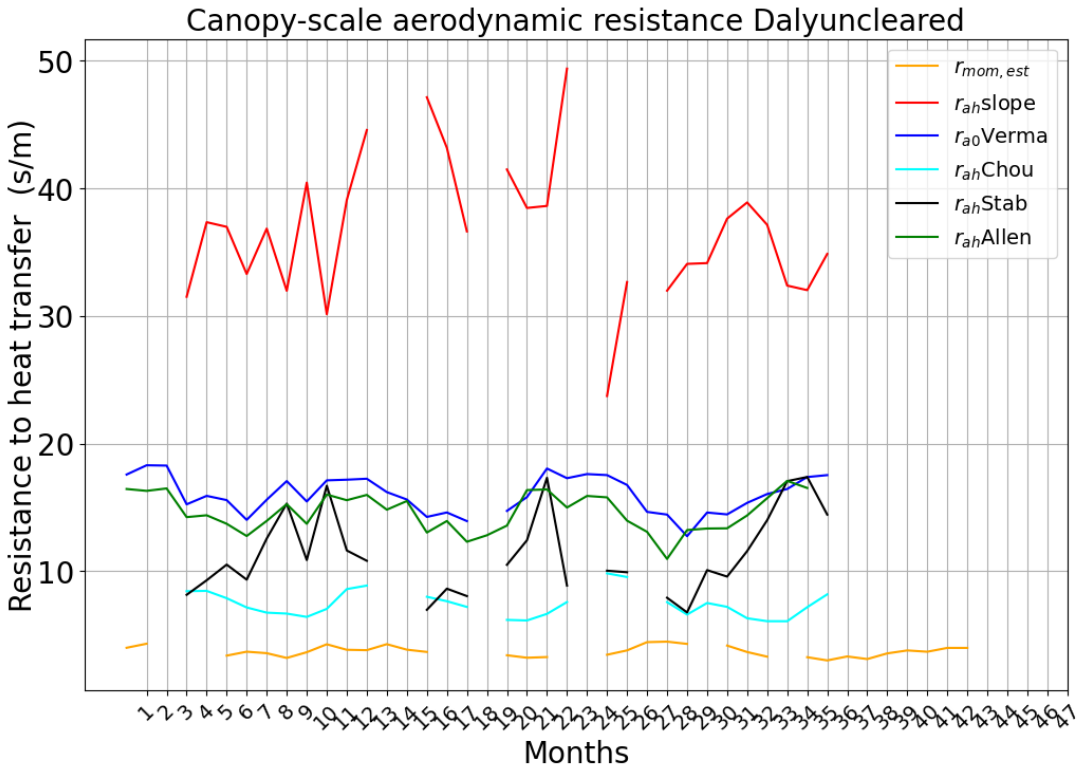

Figure C.8: Three years of daytime measurement have been used for the plot

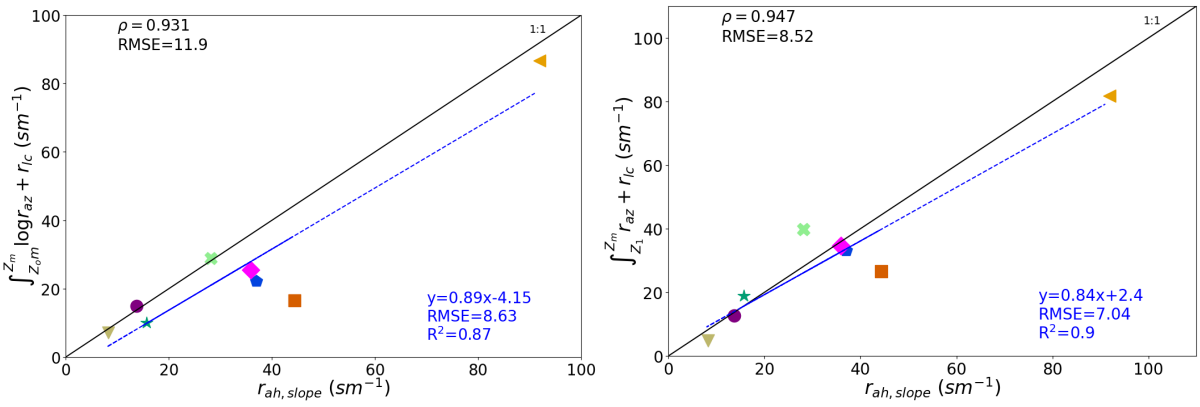

(a) (b)

Figure C.7: Comparison plot between inferred resistance $r_{ah,slope}$ in x-axis and estimated r_{lca} in y-axis, r_{lc} is estimated using Eq. 4.26 and r_{ca} is estimated (a) by integrating logarithmic r_{az} curve between Z_{om} and Z_m, (b) r_{ca} is estimated by integrating r_{az} between Z_h and Z_m for TH, TUM, GB and for others r_{az} is integrated between Z_{om} and Z_m

C.7 Monthly seasonality of different resistance formulation

C.8 r_b and r_{lc} seasonality

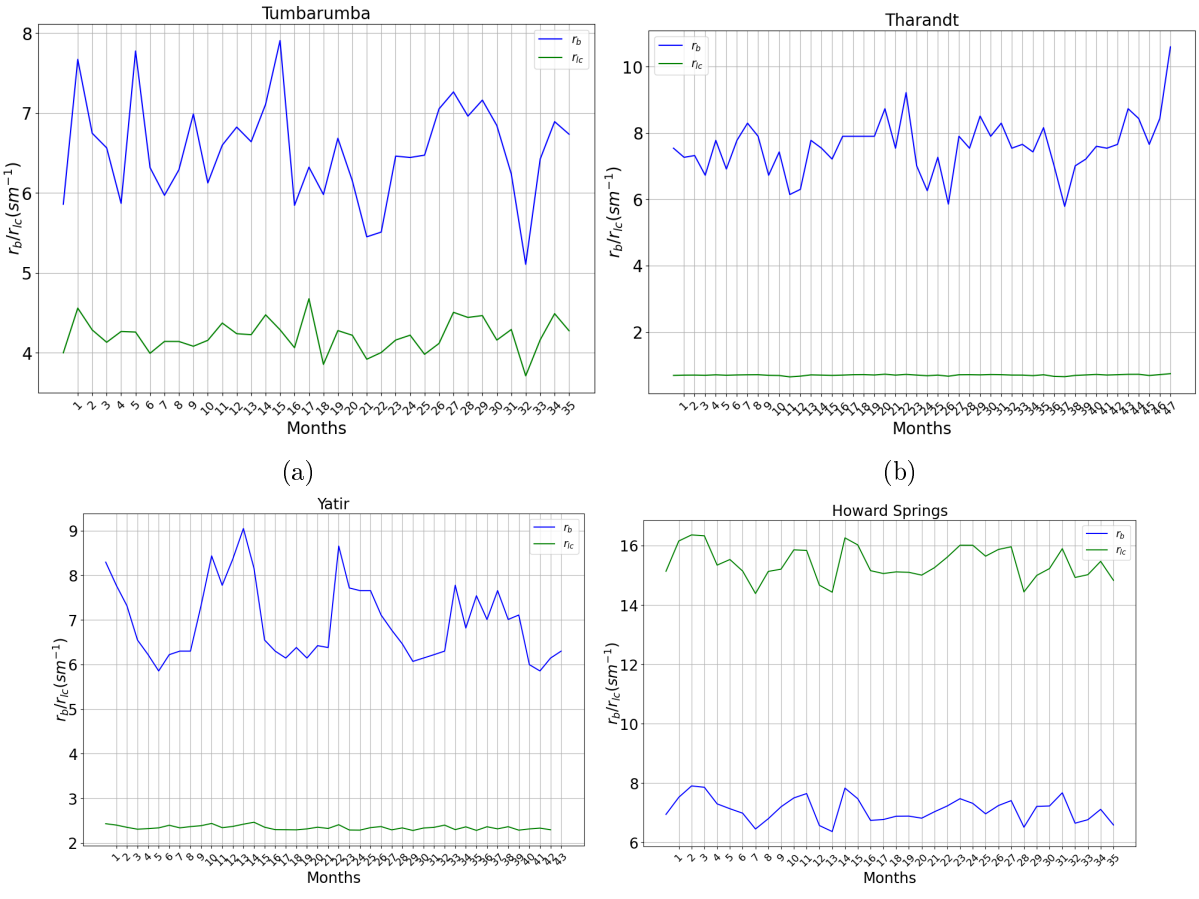

Figure C.9: Seasonality in monthly median of estimated r_b Eq. 4.14 and r_{lc} at (a)TUM (b) TH (c) YF (d) HS

C.9 Leaf resistance and LAI

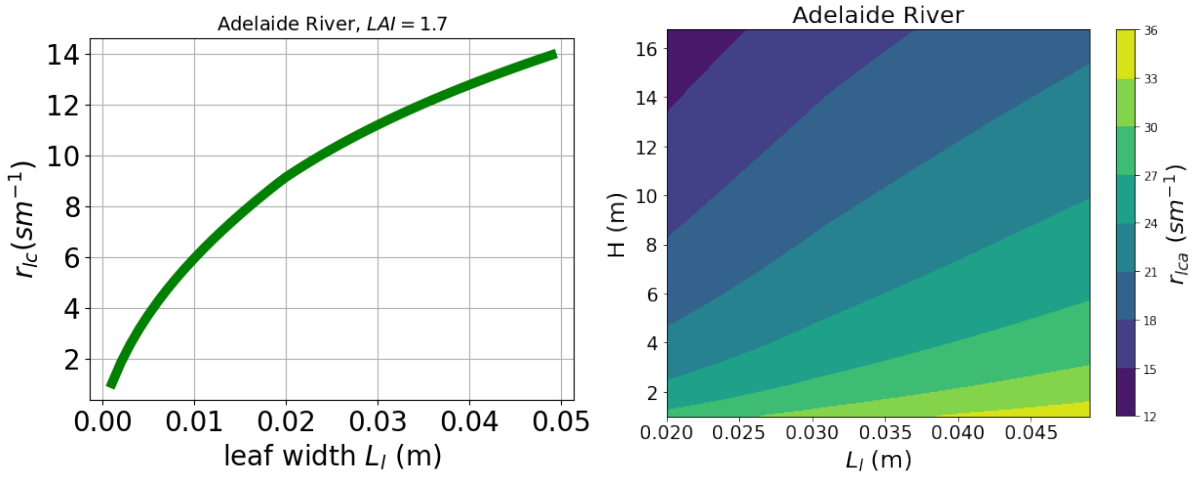

(a) (b)

Figure C.10: (a)The variation in r_{lc} with LAI, (b) Variation in the proposed canopy r_{lca} median with leaf size and canopy height

C.10 Leaf resistance using W_s, T_a at Z_m and Z_h

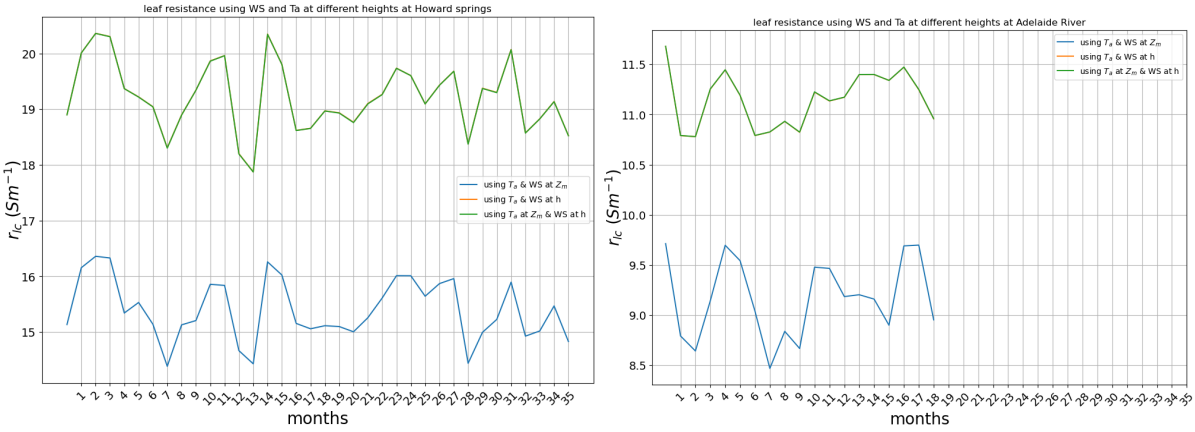

(a) (b)

Figure C.11: Monthly median of estimated r_{lc} at the study sites using measured wind speed and air temperature at Z_m and estimated wind speed and air temperature canopy-top Z_h at (a) HS (b) AR. AR has many months of missing data